

Copyright © 1994, by the author(s).
All rights reserved.

Permission to make digital or hard copies of all or part of this work for personal or classroom use is granted without fee provided that copies are not made or distributed for profit or commercial advantage and that copies bear this notice and the full citation on the first page. To copy otherwise, to republish, to post on servers or to redistribute to lists, requires prior specific permission.

**RIGOROUS THREE-DIMENSIONAL TIME-DOMAIN
FINITE-DIFFERENCE ELECTROMAGNETIC
SIMULATION**

by

Alfred Kwok-Kit Wong

Memorandum No. UCB/ERL M94/69

9 September 1994

**RIGOROUS THREE-DIMENSIONAL TIME-DOMAIN
FINITE-DIFFERENCE ELECTROMAGNETIC
SIMULATION**

Copyright © 1994

by

Alfred Kwok-Kit Wong

Memorandum No. UCB/ERL M94/69

9 September 1994

ELECTRONICS RESEARCH LABORATORY

College of Engineering
University of California, Berkeley
94720

**RIGOROUS THREE-DIMENSIONAL TIME-DOMAIN
FINITE-DIFFERENCE ELECTROMAGNETIC
SIMULATION**

Copyright © 1994

by

Alfred Kwok-Kit Wong

Memorandum No. UCB/ERL M94/69

9 September 1994

ELECTRONICS RESEARCH LABORATORY

College of Engineering
University of California, Berkeley
94720

Abstract

Rigorous Three-dimensional Time-Domain Finite-Difference Electromagnetic Simulation

by

Alfred Kwok-Kit Wong

Doctor of Philosophy in Electrical Engineering and Computer Sciences

University of California at Berkeley

Professor Andrew R. Neureuther, Chair

This thesis describes the latest embodiment of a three-dimensional electromagnetic simulation program called TEMPEST which is implemented on the connection machines CM-2 and CM-5, and is used to predict and study technology trade-offs of interest in photolithography. Highlights of the new algorithm include generalization to three-dimensional calculation, analysis of dispersive materials, an efficient absorbing boundary condition, oblique incidence, and image synthesis based on Hopkins' formulation.

The finite propagation speed of electromagnetic waves makes the time-domain finite-difference approach a natural choice for implementation on parallel computer architectures. This thesis addresses algorithmic issues including the accuracy and stability of the numerical scheme, and numerical boundary conditions. The conventional time-domain finite-difference scheme is second order accurate and requires 15 simulation nodes per wavelength to achieve a 2% accuracy. Stability of the scheme depends on the ratio between the spatial and temporal discretizations. Analogous to previous work in plasma physics, instability of the algorithm due to highly dispersive materials has been alleviated by calculating explicitly the time-domain convolution relation between the electric field and the electric displacement. A novel boundary condition derived from the harmonic nature of electromagnetic waves is used to bound the simulation domain with minimal artificial reflection.

Implementation of a software package which caters to user convenience in data processing and remote use of the connection machine is also included. A link between TEMPEST and the optical image simulation program SPLAT allows the study of the interaction among mask topography effects, partial coherence effects, and lens aberrations.

Validation of TEMPEST via experimental comparison and the usefulness of the program in predicting and assessing complex technological issues in photolithography are presented. In particular, TEMPEST is used to predict important effects such as glass edge scattering in phase-shifting masks and resonance in dielectric ridges. These predictions have been subsequently confirmed experimentally. Transmission loss and polarization effects in small contact holes are characterized as a function of the feature size. TEMPEST is also shown to be well-suited for analyzing three-dimensional effects of reflection from underlying topography during photoresist exposure which can cause variations in the critical dimensions of the features being formed.



Professor A. R. Neureuther
Committee Chairman

Table of Contents

Chapter 1	Introduction	1
Chapter 2	Numerical Methods in Electromagnetic Simulation	6
2.1	Introduction	6
2.2	Frequency-Domain Methods	6
2.3	Time-Domain Approaches	9
2.4	Summary	10
Chapter 3	The TDFD Algorithm	11
3.1	Introduction	11
3.2	Formulation	12
3.3	Distortion of the Structure	15
3.4	Accuracy	17
3.5	Stability	21
3.6	Conclusions	25
Chapter 4	Numerical Boundary Conditions	26
4.1	Introduction	26
4.2	Continuous Boundary Conditions	27
4.3	Discretization of the Boundary Operators	30
4.4	A Novel Boundary Condition	32
4.5	Boundary Conditions Comparison	36
4.6	Conclusions	42
Chapter 5	Modeling Dispersive Materials	43
5.1	Introduction	43
5.2	The Complex Field Method	44
5.3	The Four-step Method	46
5.4	The Frequency-dependent Finite-difference Time-domain Method	50
5.5	Comparison of the Four-step Method and the (FD)2TD Approach	52
5.6	Implementation of the (FD)2TD Approach	54
5.7	Performance Evaluation	56
5.8	Conclusions	58
Chapter 6	TEMPEST Software Package	60
6.1	Introduction	60
6.2	Reduction of Computation Efficiency due to the Boundary Condition	61
6.3	Domain Excitation	62
6.4	Convergence	64
6.5	Program Operation	66
6.6	Image Synthesis	67
6.7	Conclusions	72
Chapter 7	Two-dimensional Applications: Phase-shifting Mask Studies	74
7.1	TEMPEST Applications	74
7.2	Simulation Technique	74

7.3	Different Phase-shifting Mask Techniques	76
7.4	Alternating PSMs	78
7.5	Rim PSM	82
7.6	Attenuated PSM	86
7.7	Chromeless PSMs	101
7.8	Conclusions	105
Chapter 8	Three-dimensional Applications: Mask Edge Effects and Reflective Notching	109
8.1	Introduction	109
8.2	Simulation Context	109
8.3	Polarization Effects and Transmission loss in 1X Contact Holes	110
8.4	Defect Printability in Chromeless Phase-Shifting Masks	115
8.5	Reflective Notching	118
8.6	Conclusions	120
Chapter 9	Conclusions	122
References		125

Acknowledgments

Many people have provided me with assistance in this project and I would like to acknowledge their help. I would like to thank my advisor, Professor Neureuther, for his encouragement and guidance throughout the project. I am grateful to Professor Mei, Professor Oldham and Professor Strain who have given me valuable insight into problems in electromagnetic simulation, photolithography and numerical analysis. I have also learned a lot from Roberto Guerrieri in algorithms on the connection machine.

The friendly and warm working atmosphere within the research group has fostered meaningful discussions and novel ideas which were indispensable to the project. I am especially grateful to Michael Yeung for numerous discussions on electromagnetic simulation techniques. His vast knowledge in the field and his approach to the problem were invaluable. I would also like to thank Richard Ferguson and Kenny Toh for discussions and help.

This research was supported by the Charles LeGeyt Fortescue Fellowship, an IBM Fellowship, and the SRC/SEMATECH contract #93-MC-500. I would like to extend my appreciation to the Thinking Machines Corporation as well as the National Center for Supercomputing Applications for permissions to use their connection machine facilities.

I feel extremely fortunate to have the opportunities to receive an education at Berkeley and to live in a fair and open country. Associated with these opportunities are the responsibilities which sometimes put me in anguish.

Last but not least, I would like to thank my grandmother and mother, as well as my friends around the Bay Area who have helped me, directly or indirectly, to develop and improve: Chu Chong-Sun, Sidney Ho and family, Professor Sun and Mrs. Sun, Raymond Tam, Sandra Wong, Yu Kin-Man, and especially Leonora Lau who had endured a few years of TEMPEST.

Chapter 1

Introduction

Computer aided design (CAD) tools have come to play an important role in integrated circuit design, device design, and process design. Circuit simulation programs such as SPICE⁶² were among the first to be developed and gain popular acceptance. Device simulation programs such as MINIMOS⁷⁹ and PISCES⁷⁴ are helpful in understanding device performance. Process simulation tools such as DEPICT⁸⁶, SAMPLE⁷⁰, SOLID²⁷, and SUPREM⁴⁰ are becoming more popular as the cost of performing experiments rises continually with time and the cost of computation decreases dramatically from year to year. However, with the introduction of new technologies and the scaling of optical lithography to smaller feature sizes, greater demands are placed on the scope of the physical models and the accuracy of their implementation in algorithms. At the same time, these numerical models must be efficient in order to provide a rapid solution. These needs together have placed stringent requirements on the completeness, accuracy and efficiency of process simulation tools.

Modeling of the optical lithography and electromagnetic scattering processes has proven to be one of the greatest challenges. For example, standing wave patterns within the photoresist caused by substrate reflection must be accurately modeled. Image defocus effects within the photoresist layer may cause unwanted variation in the photoresist linewidth. Photoresist bleaching requires the modeling of an inhomogeneous layer of material whose optical properties dynamically change during exposure. Simulation of the dissolution of photoresists requires the tracking of moving surfaces which can collide with one another and produce loops. Removal of these loops poses a challenge for the computer programmer. Non-planar topographies in photomasks can cause lateral scattering of electromagnetic fields which often adversely affect the optical images. Further, topography on the silicon wafer can redirect waves in undesired directions and cause problems such as reflective notching. Alignment signals may also vary tremendously with a tiny change in the underlying layers or the alignment mark shape.

Electromagnetic problems are particularly computation intensive because typical feature sizes of interest are on the order of a wavelength. In this regime, neither geometric optics nor

Rayleigh's method suffices. Even with the most advanced numerical techniques, some of these problems are not tractable. For example, solving the problem with rigorous frequency-domain methods requires the solution to a system of millions of simultaneous equations. Direct solution of the matrix is not feasible with the current numerical techniques. Iterative solutions such as the conjugate gradient method³⁶ or GMRES⁷⁸ are not attractive as the matrix is not positive definite and the condition number is large. With time-domain methods, typically 15 simulation nodes per wavelength are required to achieve the desired accuracy. For modeling of deep-UV lithography at a wavelength of 0.248 μm , a typical volume of interest is 4 μm by 4 μm by 2 μm , corresponding to $2048\lambda^3$ or 8 million simulation nodes. The size of the problem makes it difficult to solve even on the most advanced workstations.

With the advent of supercomputers such as the Cray and the connection machine, some of these difficult problems can be tackled through the massive amount of computer power. The key is to shorten the computation time by parallel evaluation of the problem. In the modeling of photolithography, such a parallelization is possible for the simulation of electromagnetic (light) wave propagation using the time-domain finite-difference (TDFD) method. Unlike most frequency-domain approaches in which each simulation node is coupled to all the other nodes in the simulation domain, information is only exchanged with the nearest neighboring nodes in the TDFD method because of the finite propagation speed of light. The solution for a problem is achieved by time iteration until steady-state is reached. Hence, it is not necessary, in the TDFD approach, to invert a large matrix which is often the limiting factor for frequency-domain approaches. Furthermore, since Maxwell's equations are satisfied everywhere in space, the updating equations for all simulation nodes (except for the boundary nodes) are identical, and this makes programming simple. This approach is both accurate and efficient. It is accurate because no approximation concerning the propagation of the electromagnetic wave is made (as Maxwell's equations are solved); it is efficient because each processor on the parallel computer is solving identical equations in parallel.

This thesis presents the formulation and implementation aspects of electromagnetic simulation using the TDFD method. The computer program is called TEMPEST and it is implemented on the parallel computer architectures connection machine 2 (CM-2)²⁹ and

connection machine 5 (CM-5)⁸⁸. The simulation program solves Maxwell's equations using the TDFD method. The algorithm is built on that proposed by Yee¹⁰⁴ and the initial formulation and implementation by Guerrieri²⁵ and Gamelin²³. Electromagnetic wave propagation and scattering are simulated by solving iteratively the discretized Maxwell's equations until the electromagnetic field inside the simulation domain reaches steady-state. In this thesis, generalization to three-dimensional analysis is discussed. Discretized equations are shown for this first three-dimensional formulation on the connection machine, together with the accuracy and stability of the numerical scheme. Accuracy of the leap-frog numerical scheme is shown to be second order accurate except for materials with the property that $\epsilon_i \gg \epsilon_r$. Stability of the algorithm depends both on the ratio of the spatial discretization Δx to the temporal discretization Δt being greater than the speed of light multiplied by a constant as well as the real part of the refractive index being larger than the imaginary part. Simulation of highly dispersive materials in which $n_i > n_r$ is feasible when the convolution between the electric field E and the electric displacement D is explicitly calculated. Two susceptibility models relating E and D are used: the Debye model which models ionic-like materials and the Lorentz model which models metallic-like materials. Another difficulty with accurate and efficient three-dimensional electromagnetic simulation is the need for a robust numerical absorbing boundary condition. A novel numerical boundary condition derived from the harmonic nature of electromagnetic waves is used to bound the simulation domain with minimal artificial reflection.

Another theme of the thesis is the assembly of a software package. In addition to the electromagnetic solver TEMPEST, the software package contains auxiliary routines including utilities to display the calculated electromagnetic fields and a program which checks for the correctness of the input files. The optical image profile of the simulated structure can also be calculated via a link to the simulation program SPLAT⁸⁹. This linkage allows the results of rigorous electromagnetic simulation from TEMPEST (the electromagnetic fields transmitted through or reflected from two-dimensional and three-dimensional objects) to be interpreted in the context of optical system effects (such as lens aberrations).

Application studies of problems of interest in photolithography are the driving forces behind the algorithm. The first version of TEMPEST formulated by Guerrieri²⁵ and implemented

by Gamelin²³ has been useful in the initial studies of many areas of photolithography such as reflective notching⁸¹, optical metrology⁸², signal integrity in mask transmission¹⁴, and alignment mark signal quality⁹⁹. To better facilitate these application studies, the original two-dimensional TEMPEST was generalized by the author in his M. S. thesis¹⁰². This extended two-dimensional TEMPEST which includes the capabilities to analyze the transverse magnetic polarization and oblique incidence has been applied in the studies of phase-shifting mask (PSM) techniques such as alternating and rim⁷³, attenuated²⁰, and chromeless¹⁰¹, as well as issues in extreme ultraviolet lithography (EUV) such as defects in multi-layer masks⁶⁶. One application study of particular interest is considered in detail in this thesis: examining the trade-offs in four different PSM techniques including alternating, rim, attenuated, and chromeless. With the added three-dimensional and image synthesis capabilities, TEMPEST is expected to make an even greater impact on the integrated circuit fabrication industry because it can examine truly three-dimensional technological issues in photolithography accurately and efficiently. Initial results of three-dimensional studies of transmission in contact holes and reflective notching are also presented.

A historical account of the different techniques proposed to solve electromagnetic problems in photolithography is first discussed in Chapter 2. These different techniques fall primarily into two categories: time-domain methods and frequency-domain methods. The TDFD approach used by TEMPEST is then discussed in Chapter 3. Stability of the numerical scheme depends on the ratio of the temporal discretization (Δt) to the spatial discretization (Δx) not being greater than some number related to the speed of light. In order to confine the computation volume, numerical absorbing boundary conditions are necessary. These boundary conditions must be efficient yet robust enough to minimize the amount of artificial reflection. In Chapter 4, several absorbing boundary conditions are presented including a novel boundary operator derived based on the harmonic nature of the electromagnetic radiation. Extension of the conventional TDFD method to analyze highly dispersive materials is shown in Chapter 5. This extension is necessary for lithographic applications because many of the commonly used materials in the fabrication of integrated circuits have the property that the imaginary part of the refractive index is greater than the real part. This results in a negative permittivity and the conventional TDFD algorithm becomes unstable.

Chapter 6 discusses some aspects of the software package TEMPEST and its implementation on the connection machine. Convergence of the program is observed to be dominated by physical scattering phenomena rather than the numerics. The need for careful excitation of the simulation domain and correction factors for the computation of diffraction harmonics due to the staggering of the FDTD grid are also discussed. Since TEMPEST only calculates the electromagnetic response of a structure whereas the optical image is the quantity which is the most often desired, conversion from the steady-state fields calculated by TEMPEST into an intensity profile is necessary. This task is accomplished by an interface to another simulation program called SPLAT⁸⁹.

Applications of the program and validation of TEMPEST by experimental verification are presented in Chapter 7 and Chapter 8. These applications show the applicability of the program in assessing the state-of-the-art technologies. In Chapter 7, TEMPEST is applied in the study of two-dimensional PSMs. Four different techniques including alternating, rim, attenuated, and chromeless are examined. Simulation results show that glass edge scattering is important in degrading the images of all these types of PSMs. This finding is confirmed by experimental studies. In Chapter 8, three-dimensional effects such as contact hole printing, phase defect printability, and reflective notching are examined. It is shown that transmission loss and polarization effects are important for small openings on chromium binary masks. Furthermore, 360° phase bump defects do not affect the optical image as adversely as 360° phase trench and protrusion effects. An initial study of latent image formation in photoresist over underlying topography shows that the critical dimension of the polysilicon gate varies over a stepped substrate.

Chapter 9 concludes the thesis and presents some possible extensions to the current simulation program. These include expanding the applicability of TEMPEST to a wider scope of problems such as the modeling of laser cavities. Furthermore, with the advent of multiple-program multiple data (MPMD) supercomputers, it is possible to improve the efficiency of the current simulation program, which is coded in the single-instruction multiple-data (SIMD) or the massively-parallel programming mode.

Chapter 2

Numerical Methods in Electromagnetic Simulation

2.1 Introduction

The electromagnetic problems of interest in photolithography present some difficulties for numerical modeling because typical feature sizes are on the order of a wavelength. In this regime, neither geometric optics (assuming that the radii of curvature of the surfaces are much larger than the wavelength) nor Rayleigh's method (assuming that the wavelength is much larger than the radii of curvature) suffices. The general problem of electromagnetic scattering from topography has been addressed in various ways. In this chapter, an overview of these different methods are described. These techniques can be classified as either frequency-domain or time-domain methods. (This is not the only classification. Yeung¹⁰⁷ classified the different techniques as modal expansion, Green's function based, volume based, and fast multipole methods.) For frequency-domain methods, the electromagnetic fields are usually expressed as a superposition of some basis functions. The steady-state electromagnetic solution is found by solving (directly or iteratively) a matrix. For time-domain methods, a time parameter is introduced and the steady-state electromagnetic fields are found by time-marching, i.e., electromagnetic interaction with matter is solved in time until the fields become time-harmonic. In general, frequency-domain methods have the advantage of simplicity as the solution is found once the system of equations is solved. However, the system of equations may be so large that the resulting matrix becomes impractical to solve. Time-domain methods do not have the problem of solving large matrices, but time-marching may be so computation intensive that a solution cannot be found within a reasonable amount of time.

2.2 Frequency-Domain Methods

2.2.1 Rayleigh's Method

Rayleigh made one of the first attempts to analyze the problem of electromagnetic scattering from a periodic grating rigorously. He made the assumption that the fields can be

expressed as a linear superposition of propagating and evanescent waves^{75,76}. Based on Rayleigh's hypothesis, Meecham⁵² used a variational method to calculate the diffraction efficiencies when a plane wave is incident upon a periodic reflecting surface. Rayleigh's assumption was unquestioned until Deriugin¹³ and Lippmann⁴⁵ raised objections to it. In 1966, Petit and Cadilhac⁷² demonstrated that the Rayleigh hypothesis is tenable only if the product of the wave number and the grating depth is less than 0.448. Nevertheless, Gallatin et al.²² as well as Bobroff and Rosenbluth⁴ applied this method to model the images of alignment marks under photoresist. But their methods are limited to long, shallow features with homogeneous layers. Another drawback of Rayleigh's method is that the computation time increases with the grating depth and the refractive index of the grating material as demonstrated by Zaki¹¹¹.

2.2.2 The Waveguide Method

Burckhardt⁸ tackled the problem of diffraction at a sinusoidally stratified dielectric grating by solving Maxwell's equations. The method of separation of variables was employed, and the transverse electric solution was found by truncating the infinite series representation of the electric field within each layer of the stratification. The resulting matrix was solved on an IBM 7094 in 1966. Kasper³³ extended Burckhardt's method to include complex dielectric constants and non-sinusoidal stratifications. Following the approach of Burckhardt and Kasper, Nyssonen and Kirk⁶⁹ developed the waveguide method and applied it in the examination of photolithographic issues such as edge detection⁶⁸ and alignment mark signals³⁷. Yuan et al.¹⁰⁸ extended the waveguide method to the transverse magnetic polarization and applied it in the study of wafer alignment and linewidth measurement¹⁰⁹. Lucas et al.⁴⁶ also applied the same technique in the study of two-dimensional phase-shifting mask structures.

2.2.3 Differential and Integral Methods

Neviere et al.⁶⁵ used the differential method to study the resonances of holographic thin film couplers. In this technique, the electromagnetic field as well as the square of the wave number are expanded as Fourier series. The Helmholtz equation thus becomes a set of coupled ordinary differential equations. However, this method has problems in modeling highly conducting gratings

(because of the difficulty in Fourier expansion of a large or infinite permittivity) and the transverse magnetic polarization (because of the boundary condition at material interfaces). Neureuther and Zaki⁶³ proposed an integral method which alleviated the problems of the differential technique. Their formulation involved integral equations with kernels containing the periodic Green's function and its derivative. Botten⁶ extended the integral method by reducing the integral equations to the solution of a Fredholm integral equation of the first kind. Maystre⁵¹ further improved the method for an arbitrary number of layers. The method requires $(p - 1)$ successive matrix inversions for a p -layer structure.

2.2.4 Finite-Element Methods

Morgan et al.⁶⁰ solved electromagnetic boundary value problems using the finite-element method combined with the surface integral equation. In this technique, the internal region finite-element field solution is coupled to equivalent currents on the boundary surface through a surface integral solution. Using a similar procedure, Moaveni et al.⁵⁹ studied electromagnetic scattering of periodic cylinders of arbitrary cross-section embedded in an inhomogeneous and lossy dielectric. Matsuzawa et al.⁵⁰ solved the Helmholtz equation using the finite-element method together with the boundary-element method and applied it in the study of photoresist bleaching on a stepped perfectly conducting substrate. The approach was improved by Urbach and Bernard⁹³ with the extension to more general domains and partial coherence. Using the spectral element method in which the electromagnetic field is expanded with the Legendre polynomials as the basis functions, Barouch et al.¹ is able to study three-dimensional reflective notching on non-planar substrates. The method consists of solving the Helmholtz equation by performing static condensation on the matrix system.

2.2.5 Other Techniques

There are many other frequency-domain techniques besides those mentioned previously. Mei⁵³ proposed the unimoment method which enables the separation of the exterior boundary value problem from an interior one. Such a formulation has the advantage that inhomogeneous media can be easily modeled, but has the disadvantage of requiring a direct matrix solution because of stability

of the resulting system of equations. Bischoff et al.² formulated a method based on the principles of Keller's geometrical theory of diffraction and their uniform extension (the locality principle) in order to study latent images in photoresists. Yeung et al.¹⁰⁶ investigated an approximate method combining physical optics with the integral equation method. This technique is well-suited for general geometries and has compared well with rigorous solutions.

2.3 Time-Domain Approaches

The previous section discusses the solution of electromagnetic problems via frequency-domain methods. In such techniques, a large system of equations must be solved. Thus, the difficulty of frequency-domain approaches is the solving of a large matrix. Time-domain approaches, on the other hand, require no matrix inversion. The electromagnetic solution is found by time-marching. The difficulty in solving a large matrix is replaced by the need to perform billions and even trillions of additions and multiplications.

Yee¹⁰⁴ was one of the first to replace Maxwell's equations by a set of finite difference equations and solve the electromagnetic problem via a staggered grid. Merewether⁵⁸ applied the technique together with the use of the radiation condition (numerical absorbing boundary condition) to study transient currents induced on a metallic body of revolution by an electromagnetic pulse. Taflove and Brodwin⁸³ examined the steady-state electromagnetic field resulting from the scattering of a two-dimensional uniform and circular dielectric cylinder.

Improvements of the conventional TDFD method to allow for more flexible geometries and more efficient memory usage were also suggested. Mei et al.⁵⁴ demonstrated the feasibility of the conformal TDFD method which enables the finite-difference mesh to conform to the object surfaces. Zivanovic et al.¹¹² proposed a subgridding TDFD method which employs a variable step size. The entire computation volume is divided into a coarse grid with a large step size, and a fine grid is introduced only around material interfaces. This subgridding method decreases the memory usage and does not introduce additional numerical error.

There has also been efforts aiming to combine frequency-domain and time-domain techniques. Taflove and Umashankar⁸⁴ investigated a hybrid TDFD and method of moment approach and applied it in the study of electromagnetic coupling and aperture penetration into

complex geometries. Fornberg²¹ studied the pseudospectral method in which the spatial derivatives are computed in the frequency-domain whereas the steady-state solution is found by time-marching. This technique has been applied by Carcione et al.⁹ in the computation of synthetic seismograms.

Because of its computation intensive nature, time-domain solutions of electromagnetic problems in photolithography was impractical until the advent of powerful supercomputers in the late 1980s. Wojcik et al. studied the time-domain finite-element (TDFE) method⁹⁸ and applied it in the study of light scattering from silicon surfaces⁹⁵, alignment mark signals⁹⁶, and linewidth metrology⁹⁷. Concurrently, Guerrieri et al.²⁵ formulated and Gamelin²³ implemented the TDFD approach on the connection machine CM-2 and applied it in the study of reflective notching⁸¹, metrology of polysilicon gate structures⁸², mask material and coating effects on image quality¹⁴, and alignment mark signal integrity⁹⁹.

2.4 Summary

Electromagnetic simulation in photolithography is difficult because of the problem size and the requirements of accurate and efficient numerical models. The advances in numerical techniques as well as the tremendous increase in computation power in recent years allow the tackling of complex problems in integrated circuit processing. The inherent parallel nature of wave propagation together with the advent of parallel computers make the TDFD approach a natural choice for simulation of electromagnetic problems in photolithography. In the following chapters, previous works relevant to the TDFD approach are extended to allow the modeling of problems in photolithography. These include a three-dimensional formulation which results in six discretized equations, generalization of the conventional TDFD numerical scheme to model highly dispersive materials, and the implementation of a novel numerical boundary condition which is efficient and minimizes artificial reflection.

Chapter 3

The TDFD Algorithm

3.1 Introduction

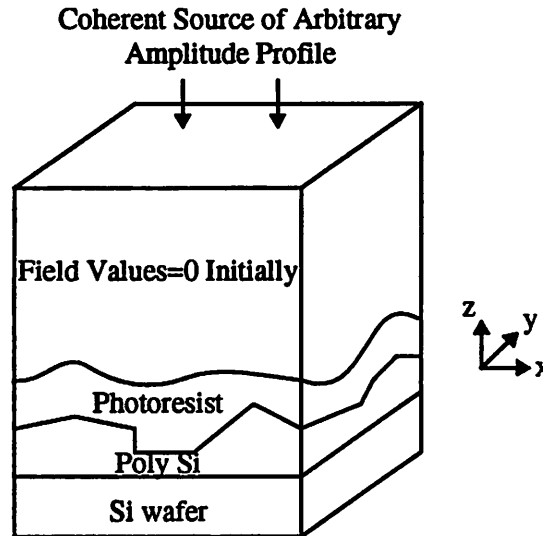


Figure 3.1 A typical simulation domain in TEMPEST. The structure can represent arbitrary three-dimensional non-planar and inhomogeneous topography. The domain is excited at the top by a monochromatic plane wave.

This chapter presents the time-domain finite-difference (TDFD) scheme used for three-dimensional electromagnetic field calculation on the connection machine. Two-dimensional formulations in the transverse electric (TE) and transverse magnetic (TM) polarizations can be found respectively in previous works by Gamelin²³ and Wong¹⁰². This three-dimensional formulation is an extension of the concepts by Yee¹⁰⁴ and Guerrieri²⁵. The complete set of updating equations is first derived. The accuracy of the numerical scheme is then estimated by consideration of the eigenvalues and eigenfunctions as well as the local truncation error. Stability of the numerical scheme is also studied using the Fourier method, resulting in a relationship between the spatial discretization Δx and the temporal discretization Δt .

3.2 Formulation

A typical simulation domain for electromagnetic fields calculation is shown in Figure 3.1. The structure can represent arbitrary three-dimensional non-planar and inhomogeneous topography. For lithographic applications, the interest is almost always the response of the structure at a particular frequency or at a narrow band of frequencies. The simulation domain is thus excited with monochromatic radiation at the top. (Note that monochromatic excitation is not an assumption in the TDFD scheme, and thus the techniques discussed in this thesis are applicable to the general problem in which the incident radiation consists of waves of different frequencies.) The problem is to find the steady-state solution for Maxwell's equations*:

$$\nabla \times \vec{H} = \frac{\partial \vec{D}}{\partial t} + \vec{j} \quad (3.1)$$

$$\nabla \times \vec{E} = -\frac{\partial \vec{B}}{\partial t} \quad (3.2)$$

supplemented with the constitutive relations:

$$\vec{B} = \mu \vec{H}$$

$$\vec{D} = \epsilon \vec{E}$$

$$\vec{j} = \sigma \vec{E}$$

where ϵ , μ , and σ are respectively the permittivity, permeability, and conductivity of the material. In general, the parameters μ , ϵ , and σ are functions of the frequency of the electromagnetic wave. For the application in hand, however, they are assumed to be constant because of monochromatic excitation. Using Stokes' theorem, equations (3.1) and (3.2) can be re-written in the weak form:

$$\oint_{\Gamma} \vec{H} \cdot d\vec{l} = \int_{\mathcal{S}} \left\{ \frac{\partial \vec{D}}{\partial t} + \vec{j} \right\} \cdot d\vec{S} \quad (3.3)$$

$$\oint_{\Gamma} \vec{E} \cdot d\vec{l} = -\int_{\mathcal{S}} \frac{\partial \vec{B}}{\partial t} \cdot d\vec{S} \quad (3.4)$$

*. In the MKS system.

where $\oint \vec{F} \cdot d\vec{l}$ and $\int \vec{F} \cdot d\vec{S}$ represent respectively the line integral and surface integral of a variable \vec{F} .

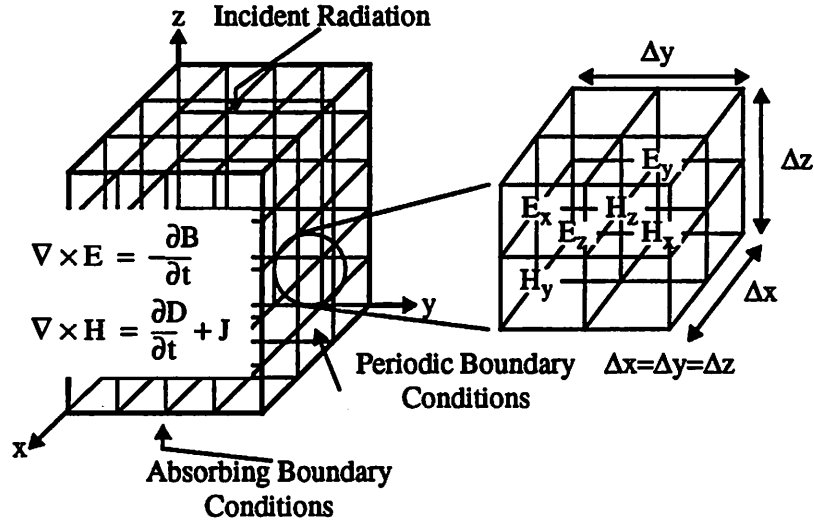


Figure 3.2 The TEMPEST simulation domain. Maxwell's equations are solved over a cubic grid using the TDFD method. The field components are staggered over the grid.

Following the TDFD method proposed by Yee¹⁰⁴, equations (3.3) and (3.4) are solved using a cubic grid in which the field components are staggered and occupy distinct locations in space as shown in Figure 3.2. The surface integral and line integral are thus evaluated on square surfaces. With this discretization scheme, equations (3.3) and (3.4) become six scalar equations for the field components E_x , E_y , E_z , H_x , H_y , and H_z . For example, Figure 3.3 shows that the electric field in the z -direction is calculated by summing up (with the sign properly taken into consideration) the magnetic field values of the four neighboring points. This scheme assumes that the electric field is constant over the square surface and the magnetic field is constant along each line segment which makes up the square. This results in the following spatially discretized equation:

$$\begin{aligned}
 (\epsilon \frac{\partial}{\partial t} + \sigma) E_z(i, j, k) \Delta x^2 = \\
 \left[H_x(i, j - \frac{1}{2}, k) - H_x(i, j + \frac{1}{2}, k) + H_y(i + \frac{1}{2}, j, k) - H_y(i - \frac{1}{2}, j, k) \right] \Delta x
 \end{aligned} \tag{3.5}$$

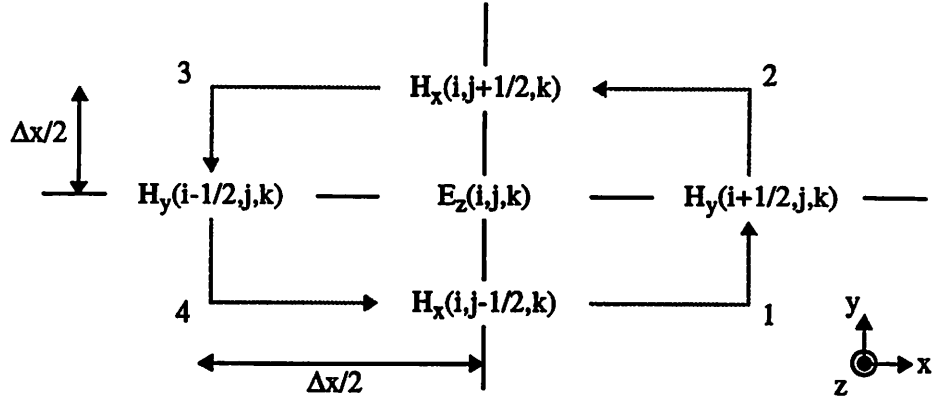


Figure 3.3 The electric field component $E_z(i,j,k)$ is calculated by summing up the magnetic field values of the four neighboring nodes. The magnetic field components are assumed to be constant along the line segments 1-2, 2-3, 3-4, and 4-1, and the electric field component E_z is assumed to be constant over the square surface bounded by 1-2-3-4.

where (i, j, k) stands for the spatial location $(i\Delta x, j\Delta x, k\Delta x)$, and the medium is assumed to be homogeneous. To obtain a suitable time discretization of equation (3.5), it is possible to use the leap-frog scheme. The electric field components are assumed to be constant within the time period $[n\Delta t, (n+1)\Delta t)$, and the magnetic field components are constant within the time period $[(n-1/2)\Delta t, (n+1/2)\Delta t)$. The use of this scheme leads to the following TDFD equation:

$$E_z^{n+1}(i, j, k) = \alpha E_z^n(i, j, k) + \beta \left[H_x^{n+\frac{1}{2}}(i, j-\frac{1}{2}, k) - H_x^{n+\frac{1}{2}}(i, j+\frac{1}{2}, k) + H_y^{n+\frac{1}{2}}(i+\frac{1}{2}, j, k) - H_y^{n+\frac{1}{2}}(i-\frac{1}{2}, j, k) \right] \quad (3.6)$$

where

$$\alpha = \frac{2\varepsilon - \sigma\Delta t}{2\varepsilon + \sigma\Delta t} \quad (3.7)$$

$$\beta = \frac{\Delta t}{\Delta x} \cdot \frac{2}{2\varepsilon + \sigma\Delta t} \quad (3.8)$$

Following the same procedure, the updating equations for the other field components are:

$$\begin{aligned}
E_y^{n+1}(i, j + \frac{1}{2}, k + \frac{1}{2}) &= \alpha E_y^n(i, j + \frac{1}{2}, k + \frac{1}{2}) + \\
&\beta \left[H_z^{n+\frac{1}{2}}(i - \frac{1}{2}, j + \frac{1}{2}, k + \frac{1}{2}) - H_z^{n+\frac{1}{2}}(i + \frac{1}{2}, j + \frac{1}{2}, k + \frac{1}{2}) + \right. \\
&\quad \left. H_x^{n+\frac{1}{2}}(i, j + \frac{1}{2}, k + 1) - H_x^{n+\frac{1}{2}}(i, j + \frac{1}{2}, k) \right]
\end{aligned} \tag{3.9}$$

$$\begin{aligned}
E_x^{n+1}(i + \frac{1}{2}, j, k + \frac{1}{2}) &= \alpha E_x^n(i + \frac{1}{2}, j, k + \frac{1}{2}) + \\
&\beta \left[H_y^{n+\frac{1}{2}}(i + \frac{1}{2}, j, k) - H_y^{n+\frac{1}{2}}(i + \frac{1}{2}, j, k + 1) + \right. \\
&\quad \left. H_z^{n+\frac{1}{2}}(i + \frac{1}{2}, j + \frac{1}{2}, k + \frac{1}{2}) - H_z^{n+\frac{1}{2}}(i + \frac{1}{2}, j - \frac{1}{2}, k + \frac{1}{2}) \right]
\end{aligned} \tag{3.10}$$

$$\begin{aligned}
H_z^{n+\frac{1}{2}}(i + \frac{1}{2}, j + \frac{1}{2}, k + \frac{1}{2}) &= H_z^{n-\frac{1}{2}}(i + \frac{1}{2}, j + \frac{1}{2}, k + \frac{1}{2}) - \\
&\frac{\Delta t}{\Delta x} \cdot \frac{1}{\mu} \left[E_x^n(i + \frac{1}{2}, j, k + \frac{1}{2}) - E_x^n(i + \frac{1}{2}, j + 1, k + \frac{1}{2}) + \right. \\
&\quad \left. E_y^n(i + 1, j + \frac{1}{2}, k + \frac{1}{2}) - E_y^n(i, j + \frac{1}{2}, k + \frac{1}{2}) \right]
\end{aligned} \tag{3.11}$$

$$\begin{aligned}
H_y^{n+\frac{1}{2}}(i + \frac{1}{2}, j, k) &= H_y^{n-\frac{1}{2}}(i + \frac{1}{2}, j, k) - \frac{\Delta t}{\Delta x} \cdot \frac{1}{\mu} \left[E_z^n(i, j, k) - E_z^n(i + 1, j, k) + \right. \\
&\quad \left. E_x^n(i + \frac{1}{2}, j, k + \frac{1}{2}) - E_x^n(i + \frac{1}{2}, j, k - \frac{1}{2}) \right]
\end{aligned} \tag{3.12}$$

$$\begin{aligned}
H_x^{n+\frac{1}{2}}(i, j + \frac{1}{2}, k) &= H_x^{n-\frac{1}{2}}(i, j + \frac{1}{2}, k) - \frac{\Delta t}{\Delta x} \cdot \frac{1}{\mu} \left[E_y^n(i, j + \frac{1}{2}, k - \frac{1}{2}) - E_y^n(i, j + \frac{1}{2}, k + \frac{1}{2}) \right. \\
&\quad \left. + E_z^n(i, j + 1, k) - E_z^n(i, j, k) \right]
\end{aligned} \tag{3.13}$$

3.3 Distortion of the Structure

The updating equations derived in the previous section are valid for homogeneous materials. For inhomogeneous materials, the values of μ , ϵ , and σ have spatial variations as the simulated structure can represent different materials. In such cases, not only are the coefficients α and β spatially dependent, modification of the updating equations may be necessary at material interfaces because of the boundary conditions imposed by Maxwell's equations (such as continuity of the normal component of the electric displacement). With the discretization scheme as shown in

Figure 3.2, it turns out that no modification of the updating equations are necessary to account for changes of material properties. The only modification is that the multiplicative coefficients become spatially dependent, i.e., α becomes $\alpha(i, j, k)$ and β becomes $\beta(i, j, k)$, with $\alpha(i, j, k)$ and $\beta(i, j, k)$ being constant within each node (i, j, k) . The permeability μ is assumed to be constant throughout the simulation domain and is equal to μ_0 since only non-magnetic materials are of interest. Magnetic materials can easily be represented by replacing μ with $\mu(i, j, k)$.

Although no modification is needed for the updating equations, the discretization scheme in Figure 3.2 nevertheless distorts the real structure through its representation of the structure by cubes. An arbitrary volume is represented by cubes with edges parallel to the x -, y - and z -directions. Any material interface is thus approximated by line segments with only three orientations: along the x -direction, the y -direction, and the z -direction. Curved interfaces and slanted interfaces are approximated by stair-cases.

To determine how a structure is distorted by the staggered grid representation is equivalent to finding the exact volume occupied by a node (i, j, k) containing the field variables $E_z(i, j, k)$, $E_x(i + 1/2, j, k + 1/2)$, $E_y(i, j + 1/2, k + 1/2)$, $H_z(i + 1/2, j + 1/2, k + 1/2)$, $H_x(i, j + 1/2, k)$, and $H_y(i + 1/2, j, k)$. In order to achieve this, the boundary conditions imposed by Maxwell's equations must be considered. For example, consider a two-dimensional slice along the xy -plane of the three-dimensional grid as shown in Figure 3.3. Suppose that the node (i, j, k) containing the field variables $H_z(i + 1/2, j + 1/2, k + 1/2)$, $E_z(i + 1/2, j, k + 1/2)$, and $E_y(i, j + 1/2, k + 1/2)$ has different material properties from the neighboring nodes containing the field variables $E_z(i + 1/2, j + 1, k + 1/2)$, and $E_y(i + 1, j + 1/2, k + 1/2)$, the problem is to find the location of the material interface. From Maxwell's equations, the normal component of the electric displacement D is continuous across any interface (assuming that this is no free charge). If an interface exists somewhere within the interval $x = (i\Delta x, (i + 1)\Delta x)$, then Maxwell's equations require that the electric displacement at the interface at one side ($D_{1\perp} = \epsilon_1 E_{1\perp}$) be equal to that at the other side ($D_{2\perp} = \epsilon_2 E_{2\perp}$). However, the updating equation for H_z in the TDFD scheme requires that the electric field components E_x and E_y be constant along each line segment 1-2, 2-3, 3-4, and 4-1, i.e., $E_{1\perp} = E_{2\perp}$. Both conditions together imply that $\epsilon_1 = \epsilon_2$, or there cannot be an interface in the interval $x = (i\Delta x, (i + 1)\Delta x)$ or $y = (j\Delta y, (j + 1)\Delta y)$. Hence,

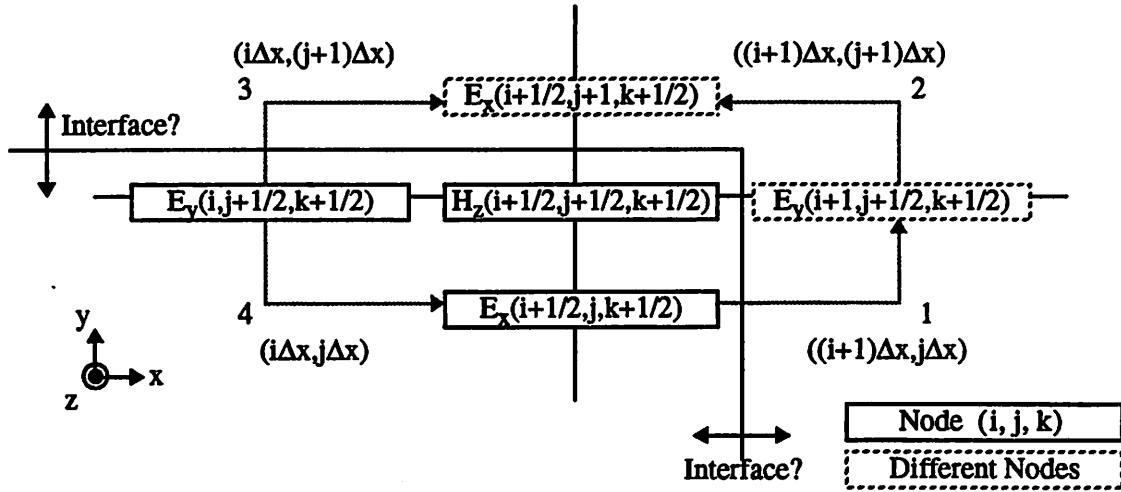


Figure 3.4 Requirements from the TDFD scheme together with Maxwell's equations determine the exact extent of each simulation node (i, j, k) .

the interface must be located at $x = (i + 1) \Delta x$, and $y = (j + 1) \Delta x$. Similar considerations for the other two components of the magnetic field H_x and H_y lead to the conclusion that the volume represented by the node (i, j, k) is a cube of volume Δx^3 defined by $x = [i \Delta x, (i + 1) \Delta x)$, $y = [j \Delta x, (j + 1) \Delta x)$, and $z = [(k - 1/2) \Delta x, (k + 1/2) \Delta x)$. Consideration of the updating equations for the electric field components does not yield additional constraints because all materials are assumed to have the same permeability μ_0 . Both the normal and tangential components of the magnetic field are thus continuous across any material interface.

3.4 Accuracy

As a rough estimation of the accuracy of the TDFD scheme, consider the wave equation resulting from Maxwell's equations in non-conductive materials:

$$\nabla^2 \vec{E} = \mu \epsilon \frac{\partial^2 \vec{E}}{\partial t^2} \quad (3.14)$$

For time-harmonic electromagnetic waves, without loss of generality, the electric field can be assumed to be travelling in the z -direction and polarized in the x -direction with a magnitude E_0 , an angular frequency ω and a wave number κ related to ω by $\kappa = \omega/c$, i.e.,

$\vec{E}(\vec{r}, t) = E_x(z, t) = E_0 \sin(\omega t - \kappa z)$. In continuous space, this sinusoidally varying electric field is an eigenvector of the operator ∇^2 with an eigenvalue of $-\kappa^2$, i.e.,

$$\nabla^2 E_x(z, t) = \frac{\partial^2}{\partial z^2} E_x(z, t) = -\kappa^2 E_x(z, t) \quad (3.15)$$

For finite-difference schemes, the ∇^2 operator can be approximated by the discrete operator D_r^2

$$\nabla^2 \rightarrow D_r^2 = D_z^2 = \frac{1}{\Delta x^2} (K_1 - 2K_0 + K_{-1}) \quad (3.16)$$

where $K_m E(k\Delta x) = E((k+m)\Delta x)$. Operation of D_r^2 on the sinusoidally varying electric field $E_x(z, t)$ results in the following discrete equation:

$$\begin{aligned} D_r^2 E_x(z, t) &= \frac{1}{\Delta x^2} [E((k+1)\Delta x, t) - 2E(k\Delta x, t) + E((k-1)\Delta x, t)] \\ &= \frac{E_0}{\Delta x^2} [\sin(\omega t - \kappa\Delta x(k+1)) - 2\sin(\omega t - \kappa\Delta x k) + \sin(\omega t - \kappa\Delta x(k-1))] \\ &= -2(1 - \cos(\kappa\Delta x)) \sin(\omega t - \kappa z) \end{aligned}$$

Taylor series expansion of $\cos(\kappa\Delta x)$ for small $\kappa\Delta x$ gives the following result:

$$D_r^2 E_x(z, t) = -\kappa^2 \left(1 - \frac{\kappa^2 \Delta x^2}{12}\right) \sin(\omega t - \kappa z) \quad (3.17)$$

The discrete operator D_r^2 thus preserves the eigenvector but gives an error in the eigenvalue. The fractional error in the eigenvalue is $(\kappa^2 \Delta x^2)/12$. In terms of the number of simulation nodes per wavelength $d = (\lambda/\Delta x)$, the relative error, which is defined as the total error in the value of the field divided by the magnitude of the incident field, is given by

$$\text{error}_{\text{rel}} = \frac{\pi^2}{3} \cdot \frac{1}{d^2} \quad (3.18)$$

To achieve a 2% accuracy thus requires a node density of about 13 simulation nodes per wavelength. The d^{-2} dependence of the relative error shows that the operator D_r^2 is second order accurate in space. Following the same procedure, the discrete time derivative operator

$$\frac{\partial^2}{\partial t^2} \rightarrow D_t^2 = \frac{1}{\Delta t^2} (Z_1 - 2Z_0 + Z_{-1}) \quad (3.19)$$

where $Z_m E(n\Delta t) = E((n+m)\Delta t)$ is second order accurate in time as well. The TDFD scheme is thus expected to be second order accurate in both the spatial discretization Δx and the temporal discretization Δt .

The above analysis gives estimations of the error of the discrete operators D_x^2 and D_t^2 . A better estimate of the accuracy of the TDFD scheme described in equations (3.6) to (3.13) can be ascertained from the local truncation error τ . τ is defined as the amount by which the exact solution fails to satisfy the numerical scheme. Let us take equation (3.6) as an example. The updating equation for E_z is repeated here:

$$E_z^{n+1}(i, j, k) = \alpha E_z^n(i, j, k) + \beta \left[H_x^{n+\frac{1}{2}}(i, j - \frac{1}{2}, k) - H_x^{n+\frac{1}{2}}(i, j + \frac{1}{2}, k) + H_y^{n+\frac{1}{2}}(i + \frac{1}{2}, j, k) - H_y^{n+\frac{1}{2}}(i - \frac{1}{2}, j, k) \right]$$

The exact solution can be found by Taylor series expansion of each individual term in the above equation around the spatial point $(i\Delta x, j\Delta y, k\Delta z)$ and at time $(n + 1/2)\Delta t$. For instance,

$$E_z^{n+1}(i, j, k) = E_z^{n+\frac{1}{2}}(i, j, k) + \frac{\Delta t}{2} \frac{\partial}{\partial t} E_z^{n+\frac{1}{2}}(i, j, k) + \frac{\Delta t^2}{8} \frac{\partial^2}{\partial t^2} E_z^{n+\frac{1}{2}}(i, j, k) + \frac{\Delta t^3}{48} \frac{\partial^3}{\partial t^3} E_z^{n+\frac{1}{2}}(i, j, k) + \frac{\Delta t^4}{384} \frac{\partial^4}{\partial t^4} E_z^{n+\frac{1}{2}}(i, j, k) + \frac{\Delta t^5}{3840} \frac{\partial^5}{\partial t^5} E_z^{n+\frac{1}{2}}(i + \theta, j + \phi, k + \eta) \quad (3.20)$$

where $0 \leq \theta, \phi, \eta \leq 1$. Expanding all the terms in equation (3.6) results in the following expression for the local truncation error:

$$\tau = (\alpha - 1) E_z - \frac{\Delta t}{2} (\alpha + 1) \frac{\partial E_z}{\partial t} + \frac{\Delta t^2}{8} (\alpha - 1) \frac{\partial^2 E_z}{\partial t^2} - \frac{\Delta t^3}{48} (\alpha + 1) \frac{\partial^3 E_z}{\partial t^3} + \frac{\Delta t^4}{384} (\alpha - 1) \frac{\partial^4 E_z}{\partial t^4} + \beta \left[\Delta x \frac{\partial H_y}{\partial x} - \Delta x \frac{\partial H_x}{\partial y} + \frac{\Delta x^3}{24} \frac{\partial^3 H_y}{\partial x^3} - \frac{\Delta x^3}{24} \frac{\partial^3 H_x}{\partial y^3} \right] + O(\Delta t^5 + \Delta x^5) \quad (3.21)$$

where all the derivatives are evaluated at the spatial location $(i\Delta x, j\Delta y, k\Delta z)$ and at time $(n + 1/2)\Delta t$. This expression of τ can be simplified by considering the z-component of the Faraday's law:

$$\frac{\partial H_y}{\partial x} - \frac{\partial H_x}{\partial y} = \epsilon \frac{\partial E_z}{\partial t} + \sigma E_z \quad (3.22)$$

All the first order terms involving Δx and Δt are cancelled and the local truncation error becomes

$$\tau = \frac{\Delta t}{\epsilon + \frac{\sigma \Delta t}{2}} \left\{ \left[-\sigma \frac{\Delta t^2 \partial^2 \mathbf{E}_z}{8 \partial t^2} - 2\epsilon \frac{\Delta t^2 \partial^3 \mathbf{E}_z}{48 \partial t^3} \right] + \left[\frac{\Delta x^2 \partial^3 \mathbf{H}_y}{24 \partial x^3} - \frac{\Delta x^2 \partial^3 \mathbf{H}_x}{24 \partial y^3} \right] \right\} \quad (3.23)$$

To estimate the magnitude of the local truncation error, approximations of the derivatives as well as the values of ϵ and σ are necessary. The magnitudes of the derivatives can be estimated by

$$\left| \frac{\partial \mathbf{E}_z}{\partial t} \right| \equiv \omega |\mathbf{E}_z|$$

$$\left| \frac{\partial \mathbf{H}_y}{\partial x} \right| \equiv \left| \frac{\partial \mathbf{H}_y}{\partial x} \right| \equiv \kappa \left| \frac{\mathbf{E}_z}{\eta} \right| = \frac{\omega}{c} \left| \frac{\mathbf{E}_z}{\eta} \right|$$

where κ is the wave number, ω is the angular frequency of the incident radiation, c is the phase velocity of the medium, and η is the intrinsic impedance of the material, and

$$\omega = ck = \frac{2\pi c}{\lambda} \quad (3.24)$$

From stability considerations (which are discussed in §3.5), the relation between Δt and Δx is

$$\Delta t \leq \frac{\Delta x}{c\sqrt{3}} \quad (3.25)$$

The relative error of the scheme is thus estimated to be

$$\text{error}_{\text{rel}} = \frac{4\pi^2 (\epsilon_i/24 + 7\epsilon_r/72)}{\epsilon_r + (1.77\epsilon_i/d)} \cdot \frac{1}{d^2} \quad (3.26)$$

where d is the density of simulation nodes per wavelength, and ϵ_r and ϵ_i are respectively the real and imaginary parts of the relative permittivity of the material. Notice in equation (3.26) that the relative error is no longer second order accurate in the spatial discretization Δx when the material is lossy. In the limit when $\epsilon_i \gg \epsilon_r$, the relative error varies as d^{-1} instead of d^{-2} and the TDFD scheme is only first order accurate. Such cases arise when the magnitudes of the real and imaginary parts of the refractive index are comparable because $\epsilon_r = n_r^2 - n_i^2$ and $\epsilon_i = 2n_r n_i$. Only for lossless materials does the TDFD scheme retain the second order accurate behavior. For slightly lossy materials in which $\epsilon_r \geq \epsilon_i$, the TDFD scheme still possesses a nearly second order behavior

so long as $d > 2$ because the first term in the denominator (ϵ_r) dominates over the second term ($1.77\epsilon_i/d$). As an example, consider silicon at a wavelength of $0.365 \mu\text{m}$. The refractive index is $(6.522, -j2.705)^{71}$. In the MKS system of units, this gives a permittivity of $35.2\epsilon_0$ ($\epsilon_r=35.2$) and a conductivity of $35.3\omega\epsilon_0$ ($\epsilon_i=35.3$). The estimated relative error is 2% with a node density of 15 per wavelength, agreeing with the estimation from the D_r^2 and D_t^2 operators.

To determine how well the theoretical prediction of accuracy corresponds with the numerical results, simulation runs with different node densities (values of d) are carried out on a planar dielectric stack consisting of three lossless layers of refractive indexes of 1 (semi-infinite), 2 (of thickness $1.0 \mu\text{m}$), and 4 (semi-infinite), respectively. The free space wavelength of the incident radiation is $0.5 \mu\text{m}$. The simulated steady-state electric field amplitudes in the middle layer are compared with the exact solution calculated from the Fresnel equation³¹ as shown in Figure 3.5. With a node density of 4 nodes per wavelength in the optically densest material, the relative error is approximately 25%. The relative error for 8 nodes per wavelength is about 5%. For 16 nodes per wavelength, the relative error is less than 2%. This is consistent with the theoretical calculation that the relative error varies as $1/d^2$ and is about 2% with 15 nodes per wavelength.

An interesting point to note in Figure 3.5 is the apparent increase in the wave number as the node density is lowered. This is due to the increased difference between the actual dispersion relation $\kappa = \omega/c$ and the numerical dispersion relation as the node density decreases. The numerical dispersion relation is given by¹⁸:

$$\left(\frac{1}{\Delta x^2} \sin^2 \left(\frac{1}{2} \kappa_x \Delta x \right) + \frac{1}{\Delta y^2} \sin^2 \left(\frac{1}{2} \kappa_y \Delta y \right) + \frac{1}{\Delta z^2} \sin^2 \left(\frac{1}{2} \kappa_z \Delta z \right) \right)^{1/2} = \sin \left(\frac{1}{2} \omega \Delta t \right) \quad (3.27)$$

3.5 Stability

Engquist et al.¹⁸ have shown that the TDFD scheme described in equations (3.6) to (3.13) is unstable unless the temporal discretization Δt and the spatial discretization Δx satisfy the following relation:

$$\Delta t \leq \left(\frac{1}{\Delta x^2} \sin^2 \left(\frac{1}{2} \kappa_x \Delta x \right) + \frac{1}{\Delta y^2} \sin^2 \left(\frac{1}{2} \kappa_y \Delta y \right) + \frac{1}{\Delta z^2} \sin^2 \left(\frac{1}{2} \kappa_z \Delta z \right) \right)^{-1/2} \quad (3.28)$$

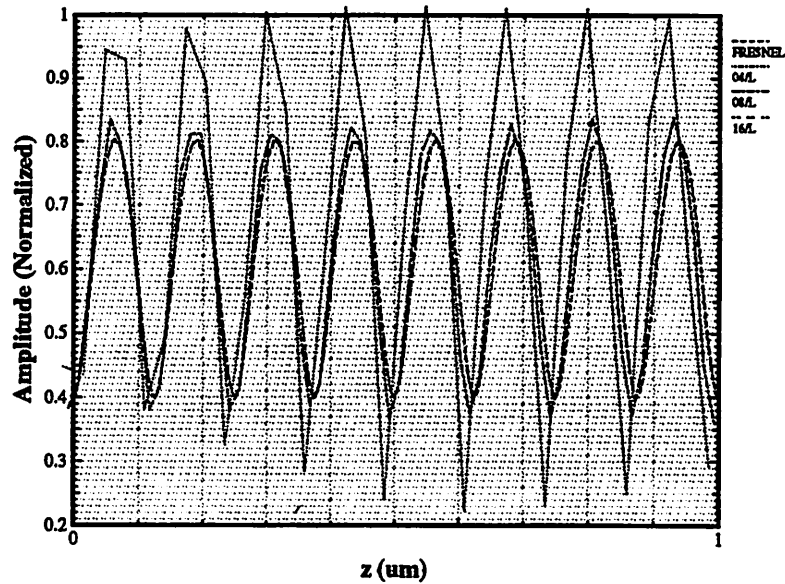


Figure 3.5 TEMPEST calculated electric field amplitude of a 3-layer planar dielectric stack with different node densities. A relative error of less than 2% can be achieved with 15 nodes per wavelength in the region with the highest refractive index.

for arbitrary κ_x , κ_y , and κ_z . Since $0 \leq \sin^2(\kappa_x \Delta x / 2) \leq 1$, and $\Delta x = \Delta y = \Delta z$, equation (3.28) reduces to

$$\Delta t \leq \frac{\Delta x}{c \sqrt{\text{dim}}} \quad (3.29)$$

The factor dim in equation (3.29) represents the number of dimensions of the structure. For a planar structure, $\text{dim} = 1$. For a structure which is uniform across one of the dimensions such as a photoresist line, $\text{dim} = 2$. For a general structure, $\text{dim} = 3$.

However, equation (3.29) provides only a necessary condition for the TDFD scheme to be stable. To guarantee stability, it turns out that the magnitude of the real part of the refractive index n_r must be greater than the imaginary part n_i . In other words, $\epsilon_r = (n_r^2 - n_i^2) > 0$. To demonstrate this, consider a two-dimensional structure in the TE polarization. The TE polarization is defined in such a way that the electric field is parallel to all surfaces, i.e., the electric field is polarized such that it oscillates perpendicular to the plane of the structure. Under this special case, only three out of the six equations of the TDFD scheme remain:

$$\begin{aligned} E_z^{n+1}(i, j) &= \alpha E_z^n(i, j) + \\ &\beta \left[H_x^{n+\frac{1}{2}}(i, j-\frac{1}{2}) - H_x^{n+\frac{1}{2}}(i, j+\frac{1}{2}) + H_y^{n+\frac{1}{2}}(i+\frac{1}{2}, j) - H_y^{n+\frac{1}{2}}(i-\frac{1}{2}, j) \right] \end{aligned} \quad (3.30)$$

$$H_x^{n+\frac{1}{2}}(i, j+\frac{1}{2}) = H_x^{n-\frac{1}{2}}(i, j+\frac{1}{2}) - \gamma [E_z^n(i, j+1) - E_z^n(i, j)] \quad (3.31)$$

$$H_y^{n+\frac{1}{2}}(i+\frac{1}{2}, j) = H_y^{n-\frac{1}{2}}(i+\frac{1}{2}, j) - \gamma [E_z^n(i, j) - E_z^n(i+1, j)] \quad (3.32)$$

where α and β are given in equations (3.7) and (3.8), and $\gamma = \mu (\Delta t / \Delta x)$. To determine stability for this scheme, the Fourier analysis is used. Consider the discrete Fourier transform of E_z :

$$\hat{E}_z(\theta_1, \theta_2) = \sum_i \sum_j E_z(i, j) e^{\sqrt{-1}(i\theta_1 + j\theta_2)} \quad (3.33)$$

The two-norms of $E_z(i, j)$ and $\hat{E}_z(\theta_1, \theta_2)$ are related by Parseval's theorem:

$$\sum_i \sum_j |E_z(i, j)|^2 = \frac{1}{4\pi^2} \int_0^{2\pi} \int_0^{2\pi} |\hat{E}_z(\theta_1, \theta_2)|^2 d\theta_1 d\theta_2 \quad (3.34)$$

The "energy" in the time-domain variable E_z is therefore equivalent to the integrated spectral energy.

Fourier transformation of equations (3.6) to (3.32) results in the following equations in the frequency space of θ_1 and θ_2 :

$$\begin{aligned} \hat{E}_z^{n+1}(\theta_1, \theta_2) &= \hat{E}_z^n [\alpha + 4\beta\gamma(\sin^2(\theta_1/2) + \sin^2(\theta_2/2))] + \\ &\hat{H}_x^n [i2\beta \sin(\theta_2/2)] + \hat{H}_y^n [-i2\beta \sin(\theta_1/2)] \end{aligned} \quad (3.35)$$

$$\hat{H}_x^{n+1}(\theta_1, \theta_2) = \hat{H}_x^n + \hat{E}_z^n [i2\gamma \sin(\theta_2/2)] \quad (3.36)$$

$$\hat{H}_y^{n+1}(\theta_1, \theta_2) = \hat{H}_y^n + \hat{E}_z^n [-i2\gamma \sin(\theta_1/2)] \quad (3.37)$$

The above equations can be written in terms of a system of equations as $\hat{F}^{n+1} = A(\theta_1, \theta_2) \hat{F}^n$ where

$$\hat{F}^n = (\hat{E}_z^n, \hat{H}_x^n, \hat{H}_y^n)^T \text{ and}$$

$$A(\theta_1, \theta_2) = \begin{bmatrix} \alpha + 4\beta\gamma(\sin^2(\theta_1/2) + \sin^2(\theta_2/2)) & i2\beta\sin(\theta_2/2) & -i2\beta\sin(\theta_1/2) \\ i2\gamma\sin(\theta_2/2) & 1 & 0 \\ -i2\gamma\sin(\theta_1/2) & 0 & 1 \end{bmatrix} \quad (3.38)$$

Parseval's theorem then gives

$$\|F^{n+1}\|_2 = 4\pi^2 \int_0^{2\pi} \int_0^{2\pi} |A\hat{F}^n|^2 d\theta_2 d\theta_1 \leq \|A^{n+1}\|_\infty \|F^0\|_2 \quad (3.39)$$

Assuming that A can be diagonalized, i.e., $A = XDX^{-1}$, equation (3.39) becomes

$$\|F^{n+1}\|_2 = 4\pi^2 \int_0^{2\pi} \int_0^{2\pi} |A\hat{F}^n|^2 d\theta_2 d\theta_1 \leq \|XD^{n+1}X^{-1}\|_\infty \|F^0\|_2 \quad (3.40)$$

The TDFD scheme is thus two-norm stable if $\|D\|_\infty \leq 1$ and if X is bounded. The former condition means that the magnitude of the eigenvalues of the matrix A must be bounded by 1; the latter condition implies that the eigenvectors of A must not blow up when the spatial and temporal discretizations Δx and Δt approach zero. To verify the former condition, the characteristic equation for the matrix is

$$(\lambda - 1) [\lambda^2 + \lambda(4\beta\gamma\{\sin^2(\theta_1/2) + \sin^2(\theta_2/2)\} - \alpha - 1) + \alpha] = 0 \quad (3.41)$$

Denoting $\sin^2(\theta_1/2) + \sin^2(\theta_2/2)$ by Λ , the eigenvalues are $\lambda_1 = 1$, and

$$\lambda_{2,3} = \frac{1}{2} [(\alpha + 1 - 4\beta\gamma\Lambda) \pm \sqrt{16\beta^2\gamma^2\Lambda^2 - 8\beta\gamma\Lambda(\alpha + 1) + (\alpha - 1)^2}] \quad (3.42)$$

The magnitudes of $\lambda_{2,3}$ in equation (3.42) is less than or equal to 1 if and only if $\epsilon > 0$ and $c\Delta t/\Delta x < 1/\sqrt{2}$. (The factor under the square root sign corresponds to the number of dimensions and is 2 in this case.) The latter requirement corresponds to that derived by Engquist¹⁸, but the former is also necessary for the TDFD scheme to be stable. The condition $\epsilon > 0$ puts a constraint on the allowable material properties. Since $\epsilon = n_t^2 - n_i^2$, this condition means that only materials with $n_t > n_i$ can be studied. This is a severe restriction as the refractive indexes of a lot of commonly used materials in the fabrication of integrated circuits shown in Table 3.1 possess the quality that $n_i > n_t$. The problem of simulation of highly dispersive materials, i.e., materials in which $n_i > n_t$, is tackled in Chapter 5.

Material	0.365 μm	0.248 μm	0.213 μm	0.193 μm
Silicon	6.522, -j2.705	1.68, -j3.58	1.119, -j3.025	0.883, -j2.778
Chromium	1.40, -j3.26	0.85, -j2.01	0.967, -j1.737	0.84, -j1.65
Photoresist	~(1.58*, -j0.02)	~(1.65*, -j0.02)	~(1.68, -j0.02)	~(1.68, -j0.02)
Oxide (glass)	1.47453, -j0	1.50841, -j0	1.53429, -j0	1.563, -j0
a-silicon	3.90, -j2.66	1.69, -j2.76	1.19, -j2.36	0.974, -j2.10
Nitride	2.093, -j0	2.278, -j0.005	2.468 -j0.07	2.66, -j0.243
Tungsten	3.39, -j2.66	3.40, -j2.85	2.0, -j3.61	1.30, -j3.02
Gold	1.716, -j1.862	1.484, -j1.636	1.432, -j1.364	1.425, -j1.156
GaAs	3.596, -j2.076	2.273, -j4.084	1.311, -j2.625	1.358, -j2.013

Table 3.1 Refractive indexes of commonly used materials in the fabrication of integrated circuits⁷¹.
*Kodak KTRF photoresist⁹⁴.

To verify the latter condition for stability, i.e., the boundedness of the eigenvectors of A , notice that the eigenvectors

$$\hat{u}_i = ((1 - \lambda_i), -\sqrt{-12\gamma\sin(\theta_2/2)}, \sqrt{-12\gamma\sin(\theta_1/2)}) \text{ where } i = 1, 2, 3 \quad (3.43)$$

are bounded when Δx and Δt approach zero.

3.6 Conclusions

A three-dimensional TDFD numerical scheme for solving Maxwell's equations is formulated for implementation on the connection machine. This scheme is shown to be second order accurate (except for materials with the property that $\epsilon_i \gg \epsilon_r$), with a relative error of 2% when the simulation node density is 15 per wavelength. It is also stable provided that both the ratio of the spatial discretization Δx to the temporal discretization Δt is greater than the speed of light multiplied by $\sqrt{3}$ and the real part of the refractive index is larger than the imaginary part. The problem of modeling of highly dispersive materials is presented in Chapter 5. In the next chapter, numerical boundary conditions used to terminate the simulation domain are discussed.

Chapter 4

Numerical Boundary Conditions

4.1 Introduction

In simulation of electromagnetic scattering, there is a need to confine the area of computation due to computer memory and CPU limitations. This leads to the introduction of artificial boundaries surrounding the simulation domain. Ideally, these artificial boundaries should not affect the propagation of electromagnetic waves, i.e., they should annihilate the outward-going waves. These absorbing boundary conditions require special attention because boundary conditions with poor absorbing properties can cause a significant amount of artificial reflection which in turn can lead to inaccurate simulation results. At the same time, these numerical boundary conditions should not require too much computation resource because they decrease the overall computation efficiency as they lead to equations at the boundaries which are distinct from those in the interior simulation domain described in Chapter 3. This decrease in efficiency is especially significant for massively-parallel computer architectures such as the connection machine CM-2 because the interior simulation nodes are idled during calculations at the boundary nodes.

Taylor et al.⁸⁵, Taflove and Brodwin⁸³, Merewether⁵⁸, and Kunz and Lee³⁹ had proposed different time-domain finite-difference boundary conditions in the early 1970s. These boundary conditions were further refined by Mur⁶¹, and Engquist and Majda^{17,18} around 1980. In recent years, Higdon²⁸ proposed a stable boundary condition with a one-dimensional spatial stencil; and Mei⁵⁶ also proposed the superabsorption method which is based on error cancellation between the artificially reflected electric and magnetic fields. Furthermore, from a mathematical point of view, Trefethen^{91,92} discussed the stability and well-posedness of absorbing boundary conditions. A review and comparison of these boundary conditions can be found in Blaschak³ and Renaut⁷⁷. These different numerical absorbing boundary conditions proposed in the literature are all based on the discretization of spatially and temporally continuous boundary operators. In this chapter, these continuous boundary operators and their absorption properties are first described. A novel

numerical boundary condition based not on boundary operators but on the harmonic nature of the wave is then derived and compared with the boundary conditions proposed by Mur⁶¹ and Higdon²⁸.

4.2 Continuous Boundary Conditions

Consider the three-dimensional wave equation:

$$\frac{\partial^2 \vec{E}}{\partial t^2} - \nabla^2 \vec{E} = \frac{\partial^2 \vec{E}}{\partial t^2} - c^2 \left(\frac{\partial^2 \vec{E}}{\partial x^2} + \frac{\partial^2 \vec{E}}{\partial y^2} + \frac{\partial^2 \vec{E}}{\partial z^2} \right) = 0 \quad (4.1)$$

A solution to the equation is:

$$\vec{E} = \vec{E}_0 \exp(\sqrt{-1} (\omega t + \kappa_x x + \kappa_y y + \kappa_z z)) \quad (4.2)$$

The wave numbers κ_x , κ_y , and κ_z are related through:

$$\kappa_x^2 + \kappa_y^2 + \kappa_z^2 = \kappa^2 \quad (4.3)$$

where

$$\kappa = \frac{2\pi}{\lambda} = \frac{\omega}{c} \quad (4.4)$$

For waves travelling in the -z-direction, the following relation is satisfied:

$$\left(\frac{\partial E}{\partial z} - \sqrt{-1} \kappa_z E \right) \Big|_{z = \text{boundary}} = 0 \quad (4.5)$$

In general, κ_z can take on any value between 0 and κ . In numerical implementation, however, the value of κ_z must be fixed at some value κ_{z0} . Thus, equation (4.5) becomes

$$B[E] = \left(\frac{\partial}{\partial z} - \sqrt{-1} \kappa_{z0} \right) \Big|_{z = \text{boundary}} E = 0 \quad (4.6)$$

where B is the (continuous) boundary operator. This boundary operator is perfectly absorbing provided that the wave approaches the boundary with a wave number in the z-direction equal to κ_{z0} . In most applications, however, waves generally approach the boundary from different directions. In these cases, the boundary condition in equation (4.6) is no longer perfectly absorbing. It produces artificial reflections. To determine the reflection coefficient, assume that at the boundary, the electric field is given by:

$$\vec{E} = \hat{a} \cdot \exp(\sqrt{-1} (\omega t + \kappa_x x + \kappa_y y - \kappa_z z)) + \hat{b} \cdot \exp(\sqrt{-1} (\omega t + \kappa_x x + \kappa_y y + \kappa_z z)) \quad (4.7)$$

where $|\hat{a}|$ is the outward-going wave amplitude and $|\hat{b}|$ is the artificially reflected wave amplitude. Substituting this expression of the electric field into the boundary equation (4.6) gives a reflection coefficient of

$$|R| = \left| \frac{\hat{b}}{\hat{a}} \right| = \left| \frac{\cos\theta - \cos\theta_0}{\cos\theta + \cos\theta_0} \right| \quad (4.8)$$

where θ is the angle between the wave propagation direction and the normal of the boundary (which will be called the exiting angle from now on), and $\kappa_{z0} = \kappa\cos\theta_0$, i.e., the boundary condition is perfectly absorbing for waves propagating with an exiting angle of θ_0 . The reflection coefficient as a function of the exiting angle with different values of the perfect absorption angle θ_0 is shown in Figure 4.1. The figure shows that as θ_0 is increased from zero, reflection at small exiting angles becomes larger; but reflection for exiting angles around θ_0 is small. From this observation, one might expect that the larger the perfect absorption angle is, the smaller the reflection coefficient for exiting angles close to 90° . Figure 4.1 shows, however, that for any perfect absorption angle $\theta_0 = [0^\circ, 90^\circ)$, the reflection coefficient always approaches 1.0 as the exiting angle approaches 90° .

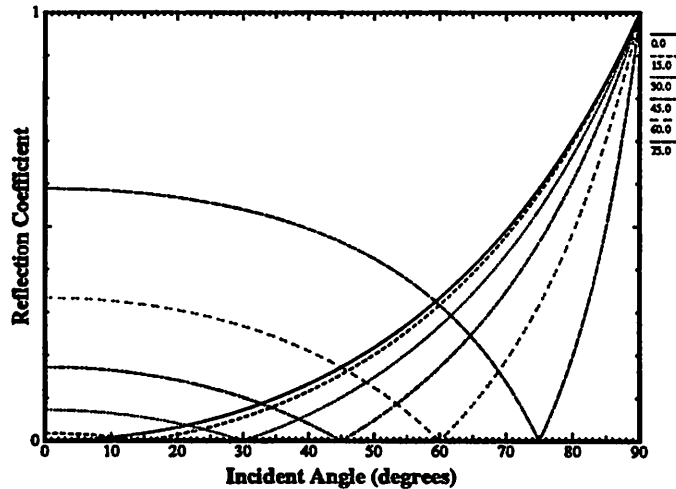


Figure 4.1 The reflection coefficient as a function of exiting angle for different values of perfect absorption angle θ_0 . The reflection coefficient is 1 at 90° regardless of the value of θ_0 .

The boundary operator in equation (4.6) with the reflection coefficient calculated above is first order only. For a perfect absorption angle of 0° , the reflection coefficient at 45° is 0.17. This

means that application of the boundary operator would result in a 17% error in the electric field value for waves exiting at an angle of 45°. To improve the absorbing property of the boundary operator, two approaches can be taken. In the first method, κ_z in equation (4.5) is expanded as a Taylor series. Keeping the higher order terms result in a higher order boundary conditions. This is the approach adopted by Mur⁶¹. In the second method, boundary operators with different values of κ_{z0} are multiplied together, resulting in a higher order boundary operator. This is the approach adopted by Higdon²⁸. These two methods are described in detail below.

4.2.1 Mur's Method

To illustrate Mur's method, assume without loss of generality that $\kappa_{z0} \approx \kappa$. Then equation (4.5) can be written as

$$\left. \left(\frac{\partial E}{\partial z} - \sqrt{-1} \sqrt{(\kappa^2 - \kappa_x^2 - \kappa_y^2)} E \right) \right|_{z = \text{boundary}} = 0 \quad (4.9)$$

Assuming that κ_x and κ_y are small and utilizing equation (4.4), Taylor series expansion of equation (4.9) results in the following equation:

$$\left. \left(\frac{\partial E}{\partial z} - \frac{\sqrt{-1} \omega}{c} \left(1 - \frac{1}{2} \left(\frac{\kappa_x^2 + \kappa_y^2}{\kappa^2} \right) + \dots \right) E \right) \right|_{z = \text{boundary}} = 0 \quad (4.10)$$

Keeping only the first two terms of the series and identifying $\sqrt{-1} \omega$ with $\partial/\partial t$, the second order boundary operator is:

$$B_{2_{\text{mur}}} [E] = \left[\frac{\partial^2}{\partial z \partial t} - \frac{1}{c} \frac{\partial^2}{\partial t^2} + \frac{c}{2} \left(\frac{\partial^2}{\partial x^2} + \frac{\partial^2}{\partial y^2} \right) \right] E = 0 \quad (4.11)$$

The reflection coefficient of this boundary operator is given by

$$|R_{2_{\text{mur}}}| = \left| \frac{\cos \theta - \cos \theta_0}{\cos \theta + \cos \theta_0} \right|^2 \quad (4.12)$$

With θ_0 equal to 0°, the reflection coefficient for waves exiting at 45° is only 3%, reduced from 17% of the first order boundary condition. Higher order boundary operators can be derived by keeping more terms in the Taylor series expansion in equation (4.10).

4.2.2 Higdon's Method

Another way to obtain higher order boundary operators is to multiply together first order boundary operators with different values of κ_{z0} . This is Higdon's approach. In this method, the boundary operator in equation (4.6) is modified to read

$$B_{1_{\text{higdon}}} [E] = \left(\frac{\partial}{\partial t} - \frac{\omega}{\kappa_{z0}} \frac{\partial}{\partial z} \right) E = \left(\frac{\partial}{\partial t} - \frac{c}{\cos\theta_0} \frac{\partial}{\partial z} \right) E = 0 \quad (4.13)$$

Then an n^{th} order boundary operator can be written as

$$B_{n_{\text{higdon}}} [E] = \prod_{j=1}^n \left(\frac{\partial}{\partial t} - \frac{c}{\cos\theta_{0j}} \frac{\partial}{\partial z} \right) E = 0 \quad (4.14)$$

For example, a second order boundary condition is

$$B_{2_{\text{higdon}}} [E] = \left(\frac{\partial}{\partial t} - \frac{c}{\cos\theta_{0_1}} \frac{\partial}{\partial z} \right) \left(\frac{\partial}{\partial t} - \frac{c}{\cos\theta_{0_2}} \frac{\partial}{\partial z} \right) E = 0 \quad (4.15)$$

and the reflection coefficient is

$$|R_{2_{\text{higdon}}}| = \left| \frac{\cos\theta - \cos\theta_{0_1}}{\cos\theta + \cos\theta_{0_1}} \right| \left| \frac{\cos\theta - \cos\theta_{0_2}}{\cos\theta + \cos\theta_{0_2}} \right| \quad (4.16)$$

4.3 Discretization of the Boundary Operators

From the expression for the two second order boundary operators in equations (4.11) and (4.15), one can see that Higdon's approach would result in a more efficient discretization scheme in three-dimensional electromagnetic simulation as it requires a three-level one-dimensional spatial (in the z -direction) and a three-level temporal stencil. For the Mur method, a three-level three-dimensional spatial and a three-level temporal stencil is required. Higdon's method is thus preferred over Mur's approach because of a smaller stencil. For two-dimensional applications, however, since the number of field components is three instead of six, the Mur boundary operator of equation (4.11) can be simplified. Assuming the TE polarization with only one electric field component in the x -direction and two magnetic field components in the y - and z -directions. Ampere's law then gives

$$\frac{\partial E_x}{\partial z} = -\frac{\partial B_y}{\partial t} \text{ and } \frac{\partial E_x}{\partial y} = \frac{\partial B_z}{\partial t} \quad (4.17)$$

and the second order boundary operator becomes

$$B_{2_{\text{mur}}}^{2-D} [E, H] = \frac{\partial E}{\partial y} + \frac{1}{c} \frac{\partial E}{\partial t} + \frac{c\mu}{2} \frac{\partial H_y}{\partial z} = 0 \quad (4.18)$$

This two-dimensional boundary operator involves only first order derivatives. The discretized equation for a wave travelling in the -z-direction becomes

$$E_{i,j,0}^{n+1} = E_{i,j,1}^n - \left(\frac{c\Delta t - n\Delta x}{c\Delta t + n\Delta x} \right) E_{i,j,0}^n + \frac{\mu c^2 \Delta t}{2n(c\Delta t + n\Delta x)} \left[H_{z,i,j+1/2,1}^{n+\frac{1}{2}} - H_{z,i,j-1/2,1}^{n+\frac{1}{2}} + H_{z,i,j+1/2,0}^{n+\frac{1}{2}} - H_{z,i,j-1/2,0}^{n+\frac{1}{2}} \right] + \left(\frac{c\Delta t - n\Delta x}{c\Delta t + n\Delta x} \right) E_{i,j,1}^{n+1} \quad (4.19)$$

where $i\Delta x$ and $j\Delta x$ are respectively the abscissa and ordinate (the index i is constant in this case as the structure is only two-dimensional), and the third index represents the z-position. A value of 0 represents the boundary node, and a value of 1 represents the first node inside the simulation domain. For waves travelling in other directions, the boundary equations are easily derived by coordinate transformation.

For three-dimensional applications, however, the relation among the derivatives of the electric and magnetic field components in equation (4.17) no longer holds, and the stencil becomes three-dimensional in space. In this case, Higdon's boundary operator is more advantageous. In order to discretize the continuous boundary operator of equation (4.13), Higdon proposed the following discrete boundary operator

$$D'_{1_{\text{higdon}}} (K, Z^{-1}) = \left(\frac{I - Z^{-1}}{\Delta t} \right) [(1-a)I + aK] - \frac{c}{\cos\theta_0} \left(\frac{K - I}{\Delta x} \right) [(1-b)I + bZ^{-1}] \quad (4.20)$$

where K and Z denote the forward shift operators with respect to space and time respectively, i.e., $Ku_{i,j,k}^n = u_{i,j,k+1}^n$ and $Zu_{i,j,k}^n = u_{i,j,k}^{n+1}$; I is the identity. The coefficients a and b represent respectively the weighted space and time averages of the temporal and spatial differences. Equation (4.20) gives the following discretized boundary equation:

$$D_{1_{\text{higdon}}} [E] = (I + \alpha K - \beta Z^{-1} - \gamma KZ^{-1}) E = 0 \quad (4.21)$$

with the coefficients α , β , and γ given by

$$\alpha = \frac{a\kappa\cos\theta_0\Delta x - (1-b)\omega\Delta t}{(1-a)\kappa\cos\theta_0\Delta x + (1-b)\omega\Delta t}, \beta = \frac{(1-a)\kappa\cos\theta_0\Delta x - b\omega\Delta t}{(1-a)\kappa\cos\theta_0\Delta x + (1-b)\omega\Delta t}, \text{ and}$$

$$\gamma = \frac{a\kappa\cos\theta_0\Delta x + b\omega\Delta t}{(1-a)\kappa\cos\theta_0\Delta x + (1-b)\omega\Delta t} \quad (4.22)$$

With values of $a = 0.5$ and $b = 0.5$ (center differencing), a first order discretized boundary equation becomes

$$D_{1_{\text{higdon}}} [E] \Rightarrow E_{i,j,0}^{n+1} = E_{i,j,1}^n + \frac{\omega\Delta t - \kappa_{z0}\Delta x}{\omega\Delta t + \kappa_{z0}\Delta x} [E_{i,j,1}^{n+1} - E_{i,j,0}^n] \quad (4.23)$$

A second order equation can be derived by twice applying the discretized boundary operator $D_{1_{\text{higdon}}}$ on the electric field, resulting in the following relation:

$$D_{2_{\text{higdon}}} [E] \Rightarrow E_{i,j,0}^{n+1} = [-(\alpha_1 + \alpha_2)K - \alpha_1\alpha_2K^2 + (\beta_1 + \beta_2)Z^{-1} +$$

$$(\gamma_1 + \gamma_2 + \alpha_1\beta_2 + \alpha_2\beta_1)KZ^{-1} + (\alpha_1\gamma_2 + \alpha_2\gamma_1)K^2Z^{-1} - \beta_1\beta_2Z^{-2} - (\beta_1\gamma_2 + \beta_2\gamma_1)KZ^{-2}$$

$$- \gamma_1\gamma_2K^2Z^{-2}] E_{i,j,0}^{n+1} \quad (4.24)$$

The parameters α_1, α_2 , etc., can be adjusted by setting θ_{0_1} and θ_{0_2} such that the boundary condition is perfectly absorbing for exiting angles of θ_{0_1} and θ_{0_2} . For practical applications, θ_{0_1} and θ_{0_2} are chosen to be the directions in which the most wave energy propagate.

4.4 A Novel Boundary Condition

The discretized boundary relation of equation (4.21) indicates that the field value of the boundary node $E_{i,j,0}^{n+1}$ is a linear combination of the three field values $E_{i,j,1}^{n+1}$, $E_{i,j,0}^n$, and $E_{i,j,1}^n$. However, since the electromagnetic field components vary in a harmonic fashion, the value of any field component at any point and instant should be determined by its amplitude and phase only. Thus, theoretically speaking, only two parameters are necessary to specify the value of any boundary point at any instant of time. In other words, $E_{i,j,0}^{n+1}$ can be given by a linear combination of two field values instead of three as in equation (4.21).

To derive such a relationship, assume that the field varies harmonically with an angular frequency ω as follows:

$$E(x, y, z, t) = A \sin(\omega t + \kappa_{x0}x + \kappa_{y0}y + \kappa_{z0}z + \Omega) \quad (4.25)$$

where A is the amplitude and Ω is an arbitrary phase. With this form, the field value of an arbitrary node at any time step can be written as

$$E_{i,j,k}^{n+1-m} = A \sin(\phi - \omega m \Delta t + \kappa_{z0}k \Delta x) \quad (4.26)$$

where $\phi = \omega(n+1)\Delta t + \kappa_{x0}i\Delta x + \kappa_{y0}j\Delta x + \Omega$. Thus, in terms of ϕ , $E_{i,j,0}^{n+1} = \sin\phi$, $E_{i,j,1}^{n+1} = \sin(\phi + \kappa_{z0}\Delta x)$, and $E_{i,j,0}^n = \sin(\phi - \omega\Delta t)$. Expanding the arguments for $E_{i,j,1}^{n+1}$ and $E_{i,j,0}^n$ results in the following set of simultaneous equations:

$$\begin{bmatrix} \cos \kappa_{z0}\Delta x & \sin \kappa_{z0}\Delta x \\ \cos \omega\Delta t & -\sin \omega\Delta t \end{bmatrix} \begin{bmatrix} \sin \phi \\ \cos \phi \end{bmatrix} = \begin{bmatrix} E_{i,j,1}^{n+1} \\ E_{i,j,0}^n \end{bmatrix} \quad (4.27)$$

The solution for this system of simultaneous equations is

$$\begin{bmatrix} \sin \phi \\ \cos \phi \end{bmatrix} = \frac{-1}{\sin(\kappa_{z0}\Delta x + \omega\Delta t)} \begin{bmatrix} -\sin \omega\Delta t & -\sin \kappa_{z0}\Delta x \\ -\cos \omega\Delta t & \cos \kappa_{z0}\Delta x \end{bmatrix} \begin{bmatrix} E_{i,j,1}^{n+1} \\ E_{i,j,0}^n \end{bmatrix} \quad (4.28)$$

Since $E_{i,j,0}^{n+1} = \sin\phi$, a boundary condition can be written as

$$D_{1_{\text{bar}1}}[E] = (I - \alpha K - \beta Z^{-1})E = 0 \quad (4.29)$$

or

$$E_{i,j,0}^{n+1} = \frac{\sin \omega\Delta t}{\sin(\kappa_{z0}\Delta x + \omega\Delta t)} E_{i,j,1}^{n+1} + \frac{\sin \kappa_{z0}\Delta x}{\sin(\kappa_{z0}\Delta x + \omega\Delta t)} E_{i,j,0}^n \quad (4.30)$$

where the boundary node value is written as a linear combination of only two field values. However, a problem arises with this boundary equation as the coefficients do not sum up exactly to 1. To alleviate this problem, the small angle approximation for sine is used. Keeping only the first order term, the following boundary condition results:

$$D_{1_{\text{bar}1}}[E] \Rightarrow E_{i,j,0}^{n+1} = \frac{\omega\Delta t}{\kappa_{z0}\Delta x + \omega\Delta t} E_{i,j,1}^{n+1} + \frac{\kappa_{z0}\Delta x}{\kappa_{z0}\Delta x + \omega\Delta t} E_{i,j,0}^n \quad (4.31)$$

and the coefficients sum up exactly to 1.

Using this concept, the boundary node value $E_{i,j,0}^{n+1}$ is not restricted to be a linear combination of any two specified field values. For instance, instead of $E_{i,j,1}^{n+1}$ and $E_{i,j,0}^n$, $E_{i,j,1}^{n+1}$ and $E_{i,j,1}^n$ can be used, and a different boundary condition can be derived:

$$D_{1_{\text{bar}2}}[E] \Rightarrow E_{i,j,0}^{n+1} = -\frac{\kappa_{z0}\Delta x - \omega\Delta t}{\omega\Delta t} E_{i,j,1}^{n+1} + \frac{\kappa_{z0}\Delta x}{\omega\Delta t} E_{i,j,1}^n \quad (4.32)$$

Moreover, this concept is not only limited to two field values. More node values can be used, although only two free parameters are allowed. For example, using the field values of the nodes $E_{i,j,1}^{n+1}$, $E_{i,j,1}^n$, and $E_{i,j,0}^n$, the following system of equations can be obtained

$$\begin{bmatrix} \cos(\kappa_{z0}\Delta x - \omega\Delta t) & \sin(\kappa_{z0}\Delta x - \omega\Delta t) \\ \cos\kappa_{z0}\Delta x - \cos\omega\Delta t & \sin\kappa_{z0}\Delta x + \sin\omega\Delta t \end{bmatrix} \begin{bmatrix} \sin\phi \\ \cos\phi \end{bmatrix} = \begin{bmatrix} E_{i,j,1}^n \\ E_{i,j,1}^{n+1} - E_{i,j,0}^n \end{bmatrix} \quad (4.33)$$

and the corresponding boundary condition is

$$D_{1_{\text{bar}3}}[E] \Rightarrow E_{i,j,0}^{n+1} = E_{i,j,1}^n + \frac{\omega\Delta t - \kappa_{z0}\Delta x}{\omega\Delta t + \kappa_{z0}\Delta x} [E_{i,j,1}^{n+1} - E_{i,j,0}^n] \quad (4.34)$$

The above boundary condition is identical with Higdon's first order boundary condition with center differencing shown in equation (4.23).

The boundary conditions given in equations (4.31) and (4.32) are only first order. To obtain higher order boundary conditions, different discrete boundary operators can be multiplied together similar to Higdon's approach. For example, twice multiplying the discrete boundary operator in equation (4.31) results in the following second order boundary condition:

$$D_{2_{\text{bar}11}}[E] \Rightarrow E_{i,j,0}^{n+1} = [(\alpha_1 + \alpha_2)K - \alpha_1\alpha_2K^2 + (\beta_1 + \beta_2)Z^{-1} - (\alpha_1\beta_2 + \alpha_2\beta_1)KZ^{-1} - \beta_1\beta_2Z^{-2}] E_{i,j,0}^{n+1} \quad (4.35)$$

where $\alpha_i = \omega\Delta t / (\kappa_{z0_i}\Delta x + \omega\Delta t)$ and $\beta_i = \kappa_{z0_i}\Delta x / (\kappa_{z0_i}\Delta x + \omega\Delta t)$. The same procedure can be applied to the discrete boundary operator of equation (4.32) to obtain higher order boundary conditions, or alternatively, the operators of equations (4.31) and (4.32) can be cross-multiplied. For instance, $D_{2_{\text{bar}22}}[E]$ is

$$D_{2_{\text{bar}22}} [E] \Rightarrow E_{i,j,0}^{n+1} = [-(\alpha_1 + \alpha_2) K - \alpha_1 \alpha_2 K^2 + (\beta_1 + \beta_2) KZ^{-1} + (\alpha_1 \beta_2 + \alpha_2 \beta_1) K^2 Z^{-1} - \beta_1 \beta_2 K^2 Z^{-2}] E_{i,j,0}^{n+1} \quad (4.36)$$

where $\alpha_1 = (\kappa_{z0_1} \Delta x - \omega \Delta t) / \omega \Delta t$ and $\beta_1 = \kappa_{z0_1} \Delta x / \omega \Delta t$. Cross-multiplying $D_{1_{\text{bar}1}}$ and $D_{1_{\text{bar}2}}$ results in

$$D_{2_{\text{bar}12}} [E] \Rightarrow E_{i,j,0}^{n+1} = [(\alpha_1 - \alpha_2) K + \alpha_1 \alpha_2 K^2 + \beta_1 Z^{-1} + (\beta_1 \alpha_2 + \beta_2) KZ^{-1} - \alpha_1 \beta_2 K^2 Z^{-1} - \beta_1 \beta_2 KZ^{-2}] E_{i,j,0}^{n+1} \quad (4.37)$$

where $\alpha_1 = \omega \Delta t / (\kappa_{z0_1} \Delta x + \omega \Delta t)$, $\beta_1 = \kappa_{z0_1} \Delta x / (\kappa_{z0_1} \Delta x + \omega \Delta t)$, $\alpha_2 = (\kappa_{z0_2} \Delta x - \omega \Delta t) / \omega \Delta t$, and $\beta_2 = \kappa_{z0_2} \Delta x / \omega \Delta t$.

The advantage of representing the boundary value as a linear combination of two field values is the decreased amount of computation resource needed. For a first order boundary condition, only two multiplications and one addition are needed for $D_{1_{\text{bar}}}$ [E] whereas three multiplications and two additions are needed for the operator $D_{1_{\text{higdon}}}$ [E]. The difference in computation operations increases as the order of the boundary condition increases. For a second order boundary condition, $D_{2_{\text{higdon}}}$ [E] requires eight multiplications and seven additions, $D_{2_{\text{bar}12}}$ [E] requires six multiplications and five additions, whereas $D_{2_{\text{bar}11}}$ [E] and $D_{2_{\text{bar}22}}$ [E] require only five multiplications and four additions.

The harmonic boundary operator discussed above is derived based on the assumption that the electromagnetic field varies in a harmonic fashion. However, its use is not limited to time-harmonic problems with monochromatic excitation. Indeed, the harmonic boundary operators (just as Mur's and Higdon's boundary operators) are applicable to problems in which the speed of wave propagation is constant with respect to the wave number, i.e., the medium is non-dispersive. This is because the boundary operators in equations (4.31), (4.32) and (4.34) depend not on the individual values of the angular frequency ω and the wave number κ , but on the ratio between them. Since any propagating waveform in an isotropic medium can be decomposed into a superposition of waves with different wave numbers travelling at the same speed c , the harmonic boundary operators actually apply to electromagnetic wave propagation in non-dispersive media in general. Thus, the

harmonic operators can be used in steady-state as well as transient field calculations under monochromatic or polychromatic excitation.

4.5 Boundary Conditions Comparison

In this section, the different boundary conditions described in the previous sections are compared for accuracy: Mur's method, Higdon's method, and the harmonic method. Because Mur's simplification applies only for two-dimensional structures, the comparison is performed for two-dimensional structures only. For three-dimensional applications, Higdon's method and the harmonic method are superior to Mur's method in terms of efficiency because of the one-dimensional spatial stencil utilized. Assuming that the wave travels in the $-z$ -direction, the discretized equations for the different boundary conditions are listed as follows:

For Mur's method, $D_{2_{\text{mur}}}$ [E, H] gives

$$E_{i,j,0}^{n+1} = E_{i,j,1}^n - \left(\frac{c\Delta t - n\Delta x}{c\Delta t + n\Delta x} \right) E_{i,j,0}^n + \frac{\mu c^2 \Delta t}{2n(c\Delta t + n\Delta x)} \left[H_{z,j+1/2,1}^{n+\frac{1}{2}} - H_{z,j-1/2,1}^{n+\frac{1}{2}} + H_{z,j+1/2,0}^{n+\frac{1}{2}} - H_{z,j-1/2,0}^{n+\frac{1}{2}} \right] + \left(\frac{c\Delta t - n\Delta x}{c\Delta t + n\Delta x} \right) E_{i,j,1}^{n+1} \quad (4.38)$$

For Higdon's method, $D_{2_{\text{higdon}}}$ [E] gives

$$E_{i,j,0}^{n+1} = [-(\alpha_1 + \alpha_2)K - \alpha_1\alpha_2K^2 + (\beta_1 + \beta_2)Z^{-1} + (\gamma_1 + \gamma_2 + \alpha_1\beta_2 + \alpha_2\beta_1)KZ^{-1} + (\alpha_1\gamma_2 + \alpha_2\gamma_1)K^2Z^{-1} - \beta_1\beta_2Z^{-2} - (\beta_1\gamma_2 + \beta_2\gamma_1)KZ^{-2} - \gamma_1\gamma_2K^2Z^{-2}] E_{i,j,0}^{n+1} \quad (4.39)$$

where

$$\alpha_i = \frac{a_i \kappa \cos \theta_{0i} \Delta x - (1 - b_i) \omega \Delta t}{(1 - a_i) \kappa \cos \theta_{0i} \Delta x + (1 - b_i) \omega \Delta t}, \quad \beta_i = \frac{(1 - a_i) \kappa \cos \theta_{0i} \Delta x - b_i \omega \Delta t}{(1 - a_i) \kappa \cos \theta_{0i} \Delta x + (1 - b_i) \omega \Delta t}, \quad \text{and} \\ \gamma_i = \frac{a_i \kappa \cos \theta_{0i} \Delta x + b_i \omega \Delta t}{(1 - a_i) \kappa \cos \theta_{0i} \Delta x + (1 - b_i) \omega \Delta t} \quad (4.40)$$

For the harmonic method, $D_{2_{\text{har11}}}$ [E] gives

$$E_{i,j,0}^{n+1} = [(\alpha_1 + \alpha_2)K - \alpha_1\alpha_2K^2 + (\beta_1 + \beta_2)Z^{-1} - (\alpha_1\beta_2 + \alpha_2\beta_1)KZ^{-1} - \beta_1\beta_2Z^{-2}] E_{i,j,0}^{n+1} \quad (4.41)$$

where $\alpha_i = \omega\Delta t / (\kappa_{z0_i}\Delta x + \omega\Delta t)$ and $\beta_i = \kappa_{z0_i}\Delta x / (\kappa_{z0_i}\Delta x + \omega\Delta t)$. With $D_{2_{\text{nar}22}}[E]$, the boundary condition becomes

$$E_{i,j,0}^{n+1} = [-(\alpha_1 + \alpha_2)K - \alpha_1\alpha_2K^2 + (\beta_1 + \beta_2)KZ^{-1} + (\alpha_1\beta_2 + \alpha_2\beta_1)K^2Z^{-1} - \beta_1\beta_2K^2Z^{-2}] E_{i,j,0}^{n+1} \quad (4.42)$$

where $\alpha_i = (k_{z0_i}\Delta x - \omega\Delta t) / \omega\Delta t$ and $\beta_i = k_{z0_i}\Delta x / \omega\Delta t$. Cross-multiplication of the two first order boundary conditions gives

$$E_{i,j,0}^{n+1} = [(\alpha_1 - \alpha_2)K + \alpha_1\alpha_2K^2 + \beta_1Z^{-1} + (\beta_1\alpha_2 + \beta_2)KZ^{-1} - \alpha_1\beta_2K^2Z^{-1} - \beta_1\beta_2KZ^{-2}] E_{i,j,0}^{n+1} \quad (4.43)$$

where the coefficients α_i and β_i are given in the previous section.

These five different boundary conditions are applied to four different structures and their properties such as accuracy and convergence are compared. The four different structures are shown in Figure 4.2. The first structure is a 1 μm by 1 μm empty (vacuum) simulation domain at $\lambda=0.5$

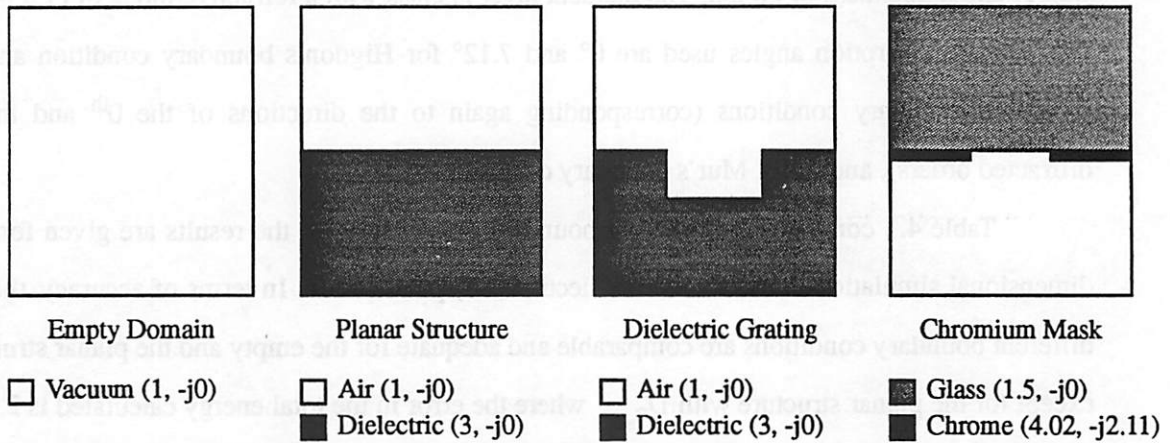


Figure 4.2 Four different structures used to assess the properties of the different absorbing boundary conditions. The first structure is an empty domain (left), the second structure consists of two semi-infinite materials with a planar interface (middle left), the third structure is a dielectric grating which can be highly resonant (middle right), and the fourth is a chromium mask (right), a structure typical in photolithographic applications.

μm . Thus, the boundary conditions are expected to give no reflection (0%) and all the energy should be transmitted (100%). The second structure contains two semi-infinite lossless materials. The simulation domain is again $1\mu\text{m}$ by $1\mu\text{m}$ with the incident wavelength at $0.5\mu\text{m}$. Electromagnetic energy is incident from air (vacuum) with a refractive index of 1. A dielectric material with a refractive index of 3 has a planar interface with air. The (electric field) reflection coefficient is -0.5; and thus the reflected energy should be 25% whereas the transmitted energy should be 75%. The third structure is a non-planar dielectric grating. The grating has a $1.0\mu\text{m}$ period and a duty cycle of 1.0. The height of the grating is $0.2\mu\text{m}$ and the edges are vertical. The perfect absorption angles used are 0° and 30° for Higdon's boundary condition and the harmonic boundary conditions (corresponding to the directions of the 0^{th} and 1^{st} diffracted orders). With an incident wavelength of $0.5\mu\text{m}$, such a structure may reflect a large portion of the incident light wave energy in the non-specular directions and may pose accuracy problems for the numerical boundary conditions. The fourth structure is a chromium mask opening. This is a typical geometry encountered in photolithography. The incident wavelength is $0.248\mu\text{m}$. The mask opening space has a width of $0.25\mu\text{m}$ ($\sim 1\lambda$) with a period of $2.0\mu\text{m}$. The opaque chromium layer has a refractive index of $(4.02, -j2.11)$ and a thickness of 80 nm . The incident layer is glass with a refractive index of $(1.5, -j0.0)$. The perfect absorption angles used are 0° and 7.12° for Higdon's boundary condition and the harmonic boundary conditions (corresponding again to the directions of the 0^{th} and the 1^{st} diffracted orders), and 0° for Mur's boundary condition.

Table 4.1 compares the different boundary conditions. All the results are given for two-dimensional simulation in the transverse electric (TE) polarization. In terms of accuracy, the five different boundary conditions are comparable and adequate for the empty and the planar structure, except for the planar structure with $D_{2_{\text{har}11}}$ where the error in the total energy calculated is 2.57%. For the dielectric grating and the chromium mask structure, however, Higdon's boundary condition gives slightly different results for both the reflected and the transmitted energy. Investigation of the electric field amplitude confirms the difference among the different boundary conditions. Figure 4.3 shows the electric field amplitude (for the chrome mask structure) both along a vertical line through the middle of the opening and a horizontal line just underneath the chromium layer. There is virtually no difference in the electric field amplitude along the horizontal line underneath the

Empty Structure

Boundary Condition	Reflected Energy (%)	Transmitted Energy (%)	Total Energy (%)	Convergence (cycles)	CPU Time (s)
Mur	0.00	100.22	100.22	7	56.39
Higdon	0.00	100.52	100.52	7	76.74
Harmonic ₁₁ eq. (4.41)	0.00	100.27	100.27	7	61.30
Harmonic ₂₂ eq. (4.42)	0.00	100.94	100.94	7	69.29
Harmonic ₁₂ eq. (4.43)	0.00	100.31	100.31	7	69.47

Planar Structure

Boundary Condition	Reflected Energy (%)	Transmitted Energy (%)	Total Energy (%)	Convergence (cycles)	CPU Time (s)
Mur	24.92	76.24	101.16	11	77.55
Higdon	25.11	101.04	100.52	11	106.88
Harmonic ₁₁ eq. (4.41)	24.75	77.82	102.57	12	90.21
Harmonic ₂₂ eq. (4.42)	25.20	75.43	100.63	11	96.06
Harmonic ₁₂ eq. (4.43)	25.73	74.32	100.05	11	96.34

Dielectric Grating

Boundary Condition	Reflected Energy (%)	Transmitted Energy (%)	Total Energy (%)	Convergence (cycles)	CPU Time (s)
Mur	22.07	77.80	99.87	17	108.27
Higdon	19.82	74.63	94.45	35	283.41
Harmonic ₁₁ eq. (4.41)	22.27	77.61	99.88	37	231.13
Harmonic ₂₂ eq. (4.42)	22.28	76.59	98.87	13	108.65
Harmonic ₁₂ eq. (4.43)	22.59	76.38	98.97	17	135.72

Chrome Mask

Boundary Condition	Reflected Energy (%)	Transmitted Energy (%)	Total Energy (%)	Convergence (cycles)	CPU Time (s)
Mur	28.64	9.29	37.93	13	309.48
Higdon	28.63	8.69	37.32	20	578.59
Harmonic ₁₁ eq. (4.41)	29.16	9.36	38.52	16	389.64
Harmonic ₂₂ eq. (4.42)	28.69	9.27	37.96	13	362.63
Harmonic ₁₂ eq. (4.43)	28.83	9.26	38.09	13	372.31

Table 4.1 Comparison of the different boundary conditions for two-dimensional simulations. All the boundary conditions give similar energy calculations. For the empty and planar structures, there is virtually no difference in convergence. For the chromium mask structure, however, Higdon's method shows the worst convergence property.

chromium layer, except that Higdon's boundary condition gives a slightly higher amplitude at the

center of the opening. For the vertical line along the opening, a larger discrepancy is seen. Mur's boundary condition and all of the harmonic conditions in equations (4.41), (4.42) and (4.43) agree well. However, the difference in electric field amplitude between Higdon's method and the other methods can be as large as 5% at particular spatial locations, although the locations of the standing wave peaks and valleys are the same for all the boundary conditions.

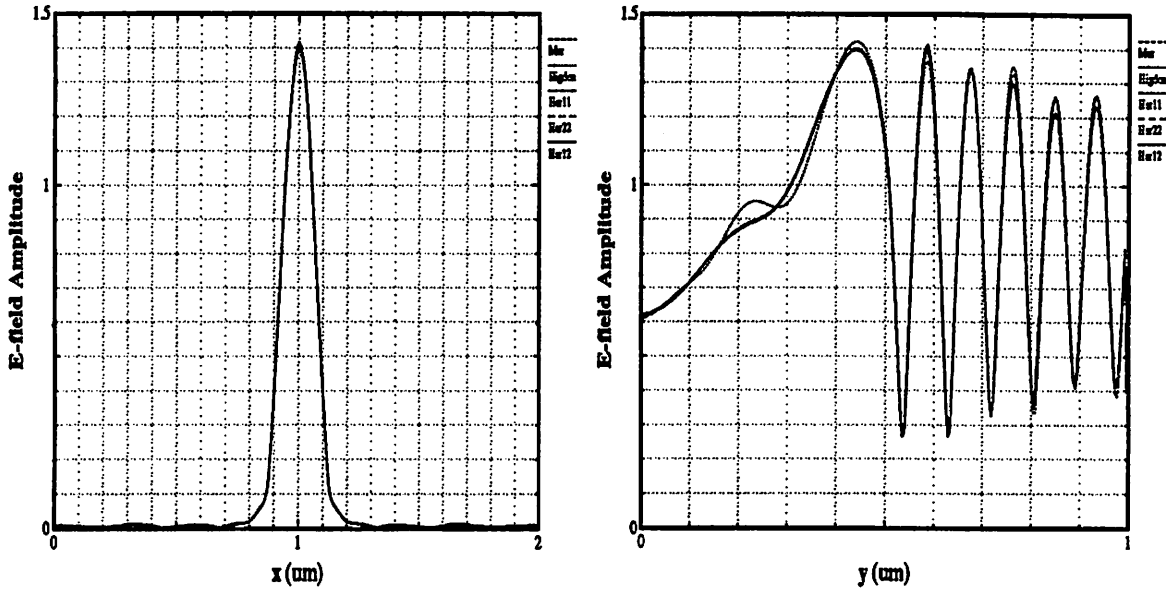


Figure 4.3 Electric field amplitude of the chromium mask structure calculated by the different boundary conditions. The field amplitude shows virtually no difference at a horizontal line just underneath the chromium layer (left). For a vertical line along the opening (right), however, Higdon's boundary condition shows slight discrepancy when compared with the other boundary conditions. Nevertheless, the location of the standing wave peaks and valleys are the same for all the different boundary conditions

The efficiency of the boundary conditions are also evaluated in Table 4.1. There are two criteria: the amount of computer time used and the number of wave cycles for convergence. The criterion for convergence is that the electric field varies by less than 1% for three consecutive periods at the same instant of the wave cycle. While the amount of computer time is the most important quality for an efficient boundary condition, the number of wave cycles for convergence is a good indicator of whether the boundary condition absorbs the waves well. In general, a large number of wave cycles for convergence means that either the structure under examination is highly resonant or the waves are artificially reflecting off the simulation domain boundaries. Therefore,

comparing the number of wave cycles for convergence required for the different boundary conditions for the same structure gives an indication of the absorbing quality of the boundary conditions. Table 4.1 indicates that for two-dimensional simulations, Mur's boundary condition is the most efficient, both in terms of the computation time and the number of wave cycles for convergence. The harmonic boundary conditions in equations (4.42) and (4.43) are comparable to Mur's boundary condition in terms of number of cycles for convergence, but the computation time of the two harmonic boundary conditions are slightly higher than that of Mur's boundary condition. Higdon's boundary condition seems to be the worst among all the boundary conditions as it requires the most amount of computer time as well as wave cycles for convergence.

The above accuracy comparison demonstrated that the boundary conditions are suitable for implementation. Choice of the boundary condition to use thus depends on the efficiency. The previous efficiency discussion suggests that Mur's boundary condition is the best for two-dimensional calculations as it requires the lowest amount of computer time. For three-dimensional calculations, however, Mur's boundary condition no longer has the advantage over the other boundary conditions as its stencil becomes large. To estimate the efficiency of the boundary conditions for three-dimensional structures, first note that the computer time consumed by the boundary conditions is about 75% of the total simulation time²⁵. Table 4.1 thus implies that the harmonic boundary conditions are slower than Mur's boundary condition by about 20%. Counting the number of additions and multiplications, Mur's boundary condition needs three multiplications and six additions (a total of 9 floating point operations) whereas the harmonic boundary condition $D_{2_{\text{har}12}}$ requires six multiplications and five additions (a total of 11 floating point operations). The ratio of the number of floating point operations is 1.22, agreeing with the 20% increase in computer time for the harmonic boundary condition. For three-dimensional calculations, the number of floating point operations is 75 (41 additions and 34 multiplications) for Mur's boundary condition and 11 (6 multiplications and 5 additions) for the harmonic boundary condition H_{12} . The advantage in the efficiency of the harmonic boundary condition is thus estimated to be almost 600%.

4.6 Conclusions

In this chapter, different boundary conditions resulting from the discretization of continuous differential operators are presented. In particular, the methods proposed by Mur and Higdon are compared with novel boundary conditions derived based on the space- and time-harmonic variation of the field. All these boundary conditions are shown to produce reasonable results; they also agree well with one another except for Higdon's boundary condition. In terms of efficiency, Higdon's method and the harmonic method are more efficient than Mur's method for three-dimensional applications. This is because Mur's method requires a three-dimensional spatial stencil whereas Higdon's method as well as the harmonic method require only a one-dimensional spatial stencil. The harmonic method is slightly more efficient than Higdon's method as it requires fewer number of multiplications and additions. In terms of accuracy, Mur's boundary condition and the harmonic boundary condition are superior to Higdon's method. Based on these considerations, the harmonic boundary condition $D_{2_{\text{har}12}}$ in equation (4.43) is chosen for three-dimensional implementation as it is expected to converge (in terms of the number of wave cycles) as fast as Mur's boundary condition and requires about one seventh of the computer time of Mur's boundary condition.

Chapter 5

Modeling Dispersive Materials

5.1 Introduction

Electromagnetic simulation using the TDFD approach has received increasing attention in recent years because of its applicability for execution on massively parallel computer architectures. However, difficulty arises when the TDFD approach is applied in problems involving dispersive materials. The original TDFD formulation by Yee¹⁰⁴ requires that the electric permittivity, magnetic permeability, and conductivity of all the materials in the structure be frequency independent. Nevertheless, this assumption of frequency independent material constants alone does not place a constraint on applications where the only interest is the response of a structure at a particular frequency, since the uniqueness theorem⁸⁰ states that any converged solution is the true solution. The problem of the TDFD approach arises when a material has the property that the magnitude of the imaginary part of the refractive index is larger than the real part. This causes the real part of the permittivity of the material to be less than zero, and the TDFD formulation becomes unstable as shown in Chapter 3.

Different schemes have been proposed to solve this instability problem. A possible scheme is the complex field method in which the field variables as well as the material constants are expressed as complex numbers. This approach can be viewed as solving for two separate problems, with a 90° phase difference between them. Another approach is proposed by Luebbers et al.⁴⁸ in which the convolution relation between the electric field and the electric displacement is calculated at each time step by a recursion relation. This approach is called the frequency-dependent finite-difference time-domain ((FD)²TD) method in this chapter. Lee et al.⁴¹ proposed a scheme in which the electric displacement (magnetic induction) is first found from Ampere's law (Faraday's law), and then the electric field (magnetic field) is derived from the electric displacement (magnetic induction). This method, which is called the four-step method in this chapter, requires no explicit calculation of the convolution integral. In this chapter, these different schemes are assessed for their

applicability and efficiency. While only electric dispersive materials are considered, extension to modeling magnetic dispersive materials is straightforward.

5.2 The Complex Field Method

In the conventional TDFD approach, the following pair of equations is solved:

$$\nabla \times \vec{H} = \epsilon \frac{\partial \vec{E}}{\partial t} + \sigma \vec{E} \quad (5.1)$$

$$\nabla \times \vec{E} = -\mu \frac{\partial \vec{H}}{\partial t} \quad (5.2)$$

This pair of equations assumes that there is no magnetic loss, and that the electric loss is represented by the conductivity σ . In the complex field method (CFM), each field variable is represented by a complex number instead of a real number in conventional time-domain schemes. The motivation of this formulation comes from frequency-domain approaches in which each field component is represented by an amplitude and a phase (a phasor). The difference in the CFM is that instead of an amplitude and a phase, each field component is represented by a real part and an imaginary part. In this scheme, electric loss is not represented by the conductivity, but by a complex dielectric constant. Hence, the set of equations which the CFM solves is as follows:

$$\nabla \times \underline{\vec{H}} = \epsilon \frac{\partial \underline{\vec{E}}}{\partial t} \quad (5.3)$$

$$\nabla \times \underline{\vec{E}} = -\mu \frac{\partial \underline{\vec{H}}}{\partial t} \quad (5.4)$$

where the underscore indicates a complex quantity. Equations (5.3) and (5.4) are actually four finite difference equations, corresponding to the real and imaginary parts of the electric and magnetic fields, i. e.,

$$\nabla \times \underline{\vec{H}}_r = \epsilon_r \frac{\partial \underline{\vec{E}}_r}{\partial t} - \epsilon_i \frac{\partial \underline{\vec{E}}_i}{\partial t} \quad (5.5)$$

$$\nabla \times \underline{\vec{H}}_i = \epsilon_r \frac{\partial \underline{\vec{E}}_i}{\partial t} + \epsilon_i \frac{\partial \underline{\vec{E}}_r}{\partial t} \quad (5.6)$$

$$\nabla \times \vec{E}_r = -\mu \frac{\partial \vec{H}_r}{\partial t} \quad (5.7)$$

$$\nabla \times \vec{E}_i = -\mu \frac{\partial \vec{H}_i}{\partial t} \quad (5.8)$$

where the subscripts r and i represent the real and imaginary parts respectively.

To justify the use of complex dielectric constants in a time-domain scheme, notice that the conductivity σ can be associated with an imaginary relative permittivity with the imaginary part given by $-\sqrt{-1}(\sigma/\omega)$ for time-harmonic fields. Indeed, the difference between the use of conductivity and the use of a complex permittivity is primarily philosophical²⁶. Therefore, at steady-state, Maxwell's curl equations can be expressed by equations (5.3) and (5.4), with the dielectric constant given by

$$\underline{\epsilon} = \epsilon_r - \sqrt{-1}\epsilon_i = \epsilon - \sqrt{-1}\frac{\sigma}{\omega} \quad (5.9)$$

The advantages of the CFM is its simplicity. There is no major modification of the finite-difference equations. However, this scheme requires more field variables (more memory) and more computation per iteration (more CPU time). Moreover, the CFM does not model dispersive behavior of materials since it assumes that the complex dielectric constant $\underline{\epsilon}$ is independent of frequency. However, this latter limitation does not place severe restrictions on applications in photolithography since most sources can be assumed to be monochromatic.

The CFM, although simple and straightforward in implementation, is unstable except for lossless materials. In order to examine the stability of the CFM, consider the two-dimensional finite-difference equations in the TE polarization:

$$\begin{aligned} E_z^{n+1}(i, j) = & \frac{\Delta t}{\underline{\epsilon}\Delta x} \left[H_x^{n+\frac{1}{2}}(i, j - \frac{1}{2}) - H_x^{n+\frac{1}{2}}(i, j + \frac{1}{2}) + H_y^{n+\frac{1}{2}}(i + \frac{1}{2}, j) - H_y^{n+\frac{1}{2}}(i - \frac{1}{2}, j) \right] \\ & + E_z^n(i, j) \end{aligned} \quad (5.10)$$

$$H_y^{n+\frac{1}{2}}(i + \frac{1}{2}, j) = H_y^{n-\frac{1}{2}}(i + \frac{1}{2}, j) + \frac{\Delta t}{\mu\Delta x} [E_z^n(i + 1, j) - E_z^n(i, j)] \quad (5.11)$$

$$H_x^{n+\frac{1}{2}}(i, j - \frac{1}{2}) = H_x^{n-\frac{1}{2}}(i, j - \frac{1}{2}) + \frac{\Delta t}{\mu\Delta x} [E_z^n(i, j - 1) - E_z^n(i, j)] \quad (5.12)$$

In order to use Fourier analysis as was done in Chapter 3, equation (5.10) must first be modified by substituting equations (5.11) and (5.12) for $H_x^{n+1/2}$ and $H_y^{n+1/2}$. The scheme thus becomes

$$\begin{aligned} E_z^{n+1}(i, j) = & \alpha \left[H_x^{n-\frac{1}{2}}(i, j - \frac{1}{2}) - H_x^{n-\frac{1}{2}}(i, j + \frac{1}{2}) + H_y^{n-\frac{1}{2}}(i + \frac{1}{2}, j) - H_y^{n-\frac{1}{2}}(i - \frac{1}{2}, j) \right] + \\ & \alpha\beta [E_z^n(i+1, j) - 2E_z^n(i, j) + E_z^n(i-1, j) + E_z^n(i, j+1) - 2E_z^n(i, j) + E_z^n(i, j-1)] + \\ & E_z^n(i, j) \end{aligned} \quad (5.13)$$

where $\alpha = \Delta t / (\epsilon \Delta x)$ and $\beta = \Delta t / (\mu \Delta x)$. The Fourier transform of the finite-difference equations (equations (5.10) to (5.12)) can thus be expressed as

$$\hat{F}^{n+1} = A(\theta_1, \theta_2) \hat{F}^n \quad (5.14)$$

where $\hat{F}^n = (\hat{E}_z^n, \hat{H}_x^n, \hat{H}_y^n)^T$ and

$$A(\theta_1, \theta_2) = \begin{bmatrix} 1 - 4\alpha\beta((\sin^2\theta_1/2) + (\sin^2\theta_2/2)) & i2\alpha\sin\theta_2/2 & -i2\alpha\sin\theta_1/2 \\ i2\beta\sin\theta_2/2 & 1 & 0 \\ -i2\beta\sin\theta_1/2 & 0 & 1 \end{bmatrix} \quad (5.15)$$

The characteristic equation for the matrix A is

$$(\lambda - 1) [\lambda^2 + 2\lambda(2\alpha\beta(\sin^2\theta_1/2 + \sin^2\theta_2/2) - 1) + 1] = 0 \quad (5.16)$$

The eigenvalues are $\lambda_1 = 1$ and

$$\lambda_{2,3} = 1 - 2\alpha\beta(\sin^2\theta_1/2 + \sin^2\theta_2/2) \left[1 \mp \sqrt{1 - (1/\alpha\beta)(\sin^2\theta_1/2 + \sin^2\theta_2/2)} \right] \quad (5.17)$$

The magnitudes of λ_2 and λ_3 are greater than or equal to 1, with equality holding only when $\epsilon_i = 0$. Therefore, the TDFD numerical scheme using the CFM is stable only if the materials are lossless, and is thus not practical.

5.3 The Four-step Method

In the conventional TDFD approach, the following pair of equations is solved:

$$\nabla \times \vec{H} = \epsilon \frac{\partial \vec{E}}{\partial t} + \sigma \vec{E} \quad (5.18)$$

$$\nabla \times \vec{E} = -\mu \frac{\partial \vec{H}}{\partial t} \quad (5.19)$$

where the permittivity ϵ , permeability μ , and conductivity σ are assumed to be constants. This leap-frog algorithm consists of two major steps. In the first step, the magnetic field values in the previous time step are used to update the electric field. In the second step, these newly updated electric field values are used to update the magnetic field. In the four-step approach developed by Lee et al.⁴¹, two extra steps are added in which the following set of equations is solved:

$$\nabla \times \vec{H} = \frac{\partial \vec{D}}{\partial t} \quad (5.20)$$

$$\vec{D}(\omega) = \epsilon(\omega) \vec{E}(\omega) \quad (5.21)$$

$$\nabla \times \vec{E} = -\frac{\partial \vec{B}}{\partial t} \quad (5.22)$$

$$\vec{B}(\omega) = \mu(\omega) \vec{H}(\omega) \quad (5.23)$$

Equations (5.20) and (5.22) are essentially the conventional equations except that the electric displacement D replaces ϵE and the magnetic induction B replaces μH . Equations (5.21) and (5.23) are additional equations which model the dispersive nature of the material. Note that equations (5.21) and (5.23) are frequency-domain equations. To obtain their time-domain counterparts, one must model the frequency dependence of the permittivity and permeability as well as make the appropriate connections from the frequency-domain expressions to the time-domain expressions. For example, consider the electric dispersion relation of equation (5.21), the tasks become finding a suitable mathematical model for the electric permittivity and transforming the frequency-domain relation of equation (5.21) into a corresponding time-domain equation.

The dispersive behavior of a material may be characterized by many complex physical phenomena. For the application in hand in which the interest is only in a narrow band of frequencies, the mathematical model of the permittivity should satisfy two constraints only. Besides matching the characteristics of the material within the interested frequency range, the

causality condition must be obeyed. Two possible mathematical models are the Debye model¹² and the Lorentz model¹¹, shown in the following equations respectively:

$$\epsilon_{\text{Debye}}(\omega) = \epsilon_{\infty} + \frac{\epsilon_s - \epsilon_{\infty}}{1 - \sqrt{-1}(\omega/\omega_0)} \quad (5.24)$$

$$\epsilon_{\text{Lorentz}}(\omega) = 1 + \frac{\omega_p^2}{\omega_s^2 - \omega^2 - \sqrt{-1}(\omega/\omega_0)} \quad (5.25)$$

In equation (5.24), ϵ_s is the permittivity of the material at zero frequency, ϵ_{∞} is the permittivity when $\omega \rightarrow \infty$, and ω_0 is the resonance frequency. The parameter ω_p in the Lorentz model of equation (5.25) is the “plasma” frequency, ω_s and $1/\omega_0$ are respectively the resonance frequency and the damping constant. Equations (5.24) and (5.25) are frequency-domain equations which can be transformed into time-domain equations by making the substitution

$$\frac{\partial}{\partial t} = -\sqrt{-1}\omega \quad (5.26)$$

Hence, for the Debye model, the frequency domain relation in equation (5.21) is transformed via equation (5.26) into the following time-domain equation

$$\left(1 + \frac{1}{\omega_0} \frac{\partial}{\partial t}\right) D(t) = \epsilon_0 \left(\epsilon_s + \frac{\epsilon_{\infty}}{\omega_0} \frac{\partial}{\partial t}\right) E(t) \quad (5.27)$$

Similarly, the time-domain equation for the Lorentz model is

$$\left(\omega_s^2 + \frac{\partial^2}{\partial t^2} + \frac{1}{\omega_0} \frac{\partial}{\partial t}\right) D(t) = \epsilon_0 \left(\omega_p^2 + \omega_s^2 + \frac{\partial^2}{\partial t^2} + \frac{1}{\omega_0} \frac{\partial}{\partial t}\right) E(t) \quad (5.28)$$

With equations (5.27) and (5.28), the discretized time-domain counterpart of equation (5.21) for the Debye and Lorentz models are as follows, respectively:

$$E^{n+1} = \frac{1}{\frac{\epsilon_{\infty}}{\omega_0 \Delta t} + \frac{\epsilon_s}{2}} \left(\left(\frac{1}{\omega_0 \Delta t} + \frac{1}{2}\right) \frac{D^{n+1}}{\epsilon_0} + \left(\frac{1}{2} - \frac{1}{\omega_0 \Delta t}\right) \frac{D^n}{\epsilon_0} + \left(\frac{\epsilon_{\infty}}{\omega_0 \Delta t} - \frac{\epsilon_s}{2}\right) E^n \right) \quad (5.29)$$

$$E^{n+1} = \frac{D^{n+1}}{\epsilon_0} + \frac{\omega_s^2 \Delta t^2 - 2}{1 + \Delta t/2\omega_0} \left(\frac{D^n}{\epsilon_0} - E^n\right) - \frac{\omega_p^2 \Delta t^2}{1 + \Delta t/2\omega_0} E^n + \frac{1 - \Delta t/2\omega_0}{1 + \Delta t/2\omega_0} \left(\frac{D^{n-1}}{\epsilon_0} - E^{n-1}\right) \quad (5.30)$$

where the superscript n stands for the n^{th} time step. With equation (5.29) or (5.30) relating the electric field E to the electric displacement D , the four-step algorithm is complete. Firstly, the electric displacement is found from values of the magnetic field at the previous time step. Secondly, the electric field is found from the electric displacement with either equation (5.29) or (5.30), depending on the mathematical model used. The third and fourth steps update the magnetic induction and the magnetic field similar to the first and second steps. For two-dimensional simulations of electric dispersive problems in the TE polarization with the Lorentz model, the set of updating equations (corresponding to equations (5.20), (5.21), (5.22), and (5.23)) becomes

$$D_z^{n+1}(i, j) = D_z^n(i, j) + \frac{\Delta t}{\Delta x} \left(H_x^{n+\frac{1}{2}}(i, j - \frac{1}{2}) - H_x^{n+\frac{1}{2}}(i, j + \frac{1}{2}) + H_y^{n+\frac{1}{2}}(i + \frac{1}{2}, j) - H_y^{n+\frac{1}{2}}(i - \frac{1}{2}, j) \right) \quad (5.31)$$

$$E_z^{n+1}(i, j) = \frac{D_z^{n+1}(i, j)}{\epsilon_0} + \frac{\omega_s^2 \Delta t^2 - 2}{1 + \Delta t/2\omega_0} \left(\frac{D_z^n(i, j)}{\epsilon_0} - E_z^n(i, j) \right) - \frac{\omega_p^2 \Delta t^2}{1 + \Delta t/2\omega_0} E_z^n(i, j) + \frac{1 - \Delta t/2\omega_0}{1 + \Delta t/2\omega_0} \left(\frac{D_z^{n-1}(i, j)}{\epsilon_0} - E_z^{n-1}(i, j) \right) \quad (5.32)$$

$$H_x^{n+\frac{1}{2}}(i, j - \frac{1}{2}) = H_x^{n-\frac{1}{2}}(i, j - \frac{1}{2}) + \frac{\Delta t}{\mu \Delta x} (E_z^n(i, j - 1) - E_z^n(i, j)) \quad (5.33)$$

$$H_y^{n+\frac{1}{2}}(i + \frac{1}{2}, j) = H_y^{n-\frac{1}{2}}(i + \frac{1}{2}, j) + \frac{\Delta t}{\mu \Delta x} (E_z^n(i + 1, j) - E_z^n(i, j)) \quad (5.34)$$

This method has been applied in the study of several topographies. In the problem of half space filled with water⁴⁸, this method was found to give numerical results which are in excellent agreement with theoretically calculated results⁴¹. For the problem of a two-dimensional cylindrical dispersive scatterer⁴¹, it was found to give good agreement with the results calculated using the eigenfunction expansion approach¹⁰. These numerical results have demonstrated and confirmed the validity and accuracy of the four-step approach.

5.4 The Frequency-dependent Finite-difference Time-domain Method

The frequency-dependent finite-difference time-domain (FD)²TD method was proposed by Luebbers et al.⁴⁸ to solve problems involving transient propagation in a plasma, but their method is equally applicable in solving photolithography problems involving highly dispersive materials. Their method consists primarily of expressing the electric displacement D as a convolution between the electric field E and the frequency dependent electric susceptibility χ . This approach replaces the need to find the electric displacement D first and then update the electric field using the electric displacement values (in the four-step method) by the calculation of a time integral. In the (FD)²TD method, the electric displacement D is related to the electric field as:

$$D(t) = \epsilon_{\infty} \epsilon_0 E(t) + \epsilon_0 \int_0^t E(t-\tau) \chi(\tau) d\tau \quad (5.35)$$

where ϵ_0 is the permittivity of free space, ϵ_{∞} is the relative permittivity of the material when $\omega \rightarrow \infty$, and χ is the electric susceptibility of the material. Theoretically, ϵ_{∞} equals 1.0 for all materials³², but is left in the equation for the purpose of comparison with the conventional TDFD approach. Assuming that all the field values are constant during each time step and are all zero for $t < 0$, discretization of equation (5.35) results in the following equation:

$$D^{n+1} - D^n = \epsilon_{\infty} \epsilon_0 (E^{n+1} - E^n) + \epsilon_0 E^{n+1} \int_0^{\Delta t} \chi(\tau) d\tau + \epsilon_0 \sum_{m=0}^{n-1} E^{n-m} \left(\int_{(m+1)\Delta t}^{(m+2)\Delta t} \chi(\tau) d\tau - \int_{m\Delta t}^{(m+1)\Delta t} \chi(\tau) d\tau \right) \quad (5.36)$$

Denoting $\chi_m = \int_{m\Delta t}^{(m+1)\Delta t} \chi(\tau) d\tau$ and $\Delta\chi_m = \chi_m - \chi_{m+1}$, the updating equation for the electric field becomes

$$E_z^{n+1}(i, j) = \frac{\Delta t}{\Delta x \epsilon_0 (\epsilon_{\infty} + \chi_0)} (H_y^{n+1/2}(i+1/2, j) - H_y^{n+1/2}(i-1/2, j) + H_x^{n+1/2}(i, j-1/2) - H_x^{n+1/2}(i, j+1/2)) + \frac{\epsilon_{\infty}}{\epsilon_{\infty} + \chi_0} E_z^n(i, j) + \frac{1}{\epsilon_{\infty} + \chi_0} \sum_{m=0}^{n-1} E_z^{n-m}(i, j) \Delta\chi_m \quad (5.37)$$

for a two-dimensional structure in the TE polarization. Equation (5.37) is obtained by discretization of the curl equation of Ampere's Law and substituting equation (5.36) for the temporal electric

displacement difference $(D^{n+1} - D^n)$. Note that for non-dispersive materials, $\epsilon(\omega) = \epsilon = \epsilon_\infty$ and $\chi_0 = \chi_m = 0$, and equation (5.37) reduces to the conventional TDFD equation.

At first glance, calculation of the electric field at the n^{th} time step via equation (5.37) requires storage of a large number of electric field values from previous time steps because of the summation term. However, this is not necessarily the case for a suitable choice of the mathematical model of the permittivity. For instance, for the Debye model of equation (5.24), and for the Lorentz model of equation (5.25) with $\omega_0 = 0$, the summation term in equation (5.37) can be calculated recursively. Therefore, the $(\text{FD})^2\text{TD}$ method requires only one additional storage element. To illustrate, consider the Debye model of the permittivity in equation (5.24). The electric susceptibility is given by

$$\chi_{\text{Debye}}(\omega) = \frac{\epsilon_s - \epsilon_\infty}{1 - \sqrt{-1}(\omega/\omega_0)} \quad (5.38)$$

Fourier transformation of equation (5.38) leads to the time-domain susceptibility function (for $\tau \geq 0$)

$$\chi_{\text{Debye}}(\tau) = (\epsilon_s - \epsilon_\infty) \omega_0 \exp(-\omega_0 \tau) \quad (5.39)$$

With this time-domain susceptibility function, the summation term in equation (5.37) can be written as

$$\Psi_z^n(i, j) = \sum_{m=0}^{n-1} E_z^{n-m}(i, j) \Delta\chi_m = \exp(-\omega_0 \Delta t) \Psi_z^{n-1}(i, j) + \Delta\chi_0 E_z^n(i, j) \quad (5.40)$$

Thus, calculation of the summation term in equation (5.37) can be performed via the recursion expression for Ψ_z in equation (5.40). This requires only one additional storage element (Ψ_z) and can be updated easily. For the Lorentz model of the permittivity in equation (5.25) with $\omega_s = 0$, the time-domain susceptibility function is

$$\chi_{\text{Lorentz}}(\tau) = \frac{\omega_p^2}{\omega_0} (1 - \exp(-\tau\omega_0)) \quad (5.41)$$

In this case, the recursion relation in equation (5.40) still applies, but the expressions for χ_0 and $\Delta\chi_0$ are different. Thus, regardless of the mathematical model used, the updating equations in the $(\text{FD})^2\text{TD}$ method are formally identical. For instance, for two-dimensional simulations in the TE

polarization with only electric dispersive materials, the set of updating equations for the (FD)²TD method is

$$\Psi_z^n(i, j) = \sum_{m=0}^{n-1} E_z^{n-m}(i, j) \Delta\chi_m = \exp(-\omega_0 \Delta t) \Psi_z^{n-1}(i, j) + \Delta\chi_0 E_z^n(i, j) \quad (5.42)$$

$$E_z^{n+1}(i, j) = \frac{\Delta t}{\Delta x \epsilon_0 (\epsilon_\infty + \chi_0)} (H_y^{n+1/2}(i+1/2, j) - H_y^{n+1/2}(i-1/2, j) + H_x^{n+1/2}(i, j-1/2) - H_x^{n+1/2}(i, j+1/2)) + \frac{\epsilon_\infty}{\epsilon_\infty + \chi_0} E_z^n(i, j) + \frac{1}{\epsilon_\infty + \chi_0} \Psi_z^n(i, j) \quad (5.43)$$

$$H_x^{n+\frac{1}{2}}(i, j-\frac{1}{2}) = H_x^{n-\frac{1}{2}}(i, j-\frac{1}{2}) + \frac{\Delta t}{\mu \Delta x} (E_z^n(i, j-1) - E_z^n(i, j)) \quad (5.44)$$

$$H_y^{n+\frac{1}{2}}(i+\frac{1}{2}, j) = H_y^{n-\frac{1}{2}}(i+\frac{1}{2}, j) + \frac{\Delta t}{\mu \Delta x} (E_z^n(i+1, j) - E_z^n(i, j)) \quad (5.45)$$

The only difference between the Debye and the Lorentz model is in the multiplicative coefficients.

The (FD)²TD method has been applied in the computation of the reflection coefficient for an air-water interface over a wide frequency band. The result was in excellent agreement with the exact results⁴⁸. In the calculation of the complex reflection and transmission coefficients for a pulsed plane wave incident on a plasma slab, the (FD)²TD method has shown excellent agreement with the exact frequency domain calculations⁴⁹. These numerical results have demonstrated and confirmed the validity and accuracy of the (FD)²TD method.

5.5 Comparison of the Four-step Method and the (FD)²TD Approach

As both the four-step method and the (FD)²TD method had been shown to give accurate numerical results, the choice between them depends on the efficiency (computation time per iteration), ease of convergence, memory storage requirement and ease of implementation. Consider two-dimensional electromagnetic scattering simulations in the TE polarization with electric dispersive materials alone, the set of updating equations in the four-step method (equations (5.31), (5.32), (5.33), and (5.34)) and in the (FD)²TD method (equations (5.42), (5.43), (5.44), and (5.45)) are compared. In terms of the efficiency of the algorithm, the four-step method requires thirteen

(13) additions and seven (7) multiplications per iteration. The (FD)²TD method requires ten (10) additions and seven (7) multiplications per iteration. Although the four-step method requires three more additions, the actual increase in computation time is minimal when all other computations are taken into account (for instance, the boundary conditions and initialization of the variables). In terms of convergence, both algorithms should take approximately the same number of wave cycles to converge. This is because in the four-step method, both the electric displacement D and the electric field E must converge. For the (FD)²TD approach, both the electric field E and the summation variable Ψ must converge before steady-state is reached. Moreover, convergence of the TDFD approach mainly depends on the simulated structure²⁵ and should not differ between the two methods. Therefore, in terms of efficiency and ease of convergence, both approaches are similar.

In terms of ease of implementation, however, the (FD)²TD approach is superior to the four-step method. The form of the updating equations in the (FD)²TD method is identical for all mathematical models of electric susceptibility. Hence, it is not necessary to modify the updating equations with different mathematical models. Only the multiplicative coefficients (terms involving χ_0 and $\Delta\chi_0$) are affected, and this only requires a change in the initialization routine. In the four-step approach, the updating equations are model dependent. Since the time-domain relationship between the electric field and the electric displacement is converted directly from the frequency-domain counterpart via the substitution of equation (5.26), the number of variables and hence the number of additions and multiplications depend on the mathematical model of the electric susceptibility. The Lorentz model requires more variables than the Debye model because the latter model involves only first order time derivatives (and hence requires two levels of time information) whereas the former model involves second order time derivatives (and therefore requires three levels of time information). Model dependent updating equations of the four-step approach means that this approach is not flexible in adapting to materials of different characteristics. Furthermore, the four-step method generally requires more memory storage than the (FD)²TD approach. Memory requirement for the conventional, four-step, and (FD)²TD approaches are compared in Table 5.1 where the Lorentz model of permittivity is assumed for the four-step method. In the conventional method, a total of five variables are needed in the updating equations for two-dimensional simulations. The (FD)²TD method requires three (3) more variables

whereas the four-step method requires nine (9) more. As a result, the (FD)²TD approach is chosen for implementation over the four-step method based on all these considerations.

Approach	Polarization	# of Field Variables	# of Coefficients	Total Variables
Conventional	TE	3	2	5
	TM	3	2	5
	3-D	6	2	8
Four-step	TE	7	3	10
	TM	11	3	14
	3-D	18	3	21
(FD) ² TD	TE	4	3	7
	TM	5	3	8
	3-D	9	3	12

Table 5.1 Memory storage requirement of the conventional, four-step, and (FD)²TD approaches. For two-dimensional simulations in the TE and TM polarizations. The TM polarization requires more variables than the TE polarization for both the four-step and the (FD)²TD methods because there are two electric field variables (E_x and E_y) in the TM polarization whereas there is only one (E_z) in the TE polarization. For three-dimensional simulations, memory requirement of the four-step method is excessive.

5.6 Implementation of the (FD)²TD Approach

In the implementation of the (FD)²TD method, a question arises as to which susceptibility model to use for the materials in the simulation domain. To answer this question, one must keep in mind that the interest of the user is the response of the structure to an electromagnetic excitation at a specific and fixed frequency. Therefore, the mathematical model must give the true material property at the interested frequency. At all other frequencies, the model of the susceptibility function may differ from the real material property and will not affect the simulation results. Based on this consideration, the Debye model is well-suited for materials in which the real part of its relative permittivity is greater than or equal to 1.0, and the Lorentz model is suitable for materials in which the real part of its relative permittivity less than 1.0 (even less than zero). The physical reason for this choice of model is that materials in which $\epsilon_r = n_r^2 - n_i^2 \geq 1$ is more ionic than metallic in nature and hence the Debye model of ionic polarizability is more suitable. The Lorentz model with $\omega_0 = 0$ indicates that the material has a resonance at D.C., meaning that the material is more metallic than ionic in nature.

Having determined the applicability of each of the susceptibility models, the next step is to determine the parameters associated with each model. Taking $\epsilon_\infty = 1.0$ in the Debye model, the parameters ω_0 , ϵ_s as well as χ_0 and $\Delta\chi_0$ are determined as follows

$$\omega_0 = \frac{(\epsilon_r - 1.0) \omega_i}{\epsilon_i} \quad (5.46)$$

$$\epsilon_s = (\epsilon_r - 1.0) \left[1 + \left(\frac{\omega_i}{\omega_0} \right)^2 \right] + 1.0 \quad (5.47)$$

$$\chi_0 = (\epsilon_s - 1.0) (1 - e^{-\omega_0 \Delta t}) \quad (5.48)$$

$$\Delta\chi_0 = (\epsilon_s - 1.0) (1 - e^{-\omega_0 \Delta t})^2 \quad (5.49)$$

For the Lorentz model, the parameters are

$$\omega_0 = \frac{\omega_i \epsilon_i}{1 - \epsilon_r} \quad (5.50)$$

$$\omega_p^2 = (1 - \epsilon_r) (\omega_i^2 + \omega_0^2) \quad (5.51)$$

$$\chi_0 = \frac{\omega_p^2}{\omega_0} \Delta t - \frac{\omega_p^2}{\omega_0^2} (1 - e^{-\omega_0 \Delta t}) \quad (5.52)$$

$$\Delta\chi_0 = -\frac{\omega_p^2}{\omega_0^2} (1 - e^{-\omega_0 \Delta t})^2 \quad (5.53)$$

where ϵ_r and ϵ_i are respectively the real and imaginary parts of the relative permittivity and ω_i is the angular frequency of the incident radiation. Note that for lossless materials, the Debye model is used. The parameters for such materials become

$$\omega_0 = \infty \quad (5.54)$$

$$\epsilon_s = \epsilon_r \quad (5.55)$$

$$\chi_0 = \epsilon_r - 1 \quad (5.56)$$

$$\Delta\chi_0 = \epsilon_r - 1 \quad (5.57)$$

These formulas apply for all components of the electric field and electric displacement.

5.7 Performance Evaluation

5.7.1 Accuracy

The accuracy of the (FD)²TD algorithm was discussed for an air-water interface over a wide frequency band⁴⁸ as well as for pulsed plane wave incident on a plasma slab⁴⁹. In this section, calculations from the (FD)²TD algorithm for two simple planar structures is compared with the Fresnel formulas for reflection³¹. The first structure contains two semi-infinite materials. Electromagnetic energy of wavelength 248 nm is incident from air (vacuum) with a refractive index of 1. A dielectric material with a refractive index of (n=0.85, k=2.0) has a planar interface with air. The second structure is a three-layer structure with 100 nm of a hypothetical material (n=1, k=2) sandwiched between two semi-infinite layers of air. The incident wavelength in this case is 500 nm. The simulation results tabulated in Table 5.2 shows excellent agreement with theoretically calculated values.

Structure	τ (Simulation)	ρ (Simulation)	Fresnel Theory
Two-layer		0.532	0.542
Three-layer	0.093		0.091

Table 5.2 Simulation results of reflection coefficients using the (FD)²TD algorithm and the theoretically calculated values for normal incidence on dielectric stacks. The slight discrepancy between the simulations results and the theoretical calculations are due to discretization and floating point errors.

5.7.2 Efficiency

To compare the efficiency of the (FD)²TD approach with the conventional approach, three geometries shown in Figure 5.1 were simulated with both the (FD)²TD and the conventional approaches. The three structures simulated were: a) A 5X chromeless phase-shift mask of linespace patterns at an incident wavelength of 0.248 μm in which all materials are lossless. The period of the simulation domain is 5.0 μm , corresponding to a feature size of 0.25 μm . b) A planar structure of air (n=1.0, k=0.0) on 400 nm of a hypothetical photoresist material (n=1.5, k=1.0) on silicon (n=4.0, k=2.0) with an incident wavelength of 0.248 μm . c) Photoresist (n=1.68, k=0.0273)

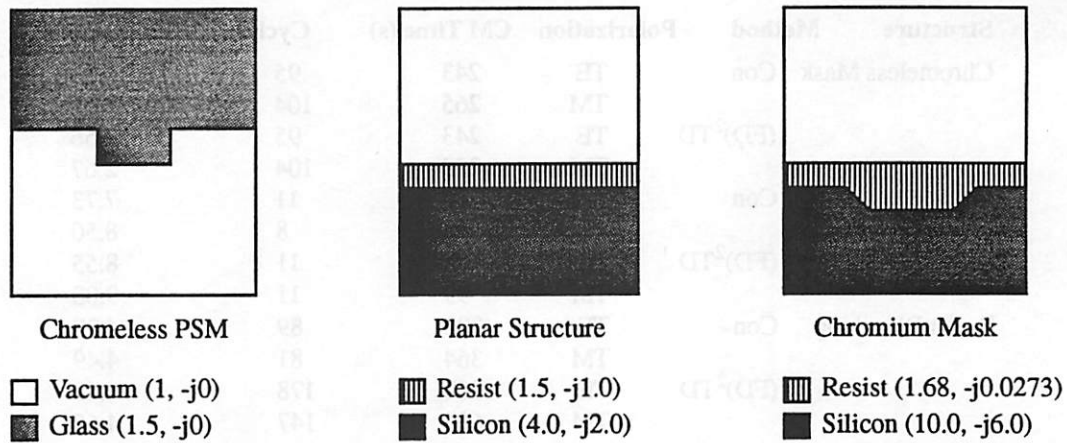


Figure 5.1 Three different structures used to assess the efficiency of the $(FD)^2TD$ algorithm. The first structure is a 5X chromeless phase-shifting mask (left), the second structure consists of three planar layers (middle), and the third is a silicon step covered with photoresist.

bleaching over an underlying silicon step ($n=10.0$, $k=6.0$). The structure is periodic with a period of $4.0 \mu\text{m}$ and the silicon step is $2.0 \mu\text{m}$ wide and $0.5 \mu\text{m}$ high with an edge slope of 1.0. The photoresist (with $a=0.74$, $b=0.20$, and $c=0.012$) is exposed with a dose of 50.0 mJ/cm^2 at $0.365 \mu\text{m}$. This exposure dose is divided into five dose steps in the simulations. All these simulations are done with materials which have the real parts of their refractive indexes larger than the imaginary parts because the conventional approach is not applicable for materials with larger imaginary parts than real parts. Simulation results in Table 5.3 show that for lossless materials, the efficiency of the $(FD)^2TD$ approach is the same as the conventional approach, both in terms of efficiency per wave cycle and number of cycles for convergence. For the lossy planar structure, iteration time per wave cycle of the $(FD)^2TD$ method increases by less than ten per cent over the conventional approach. This increase is not significant because the number of wave cycles for convergence is small for planar structures. For the photoresist bleaching example, the iteration time per wave cycle of the $(FD)^2TD$ method increases only by about three per cent over the conventional approach. However, the actual computation time is doubled due to the larger number of wave cycles required for convergence.

The reason for the larger number of wave cycles for convergence in the $(FD)^2TD$ is due to the small magnitude of the lossy part of the photoresist material. Referring to equation (5.40),

Structure	Method	Polarization	CM Time (s)	Cycles	Time/Cycle
Chromeless Mask	Con	TE	243	95	2.56
		TM	265	104	2.55
	(FD) ² TD	TE	243	95	2.56
		TM	278	104	2.67
Lossy Planar	Con	TE	85	11	7.73
		TM	68	8	8.50
	(FD) ² TD	TE	94	11	8.55
		TM	99	11	9.00
Resist Bleaching	Con	TE	390	89	4.38
		TM	364	81	4.49
	(FD) ² TD	TE	800	178	4.49
		TM	684	147	4.65

Table 5.3 Comparison of the performances of the (FD)²TD method and the conventional approach. The (FD)²TD method takes about 10% more computation time per wave cycle of iteration.

convergence of the variable $\Psi_z^n(i, j)$ depends on the value of $\Delta\chi_0$. A small value of $\Delta\chi_0$ means fast convergence because the first factor in (5.40) is exponentially decreasing with time. For materials which have small but non-zero imaginary refractive index, convergence of $\Psi_z^n(i, j)$ is slow because of a relatively large $\Delta\chi_0$ value. Therefore, for structures containing slightly lossy materials, the conventional TDFD scheme should be used for better efficiency.

5.8 Conclusions

Different techniques which may be applied to model dispersive materials with the TDFD method have been assessed. The complex field approach is not applicable as the algorithm is unstable for lossy materials. The (FD)²TD approach and the four-step approach are both suitable in modeling dispersive materials. The (FD)²TD method is chosen for implementation because of its advantages in memory storage requirement and the ease of implementation over the four-step method. The speed (per iteration) of the (FD)²TD method is only slightly slower (less than 10%) than that of the conventional TDFD approach, but the total computation time of the (FD)²TD approach may double that of the conventional method if a slightly lossy material is present because of the greater number of wave cycles for convergence. Therefore, the conventional TDFD method is preferred in the modeling of materials with small imaginary refractive indexes.

In TEMPEST, two permittivity models are implemented in the (FD)²TD method: the Debye model which models ionic-like materials and the Lorentz model which models metallic-like materials. Furthermore, with accurate mathematical models for the electric permittivity and magnetic permeability, the (FD)²TD approach has the potential of analyzing the frequency response of a structure by examining the frequency spectrum of its impulse or square wave response. Moreover, anisotropic materials can be modeled with additional terms in the updating equations.

Chapter 6

TEMPEST Software Package

6.1 Introduction

The numerical techniques presented in the previous three chapters are implemented in the program TEMPEST on the connection machines CM-2 and CM-5. This chapter discusses some additional numerical aspects of the program as well as supporting routines of the software package including a link to the simulation program SPLAT⁸⁹ for aerial image analysis. While parallel computers are expected to give future leverage in the modeling of photolithography, currently the supercomputer architectures are still evolving. The CM-2 and the CM-5 were chosen due to their availability as massively-parallel computers. The particular implementation will probably evolve with time along with the computer architectures. One of the areas of the current implementation which will likely evolve further is the efficiency of the numerical boundary conditions as affected by the increasing generality of computer architectures.

The connection machine CM-2²⁹ announced in 1985 operates in the single-instruction multiple-data (SIMD) mode where each processor has relatively low intelligence and executes the same instruction on the data. The next generation of the connection machine CM-5⁸⁸ available in 1992 operates in both the SIMD and the single-program multiple-data (SPMD) modes. In SPMD machines, the processors (which have higher intelligence than those in the CM-2) execute the same program but not necessarily the same instruction. This feature of the CM-5 makes it more flexible in the modeling of a wide variety of problems ranging from cosmology to molecular biology³⁴. There is still another operating mode called the multiple-instruction multiple-data (MIMD) mode in which different processors within the supercomputer can execute different programs simultaneously. This programming mode is supported on architectures such as the Intel Paragon iPSC³⁰ and the Kendall Square Research KSR1³⁵.

This chapter begins with a discussion of the reduced computation efficiency due to the numerical boundary condition. The importance of proper excitation of the simulation domain is then shown. Convergence of the electromagnetic fields is found to depend primarily on the physics

of the problem. The software package TEMPEST is also briefly described. Besides the electromagnetic fields solver TEMPEST, the package contains other supporting routines such as input file checking. Post processing options include data processing and display utilities, as well as image synthesis via a link to SPLAT⁸⁹. This linkage which combines electromagnetic scattering and optical system effects is also discussed.

6.2 Reduction of Computation Efficiency due to the Boundary Condition

Termination of the simulation domain leads to a different set of updating equations for the boundary nodes. This is discussed in Chapter 4. Since the boundary nodes have a different stencil from the interior nodes, they need to be solved separately from the interior nodes. For massively-parallel computer architectures such as the CM-2²⁹, the second order boundary condition consumes about 75% of the computation time whereas only 25% is used by the interior nodes²⁵. The reason is that while updating the boundary nodes, the interior nodes must be idled. This is an unworthy price to pay because the number of boundary nodes usually constitutes less than 1% of the total number of simulation nodes.

Increased efficiency can be achieved by implementing more efficient boundary conditions which reduce the number of additions and multiplications in the boundary equations. A better solution to the problem is to make use of the computer resource more effectively, i.e., all the processors on the parallel machine should be kept busy as much as possible. This is possible with the more recent version of the connection machine CM-5⁸⁸ as it can operate in the SPMD programming mode. In the SPMD programming mode, each processor is running the same program (and hence single-program) on different sets of data (and hence multiple-data). The single program is not limited to parallel programs. It can also be a serial program. Thus, more efficient computer usage can be achieved by decomposing the simulation domain in such a way that each processor contains the same number of boundary and interior nodes. A serial program with an if-then-else loop can then be written in such a way that all the processors on the parallel machine are solving the same equation at the same time, i.e., all the processors are simultaneously solving either the interior equation or the boundary equation. This avoids idling of computation resource as is the case in the SIMD programming mode. As an initial implementation on the CM-5, however, TEMPEST

is programmed in the SIMD mode, which can be made more efficient in the future by rewriting in the SPMD mode or even the MPMD mode on other parallel machines.

6.3 Domain Excitation

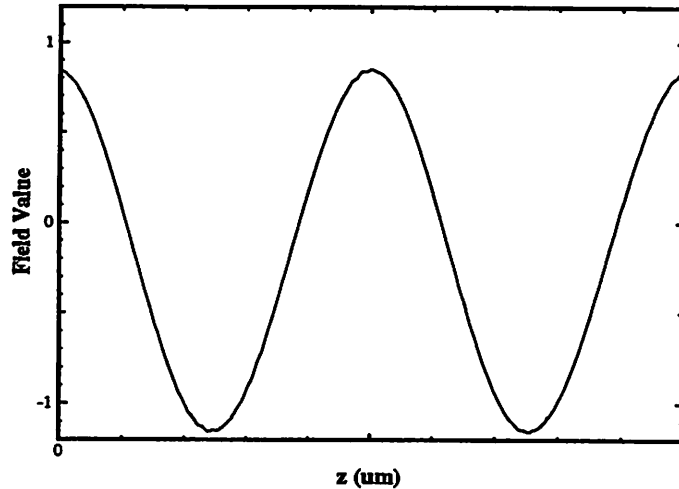


Figure 6.1 The effect of incorrect domain excitation on the steady-state electric field. Although the normalized peak-to-peak amplitude is 2, the normalized electric field oscillates between 0.84 and -1.16 .

Care must be exercised in exciting the simulation domain because an improper method of excitation can lead to inaccurate simulation results. To illustrate, take the simple case of an empty simulation domain under normal incidence. Initially ($t=0$), all the field values are set to zero except for the top layer of simulation nodes, which have a non-zero value of $\sin\phi$. For $\phi = 0$, the simulation result is correct. For $\phi = \pi/2$, however, the simulated steady-state field as shown in Figure 6.1 indicates that the steady-state electric field has a non-zero D.C. offset. While the normalized peak-to-peak amplitude is still 2, the normalized electric field oscillates between $+0.84$ and -1.16 . The reflected electric field at the top boundary should be zero at all time. However, as shown in Figure 6.2, the diffracted field shows a non-zero offset which is constant with respect to time (iteration cycle). In fact, this D.C. offset is dependent on the initial excitation value $\sin\phi$. If $\sin\phi = 0$, then no D.C. offset is introduced and the simulation results are correct.

This anomalous behavior can be explained by considering the numerical boundary conditions. Since the sum of the multiplying coefficients in the numerical boundary condition such

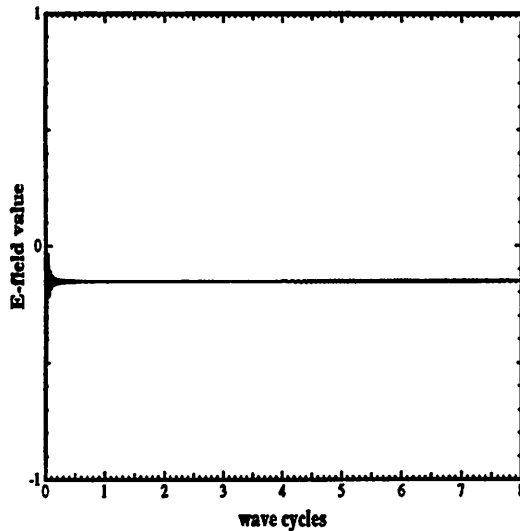


Figure 6.2 The diffracted field shows a non-zero offset which is constant with respect to time. This shows incorrect coupling of the excitation field into the numerical boundary condition.

as equation (4.43) is 1, the numerical boundary condition does not act on D.C. signals, i.e., the numerical boundary condition cannot distinguish between a sinusoidal wave and the same sinusoidal wave plus a D.C. offset. Therefore, for this particular method of excitation, an initial value ($\sin\phi$) dependent D.C. signal is coupled into the diffracted electric field via the boundary condition and results in incorrect simulation results. To elaborate, consider the boundary condition in equation (4.43), the electric field value at the top boundary (Z^{th} node) for the $(n+1)^{\text{th}}$ time step (E_Z^{n+1}) depends on the variables E_Z^n , E_{Z-1}^{n+1} , and E_{Z-1}^n . It is the dependence on E_{Z-1}^{n+1} and E_{Z-1}^n which causes the D.C. offset. Since the boundary equation applies only to the diffracted electric field, the incident electric field must be subtracted from the total electric field before the boundary equation can be applied at the top boundary. At $t=0$, the wave has not propagated to the $(Z-1)^{\text{th}}$ node yet, and the total electric field is zero. The incident electric field should also be zero. However, in order to facilitate computation in the actual computer code, the incident electric field at the $(Z-1)^{\text{th}}$ node has already assumed its value at the second time step when the boundary field value for the first time step is calculated. As a result, subtraction of the incident electric field from the total field at $t=0$ gives a value which is equal to the negative of the initial incident field value when it should

be zero. It is this value which causes the D.C. offset observed, and this is why no error is observed when the domain is excited by $\sin\phi = 0$.

One way to solve this problem is to add a conditional statement in the computer code which gives a zero diffracted field during the first time step. However, addition of this conditional statement will make the simulation program less efficient. A simpler way to solve the problem is to start the simulation assuming that the electromagnetic wave has already propagated several node layers into the simulation domain, i.e., the top few simulation layers have non-zero electric and magnetic field values at $t=0$. As a result, the previous discontinuity at the top boundary is now moved inside the simulation domain. Subtraction of the incident electric field at the $(Z-1)^{\text{th}}$ node during the first iteration step would then give the correct result. The discontinuity inside the simulation domain does not affect the steady-state solution since there is no source to support it. It is eventually absorbed by the numerical absorbing boundary condition.

With this technique, the empty box is again simulated. The steady-state electric field shows the expected sinusoidal shape with no D.C. offset. The diffracted electric field at the top boundary as a function of iteration cycles shown in Figure 6.3 indicates that the field value converges to 0.0 as expected. The diffracted field also shows a transient behavior starting at about 0.3 wave cycle. This transient behavior is caused by the back propagation of the discontinuity inside the simulation domain when the fields are introduced at $t=0$. This excitation method also works well for obliquely incident waves.

6.4 Convergence

In order to study the convergence properties of TEMPEST, the two structures shown in Figure 6.4 are used. Both structures are planar dielectric stacks consisting of three lossless layers of materials. In the first structure, the incident layer is air with a refractive index of $(1.0, -j0.0)$. The second layer has a thickness of $0.5 \mu\text{m}$ and a refractive index of $(2.0, -j0.0)$, and the third layer has a refractive index of $(4.0, -j0.0)$. The free space wavelength of the incident radiation is $0.5 \mu\text{m}$. The second structure is the same as the first, except that the middle layer is $1.0 \mu\text{m}$ thick.

Convergence of the fields is monitored by the reflected electric field at the top of the simulation domain. When the incident wave interacts with the structure, a change in the reflected

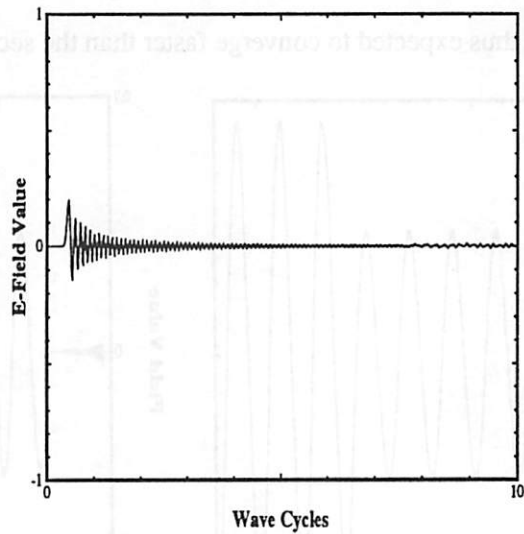


Figure 6.3 Diffracted electric field at the top boundary as a function of wave cycles. The transient behavior which starts around 0.3 wave cycle is caused by the back propagation of the discontinuity associated with the excitation method.

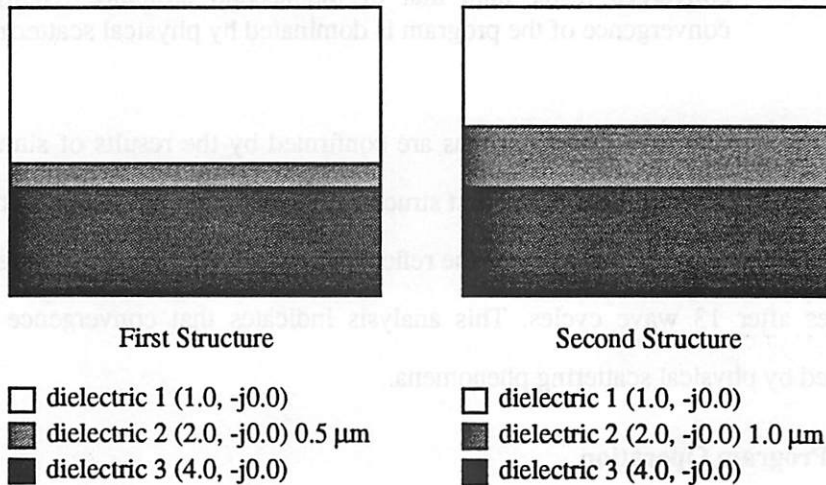


Figure 6.4 Two structures used to study the convergence of the program. Both structures consist of the same materials. The only difference between them is the thickness of the middle layer.

field amplitude occurs whenever a reflection from an interface reaches the top boundary. For the structures under consideration, two changes in the reflected electric field amplitude is expected, once from each of the material interface. Increasing the thickness of the second layer would lead to an earlier occurrence of the first change in reflected field amplitude while the second change in

amplitude is delayed because the second layer is an optically slower material than air (vacuum). The first structure is thus expected to converge faster than the second structure.

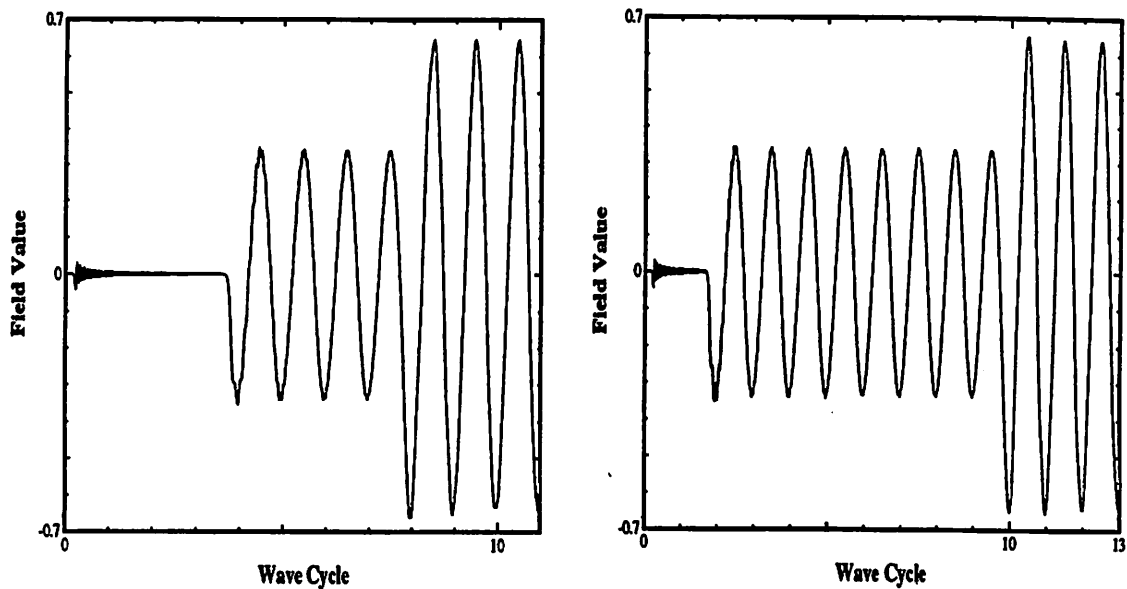


Figure 6.5 Reflected electric field for the two structures. The field of the first structure (left) converges faster than that of the second structure (right). This shows that convergence of the program is dominated by physical scattering phenomena.

These qualitative considerations are confirmed by the results of simulation as shown in Figure 6.5. The reflected field of the first structure shown on the left indicates that the electric field converges in 11 wave cycles whereas the reflected field of the second structure shown on the right converges after 13 wave cycles. This analysis indicates that convergence of the program is dominated by physical scattering phenomena.

6.5 Program Operation

The basic steps of running TEMPEST are shown in Figure 6.6. For a typical simulation, the input file is edited and checked for correctness in the local computing environment. The file is then transferred to the supercomputing environment under which the electromagnetic fields are calculated. Steady-state is normally reached after 5 minutes (30-50 wave cycles) at which point the diffraction harmonics are calculated. These diffraction harmonics are written to an output file which also contains a recapitulation of the input parameters as well as additional information including

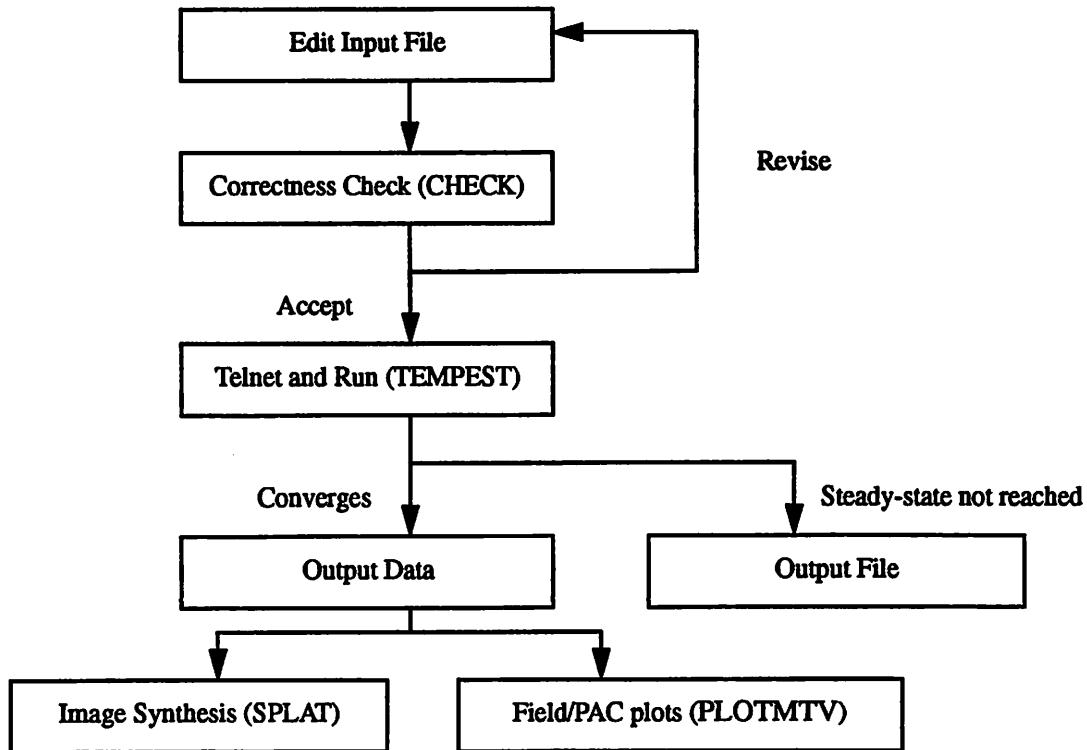


Figure 6.6 The basic steps of running TEMPEST. The software package TEMPEST contains the electromagnetic solver together with other supporting routines.

numerical parameters such as the spatial and temporal discretizations (Δx and Δt), run time and convergence information. The diffraction harmonics can then be used to synthesis the optical image profile of the simulated structure as discussed in the next section. A detail description of program operation as well as other auxiliary routines associated with the software package can be found in the TEMPEST users' guide¹⁰³.

6.6 Image Synthesis

6.6.1 Motivation

TEMPEST calculates the steady-state electromagnetic fields throughout the volume of a structure under the excitation of a monochromatic harmonic field. In many instances in photolithography, however, the interest of the user is not in the electromagnetic fields themselves but the image of the structure as viewed through an optical imaging system. Furthermore, typically

only the intensity distribution resulting from the fields can be observed to validate the simulation results. There thus exists a need to convert the steady-state fields calculated by TEMPEST into an intensity profile. The basic idea is to Fourier transform the electric and magnetic fields across a horizontal plane into the diffraction harmonics from which imaging information can be found.

There are two physical phenomena to consider in extending TEMPEST for use in image formation. First, the imaging systems used in photolithography are (spatially) partially coherent to reduce ringing at the dark-bright transitions whereas illumination is assumed to be coherent in TEMPEST. One way to model partial coherent effects is to superpose simulation results for a lot of different angles of illumination. This approach, although accurate and feasible, generally requires a lot of simulation runs and is inefficient. Hopkins' approximation⁵ can be used to simplify the problem. The key assumption is that the magnitudes of the diffraction efficiencies are independent of the incident angle. This approximation is adequate even for 1X projection systems with a numerical aperture (NA) of less than 0.5. The results which support this conclusion is briefly considered in §6.6.4¹⁰².

The second physical phenomenon to consider is aberration of the imaging system. For non-aberrated systems, the calculation of the optical image is a straightforward integral. For aberrated systems, however, the calculation becomes complicated. This calculation can again be simplified by using Hopkins' approximation to separate mask and imaging system parameters. With this assumption, the calculation becomes primarily that of computation of the transmission cross coefficients⁵ (TCCs). Routines for the calculation of these TCCs are available, for example, in a simulation program called SPLAT⁸⁹. However, SPLAT, which is based on the scalar diffraction theory and assumes infinitesimally thin masks, must be modified to link in the vector diffracted field information from TEMPEST.

6.6.2 TEMEPST-SPLAT Interface

SPLAT simulates aerial images of photomasks with the assumption that the masks are infinitesimally thin and have ideal transitions. The optical image profile of any mask at any spatial point is thus given by⁵

$$I(x, y) = \iiint \text{TCC}(\kappa'_x, \kappa'_y; \kappa''_x, \kappa''_y) M(\kappa'_x, \kappa'_y) M^*(\kappa''_x, \kappa''_y) \bullet e^{-\sqrt{-1}[(\kappa'_x - \kappa''_x)x + (\kappa'_y - \kappa''_y)y]} d\kappa'_x d\kappa'_y d\kappa''_x d\kappa''_y \quad (6.1)$$

where $M(\kappa_x, \kappa_y)$ represents the Fourier coefficients of the mask and the asterisk represents complex conjugation. In SPLAT simulations, the values of $M(\kappa_x, \kappa_y)$ are calculated by Fourier transformation of the ideal mask. Thus, in order to link SPLAT and TEMPEST, the values of $M(\kappa_x, \kappa_y)$ must be modified.

The quantity MM^* for the scalar fields can be thought of as the energy transmitted through the ideal mask. Thus, it is analogous to the Poynting vector $\vec{S} = \vec{E} \times \vec{H}^*$ for the vector fields. Assuming that the mask lies in the xy -plane, the quantity of interest is then the energy travelling in the z -direction. Thus, only the z -component of the Poynting vector $S_z = (E_x H_y^* - E_y H_x^*)$ is of interest. The spatial intensity distribution can thus be expressed by modifying equation (6.1) as

$$I(x, y) = \iiint \text{TCC}(\kappa'_x, \kappa'_y; \kappa''_x, \kappa''_y) [E_x(\kappa'_x, \kappa'_y) H_y^*(\kappa''_x, \kappa''_y) - E_y(\kappa'_x, \kappa'_y) H_x^*(\kappa''_x, \kappa''_y)] \bullet e^{-\sqrt{-1}[(\kappa'_x - \kappa''_x)x + (\kappa'_y - \kappa''_y)y]} d\kappa'_x d\kappa'_y d\kappa''_x d\kappa''_y \quad (6.2)$$

With this connection, rigorous electromagnetic simulation is combined with arbitrary lens aberrations, allowing the study of mask topography effects, partial coherent effects as well as the influence of lens aberrations simultaneously. Different illumination schemes such as annular and quadruple illumination as well as resolution enhancement techniques such as spatial filtering can be modeled. Application is not limited to mask transmission studies, however, because SPLAT can be perceived as imitating the functions of a microscope. Therefore, many problems such as a dark-field or bright-field alignment system can be studied.

6.6.3 Implementation

An interface to SPLAT requires information on the diffraction harmonics of the electric and the magnetic fields in both the x - and y -directions as discussed above. To calculate the diffraction harmonics, Fourier transforms of the instantaneous fields are taken on either the top (for the reflected diffraction harmonics) or the bottom (for the transmitted diffraction harmonics) xy -plane.

Since the quantity $(E_x H_y^* - E_y H_x^*)$ is needed, Fourier transformation must be performed on each of the four field variables E_x, E_y, H_x and H_y . However, since these variables are displaced from one another in the FDTD grid, care must be exercised in obtaining the phase of the diffraction harmonics or the resulting image would be in error. A correction factor must be multiplied to the Fourier transformed variables to take into account the staggering of the numerical grid.

To illustrate, the two-dimensional discrete Fourier transform of any variable F is found via

$$\hat{F}(\kappa_x, \kappa_y) = \sum_i \sum_j F(i, j, k) e^{\sqrt{-1}(\kappa_x i \Delta x + \kappa_y j \Delta y + \kappa_z k \Delta z)} \quad (6.3)$$

Since the node (i, j, k) in the simulation domain contains the variables $E_x(i + 1/2, j, k + 1/2)$, $E_y(i, j + 1/2, k + 1/2)$, $H_x(i, j + 1/2, k)$ and $H_y(i + 1/2, j, k)$, the phase factor inside the integral takes on different values for the different variables E_x, E_y, H_x , and H_y . For instance,

$$\hat{E}_x(\kappa_x, \kappa_y) = \sum_i \sum_j E_x(i + 1/2, j, k + 1/2) e^{\sqrt{-1}(\kappa_x [i + 1/2] \Delta x + \kappa_y j \Delta y + \kappa_z [k + 1/2] \Delta z)} \quad (6.4)$$

$$\hat{E}_y(\kappa_x, \kappa_y) = \sum_i \sum_j E_y(i, j + 1/2, k + 1/2) e^{\sqrt{-1}(\kappa_x i \Delta x + \kappa_y [j + 1/2] \Delta y + \kappa_z [k + 1/2] \Delta z)} \quad (6.5)$$

$$\hat{H}_x(\kappa_x, \kappa_y) = \sum_i \sum_j H_x(i, j + 1/2, k) e^{\sqrt{-1}(\kappa_x i \Delta x + \kappa_y [j + 1/2] \Delta y + \kappa_z k \Delta z)} \quad (6.6)$$

$$\hat{H}_y(\kappa_x, \kappa_y) = \sum_i \sum_j H_y(i + 1/2, j, k) e^{\sqrt{-1}(\kappa_x [i + 1/2] \Delta x + \kappa_y j \Delta y + \kappa_z k \Delta z)} \quad (6.7)$$

In order to determine the different correction factors for the different nodes, a reference must be chosen. For the node (i, j, k) , the reference spatial location is chosen to be at $(i + 1/4, j + 1/4, k + 1/4)$. Thus, the correction factors for the diffraction harmonic with wave numbers $(\kappa_x, \kappa_y, \kappa_z)$ are respectively $\exp[\sqrt{-1}(-\kappa_x \Delta x/4 + \kappa_y \Delta y/4 - \kappa_z \Delta z/4)]$, $\exp[\sqrt{-1}(\kappa_x \Delta x/4 - \kappa_y \Delta y/4 - \kappa_z \Delta z/4)]$, $\exp[\sqrt{-1}(\kappa_x \Delta x/4 - \kappa_y \Delta y/4 + \kappa_z \Delta z/4)]$, and $\exp[\sqrt{-1}(-\kappa_x \Delta x/4 + \kappa_y \Delta y/4 + \kappa_z \Delta z/4)]$ for $E_x(i + 1/2, j, k + 1/2)$, $E_y(i, j + 1/2, k + 1/2)$, $H_x(i, j + 1/2, k)$ and $H_y(i + 1/2, j, k)$. For example, the Fourier coefficients of the E_x component is

$$\begin{aligned}\hat{E}_x(\kappa_x, \kappa_y) &= e^{\sqrt{-1}(-\kappa_x \Delta x/4 + \kappa_y \Delta y/4 - \kappa_z \Delta z/4)} \sum_i \sum_j E_x(i + 1/2, j, k + 1/2) e^{\sqrt{-1}(\kappa_x i \Delta x + \kappa_y j \Delta y)} \\ &= e^{\sqrt{-1}(-\kappa_x \Delta x/4 + \kappa_y \Delta y/4 - \kappa_z \Delta z/4)} \text{DFT}[E_x]\end{aligned}\quad (6.8)$$

where $\text{DFT}[E_x]$ represents the discrete Fourier transform of E_x .

6.6.4 Validity of Hopkins' Approximation

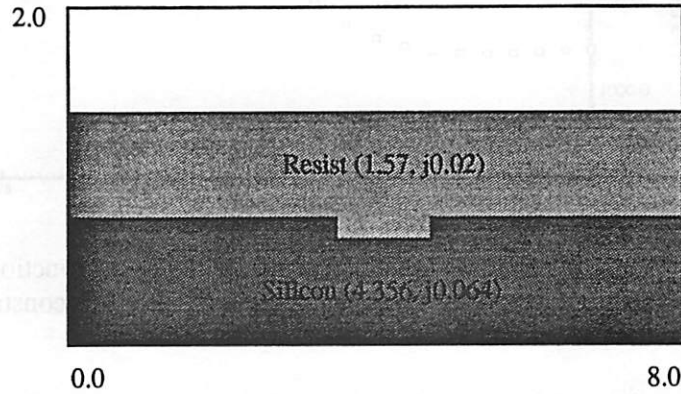


Figure 6.7 Alignment mark structure used in the study of the validity of Hopkins' approximation. The mark is 600 nm wide and 150 nm deep. The period of the simulation domain is 8.0 μm .

Intuitively, the assumption of constant diffraction efficiencies with respect to illumination angle should be valid for small angles. However, the smallness of the incident angle requires quantification. Consider the alignment mark structure shown in Figure 6.7. The mark is 600 nm wide (1.2λ) and 150 nm deep (0.3λ), and is illuminated at 0.488 μm . For a $m2\pi$ phase difference (where m is an integer) between the left and right boundaries¹⁰², angular steps of about 3.5° can be used. The results of simulations performed on this alignment mark illustrated in Figure 6.8 show that the magnitudes of the diffraction efficiencies are more or less constant for illumination angles which are less than 30° . This corresponds to an NA of 0.5, larger than the numerical aperture used in the alignment collection optics for this application. Thus for this application, only the diffraction efficiencies calculated for normal incidence are necessary.

In other applications, diffraction calculations at several oblique angles may be necessary. A measure of a reasonable step size can be determined by drawing the parallelism between

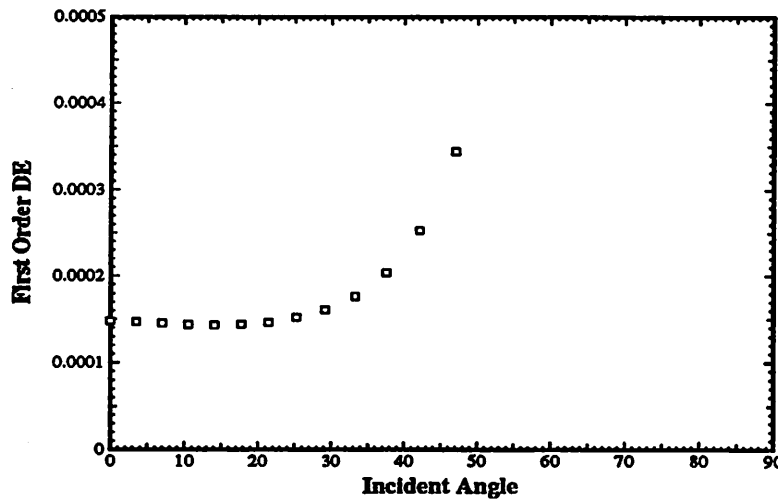


Figure 6.8 First order diffraction efficiency magnitude as a function of the incident angle for an alignment mark. The magnitude is more or less constant for incident angles less than about 30°.

electromagnetic scattering of silicon wafer structures and antenna theory. For a uniform rectangular aperture of length a , the half-power width in degrees is⁴⁴

$$\Delta\theta = 51^\circ (\lambda/a) \quad (6.9)$$

Angular steps three or four times smaller than $\Delta\theta$ would likely be adequate. The angles allowed in TEMPEST simulations are given by $m\lambda = d\sin\theta$ ¹⁰². Using the small angle approximation and converting radians to degrees gives

$$\Delta\theta_{\text{TEMPEST}} = 57^\circ (\lambda/d) \quad (6.10)$$

Thus, choosing the period to be four times the structure size ($d \geq 4a$) gives angular steps about four times smaller than the full width half maximum bandwidth as desired. Since in most applications the period d is a parameter which can be freely chosen for simulation purposes, increased angular accuracy can be obtained.

6.7 Conclusions

Some implementation issues of TEMPEST and the basic operation of the program are presented. An important finding with regard to implementation (which ensures accurate simulation results) is that more than one layer of simulation nodes must be excited initially (at $t=0$).

Convergence of the electromagnetic fields is found to depend primarily on physical scattering phenomena. This has a favorable consequence for problems in photolithography as the rate of convergence does not deteriorate with problem size.

The software package includes auxiliary routines which cater to user convenience and remote use of the connection machine. Linkage with the simulation program SPLAT allows the undertaking of combined scattering and imaging problems. The combination of rigorous scattering analysis and optical image system analysis is important in predicting the aerial images of structures such as photomasks and alignment marks.

Although the current implementation is not optimal, improved implementations will likely evolve from this experience. For example, improvement in computation efficiency could be accomplished by rewriting the program in the SPMD or the MPMD mode. Despite its imperfections, the current implementation is effective in modeling important technological issues in photolithography. Validation of TEMPEST through comparison with experimental results as well as applications of the program in assessing technological issues are presented in the next two chapters.

Chapter 7

Two-dimensional Applications: Phase-shifting Mask Studies

7.1 TEMPEST Applications

The possible applications of TEMPEST in photolithography are diverse. Problems in alignment mark signal integrity, metrology, reflective notching, and mask transmission can be studied. Many of these problems are basically two-dimensional and have been studied with the initial TE polarization version of TEMPEST²⁵. These include reflective notching⁸¹, alignment mark signal integrity⁹⁹, photomask edge and coating effects¹⁴, and polysilicon gate metrology⁸². Extensions of TEMPEST to the TM polarization as well as oblique incidence¹⁰² made possible the examination of polarization effects in mask transmission¹⁰⁰, phase-shifting mask edge effects^{73,101}, and the effects of multi-layer coating defects on reflective x-ray masks⁶⁶. These simulation results have proven to be useful for the integrated circuit fabrication industry.

In this chapter, the contribution by the author on one of these examples, namely two-dimensional phase-shifting mask structures^{73,101}, is examined to illustrate the usefulness and validity of TEMPEST. The simulation program is used to provide physical insight on the extent to which the non-planar mask topography affects image quality in optical projection printing. Design compensation data are also provided for certain PSM technologies. Since the PSMs under study are all two-dimensional structures in which one of the dimensions is the mask thickness, mask patterns are limited to one-dimensional, i.e., long line patterns. Furthermore, two-dimensional illumination effects are only modeled by making Hopkins' approximation⁵ as discussed in §6.6. Despite these shortcomings, however, TEMPEST can provide valuable intuition as to the effects of phase-shifter edges on optical signals.

7.2 Simulation Technique

In a TEMPEST simulation, an incident (normal or oblique) wave of arbitrary amplitude profile is excited at the top boundary of the simulation domain. Illumination is assumed to be

monochromatic and linearly polarized, with the electric field or the magnetic field perpendicular to the two-dimensional simulation domain (the TE or TM polarizations). The incident angle can take on discrete values depending on the illumination wavelength and the horizontal dimension of the simulation domain. Steady-state fields are found throughout the simulation domain as the incident field interacts with the topography. Either the transmitted diffraction efficiencies (for transmission masks, for example) or the reflected diffraction efficiencies (for alignment signals, for instance) can be calculated. Partial coherent effects can be approximated by using Hopkins' approximation⁵ as discussed in Chapter 6. Hence, the optical image for Köhler illumination can be calculated by weighing each pair of diffraction field harmonics by the overlap of the illumination and lens acceptance cones.

A typical simulation domain of the phase-shifting mask structures examined in this chapter is divided into a square grid of 1024 by 512, with about 15 simulation nodes per wavelength in the region with the highest refractive index. The incident radiation is assumed to be a normally incident plane wave. Steady-state is reached after about 30 to 50 wave cycles, which takes about 5 minutes on a CM-2 machine with 8192 processors. (Each processor on the CM-2 consists of 64 kilobytes of memory and there are a total of 32768 processors on the CM-2 at the Thinking Machines Corporation in Cambridge, Massachusetts.) The calculated diffracted harmonics are then transferred to a workstation for image synthesis. Image formation in the program is divided into three parts: Fourier transform of the electric field transmitted through the mask (the diffracted harmonics), filtering due to the finite pupil of the collecting lens, and the inverse Fourier transform of the filtered diffracted harmonics.

The diffracted harmonics can be used to gain insight as to when scattering differences between the etched and unetched regions is important. For a phase-shift pattern with odd symmetry such as that of an alternating and chromeless PSMs, simple scalar and thin mask approximations predict that all the even order diffraction harmonics vanish. In particular, the zeroth order or the straight through diffracted order should be zero. In addition, the +1 and -1 orders should be equal. Deviation from these two conditions means an imbalance in the peak intensities as well as image degradation for some depth of focus. This can be illustrated by the special case of when the pitch of the lines and spaces is so small such that the exit pupil only collects the lowest three diffracted

harmonics ($0, \pm 1$) and a three-beam interference results. In this case, if odd symmetry exists, the peak intensities of the 0° region and the 180° region would be equal and the depth of focus would be infinite for a coherent system, because only the ± 1 beams interact. When the zeroth harmonic is non-zero but the $+1$ and -1 harmonics have the same magnitude, it is possible to discern the size of the D.C. (0^{th} order) component from the maximum imbalance in the peak intensity.

7.3 Different Phase-shifting Mask Techniques

Phase-shifting masks (PSMs) have shown promise in increasing the resolution and depth of focus in photolithography. Different PSM techniques (shown in Figure 7.1) such as alternating⁴², attenuated⁴³, outrigger⁸⁷, rim⁶⁷ and chromeless⁹⁰ have been extensively studied in recent years. These different styles require different fabrication techniques, but common to all is the inevitability of non-planar topography because of the necessity to create phase differences. One of the important issues in examining trade-off among different phase-shifting mask technologies is the effects these edges have on the aerial images in a projection printing system. Computer simulation programs such as SAMPLE⁷⁰ and SPLAT⁸⁹ can play a major role in exploring as well as optimizing layout patterns⁶⁴. However, such tools assume that the masks have ideal dark-bright transitions and hence do not model mask edge scattering effects which can be important in PSM technologies.

The detailed shape of the phase-shifter edges (line edge topography) on PSMs has been shown both experimentally¹⁹ and through computer simulation⁴⁷ to have crucial effects on the optical signals that the PSMs create. For PSMs fabricated using the subtractive process, a previous study using the simulation program TEMPEST⁷³ showed that effects of the chromium profile and refractive index are minimal compared to the glass edge profile, and that the difference in transmission for equally sized openings of 0° and 180° means that interchanging 0° and 180° regions on the mask does not result in the same photoresist profiles⁷³. A similar conclusion has been drawn by Yuan¹¹⁰ using an alternative simulation technique. Ramifications of this observation are widespread. In the rim PSM technology, there is a difference between etching the rim or the middle signal region. In the alternating PSM technology, this problem can be addressed by properly shaping the etched glass profile. These simulation results were confirmed by experimental

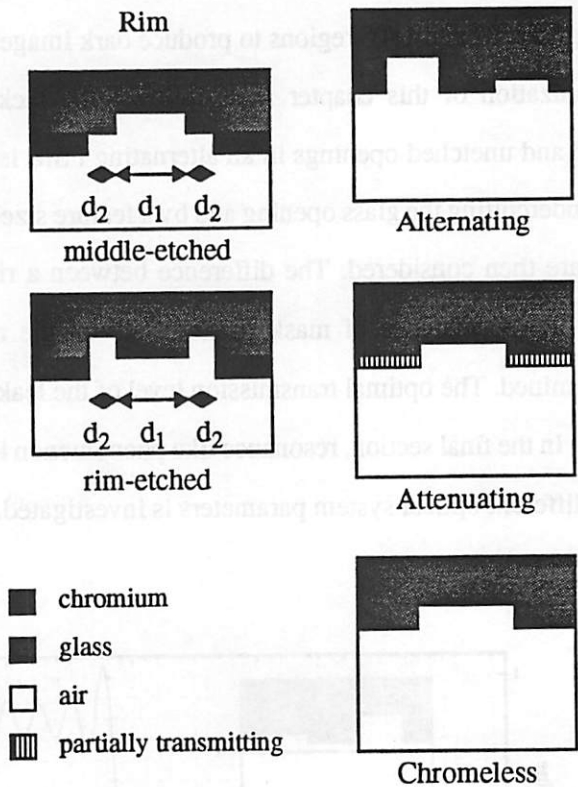


Figure 7.1 Different types of PSMs.

studies⁷³. Besides unequal linewidths due to differences in transmission, two nearby glass edges may interact and produce resonant effects¹⁰¹.

In this chapter, image quality issues in alternating, rim, attenuated and chromeless PSMs are studied. For simplicity, all PSMs examined here are assumed to have been fabricated using the quartz etch process with vertical glass edges. Except for attenuated PSMs, the opaque layer is chromium with vertical edges of thickness of 80 nm and refractive index of (2.5, -j2.0). The four styles of PSMs considered in this chapter are shown in Figure 7.1. An **alternating** mask has openings of 0° and 180° separated by opaque regions. The large clear area of a **rim** mask is surrounded by small transmitting areas which are 180° out of phase. There are two subclasses of rim PSMs. The first has its rim etched to 180° (**rim-etched**) and the second has its large clear area etched to 180° (**middle-etched**). An **attenuated** mask is similar to a conventional mask except that the normally opaque layer is partially transmitting. The phase of the field from the partially transmitting area is 180° with respect to the clear openings so that it contributes to a decreased

image width. A **chromeless** mask relies solely on the destructive interference between light transmitted through the 0° and 180° regions to produce dark images.

The organization of this chapter is as follows: the lack of intensity balance between alternating etched and unetched openings in an alternating PSM is first investigated. Remedies to this problem by undercutting the glass opening and by a feature size-independent bias are proposed. Rim type PSMs are then considered. The difference between a rim-etched and a middle-etched mask, as well as the dependence of mask performance on the rim dimension and the middle dimension are examined. The optimal transmission level of the leaky layer in attenuated type PSM is then considered. In the final section, resonance like phenomenon in dielectric ridges and its effect on imaging with different optical system parameters is investigated.

7.4 Alternating PSMs

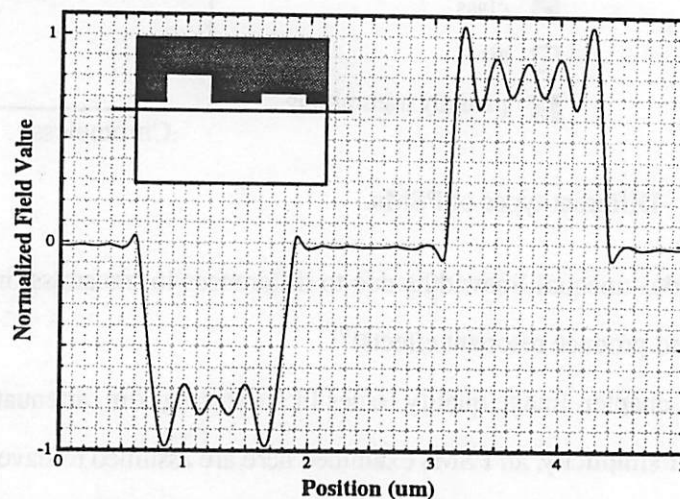


Figure 7.2 Instantaneous electric field just underneath the chromium layer of an alternating PSM with vertical glass edges directly aligned with the chromium edges in the TE polarization. The 0° region (right side) indicates higher energy transmission.

Figure 7.2 shows the instantaneous electric field just underneath the chromium absorption layer of an alternating PSM with vertical glass edges directly aligned with the chromium edges. The unetched 0° region is on the right side and the etched 180° region is on the left side. The 0° region indicates higher energy transmission due to the higher peak field value and the higher curvature of the electric field. The image created by such a mask on a proto-typical 5X optical system (called

System A) with ($\lambda=0.248 \mu\text{m}$, $\text{NA}=0.35$, $\sigma=0.64$, $M=5$) indicates that the peak intensity of the 0° region is 10% higher than that of the 180° region. Ferguson et al.¹⁹ attributed this imbalance in peak intensity to the effective transmission and phase errors associated with the glass edges.

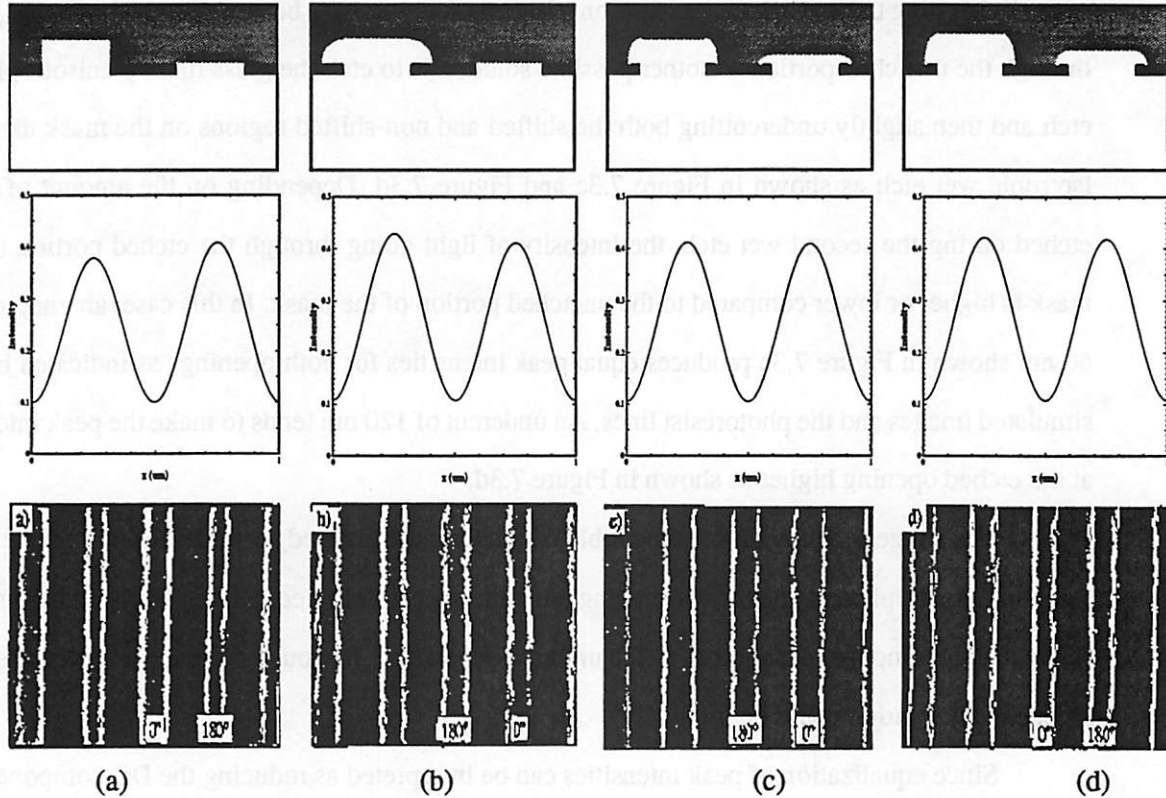


Figure 7.3 Simulated images and exposure results of $0.25 \mu\text{m}$ lines and spaces created by different alternating PSMs. (a) A mask with vertical glass edges creates an intensity imbalance which is manifested as a $0.1 \mu\text{m}$ linewidth difference in the photoresist. (b) Isotropic etching of the 180° glass opening overcompensates the problem and makes the peak intensity at the 180° region higher and the photoresist line wider. (c) Anisotropic etching followed by 60 nm of isotropic etching produces images of equal peak intensity and photoresist lines with equal widths. (d) The same mask as in case (c) except that the amount of isotropic etch is 120 nm tends to overcompensate the problem. (Photoresist pictures courtesy of Christophe Pierrat at AT&T Bell Laboratories.)

This difference in transmission means that equal spaces of 0° and 180° phases on the mask do not print equally on the wafer as illustrated in Figure 7.3⁷³. The simulated intensity profile in Figure 7.3a shows a peak intensity which is 10% lower at the 180° opening than at the 0° opening. This result is confirmed by the SEM picture of the imaged $0.25 \mu\text{m}$ linespaces (negative)

photoresist shown in the same figure. There is a $0.1\ \mu\text{m}$ linewidth difference between the 180° and the 0° openings. This difference in intensity can be reduced by undercutting the glass beneath the opaque chromium layer via isotropic wet etching as shown in Figure 7.3b. However, the intensity of the light going through the etched portion of the mask in this case becomes higher than that going through the unetched portion. Another possible solution is to etch the glass first by anisotropic dry etch and then slightly undercutting both the shifted and non-shifted regions on the mask using an isotropic wet etch as shown in Figure 7.3c and Figure 7.3d. Depending on the amount of glass etched during the second wet etch, the intensity of light going through the etched portion of the mask is higher or lower compared to the unetched portion of the mask. In this case, an undercut of 60 nm shown in Figure 7.3c produces equal peak intensities for both openings as indicated by the simulated images and the photoresist lines. An undercut of 120 nm tends to make the peak intensity at the etched opening higher as shown in Figure 7.3d.

The suggested remedies to the problem by hiding the glass edges under the chromium layer using both isotropic and anisotropic etching are quite successful in equalizing the peak intensities. However, the amount of undercut is feature size dependent. It would be better if a feature size independent solution could be found.

Since equalization of peak intensities can be interpreted as reducing the DC component of the spatial Fourier transform of the mask, equal intensities may be achieved by a design scheme based on biasing the etched 180° region to increase transmission and reduce the DC component of the transformed mask. Figure 7.4 shows the peak intensities for etched (180° and 360°) and unetched (0°) openings of different sizes for the TE and TM polarizations. Simulation results from SPLAT⁶⁹ are included as the solid line for an ideal mask behavior. The differences between the two polarizations for the unetched mask ($\sim 3\%$) and the etched mask ($\sim 1\%$) are slight. However, comparison with the ideal mask shows that the peak intensities are about 8% and 25% lower for the unetched and etched masks respectively. Thus, etching the glass reduces the transmitted intensity by about 17% of the clear field value for small features.

It is interesting to note from the figure that the difference in peak values of the unetched and the etched openings is constant for a wide range of opening sizes ranging from 0.3 to $0.7\ \lambda/\text{NA}$.

This suggests that a possible correction scheme for equal peak intensities is to use a fixed bias of $0.05 \lambda/NA$ for each etched opening on the mask over a size range of 0.3 to $0.7 \lambda/NA$.

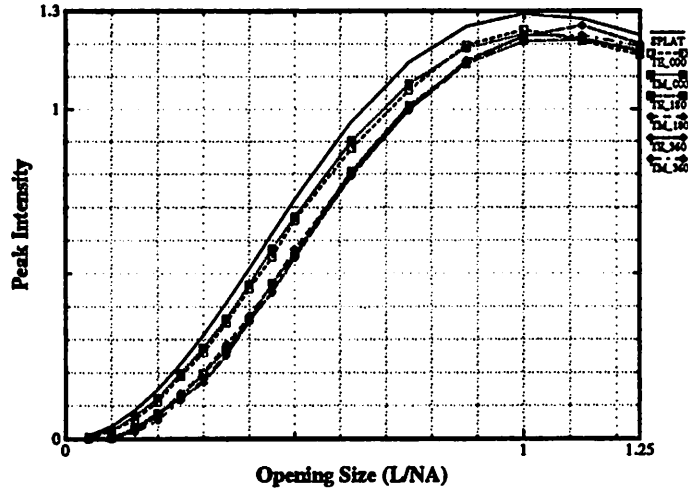


Figure 7.4 Peak intensity as a function of opening size for various degrees of glass etching. The amount of bias seems to be constant at $0.021 \lambda/NA$ for a large range of opening sizes ranging from 0.3 to $0.7 \lambda/NA$.

Table 7.1 shows the ratio of the 0° peak intensity value to the 180° peak value for different feature sizes when a constant bias of $0.042 \lambda/NA$ is applied to the 180° region. The constant bias minimizes the peak intensity differences to within about 1% for all the three feature sizes of 0.35 , 0.42 , and $0.49 \lambda/NA$ (corresponding to 0.25 , 0.30 , and $0.35 \mu\text{m}$ lines and spaces), and this equalization of peak intensities corresponds to the equalization of the critical dimension (CD). It was found that the DC component of the Fourier transformed mask is two orders of magnitude lower in the biased mask than the unbiased mask for a $0.25 \mu\text{m}$ feature size.

Feature	0° Peak / 180° Peak	0° Peak / 180° Peak
0.25	1.080	1.008
0.30	1.042	0.989
0.35	1.042	1.001

Table 7.1 0° to 180° peak intensity ratios for different feature sizes with a constant bias of $+0.042 \lambda/NA$ applied to the 180° region. The constant bias shows marked improvement in peak intensity ratio due to the reduced DC component.

Because of the reduced DC component, the biased masks are also expected to have better defocus behavior than the unbiased masks as explained above. Table 7.2 shows that for a 0.25 μm feature size, the peak intensity ratio changes by only $\pm 1\%$ for the biased mask over a focus range of ± 2 Rayleigh units ($1 \text{ RU} = 0.5 * (\lambda / (\text{NA})^2) = 1.0 \mu\text{m}$). For the unbiased mask, however, the peak intensity ratio changes by more than 6% for a 2 RU of defocus. Thus, applying a constant bias to the 180° regions of alternating PSMs can equalize the peak intensities for different feature sizes as well as improve the DOF.

Defocus	0° Peak / 180° Peak	0° Peak / 180° Peak
-2.0	1.017	0.990
-1.0	1.055	0.997
0.0	1.080	1.008
+1.0	1.069	1.011
+2.0	1.031	1.005

Table 7.2 Peak intensity ratio for 0.25 μm feature size as a function of defocus in Rayleigh units. The biased mask shows better defocus behavior than the unbiased mask.

7.5 Rim PSM

Decreased transmission of etched openings also has important consequences on the choice of the style of rim PSMs. Two types of rim PSMs are shown in Figure 7.1. The first type has its rim etched to 180° (rim-etched) whereas the second type has the middle of the open area etched (middle-etched). The dimension of the middle signal region is d_1 and the dimension of the rim is d_2 . Since an etched glass edge contributes to a decrease in peak intensity, the peak intensity of the middle-etched mask is expected to be lower than that of the rim-etched mask of the same dimensions. This is because the field at the rim can be thought of as subtracting from the field of the middle signal region. When the rim is etched, the field being subtracted is less than what it would be if it were not etched. As a result, the rim-etched mask is expected to give a higher peak intensity than the middle-etched mask. This expected difference in mask transmission must be simulated by a rigorous electromagnetic model because the scalar approach does not model scattering due to the

glass edges, and hence would give identical images for both the rim-etched and middle-etched masks.

Edge effect in rim PSMs was assessed using TEMPEST simulation on a proto-typical 4X deep-UV system (called System B) with ($\lambda=0.248 \mu\text{m}$, $\text{NA}=0.5$, $\sigma=0.4$, $M=4$). For rim masks of dimensions $d_1=1.6 \mu\text{m}$ and $d_2=0.3 \mu\text{m}$, the peak intensity of the rim-etched mask is 10% higher than that of the middle-etched. However, peak intensity is only one of the important aspects of an image, image slope is also important. Figure 7.5 shows that despite a lower peak intensity, the maximum image slope of the middle-etched mask is higher than that of the rim-etched mask. In addition, the middle-etched mask gives a narrower image than the rim-etched mask, which is evident from the locations of the peaks of the image slope.

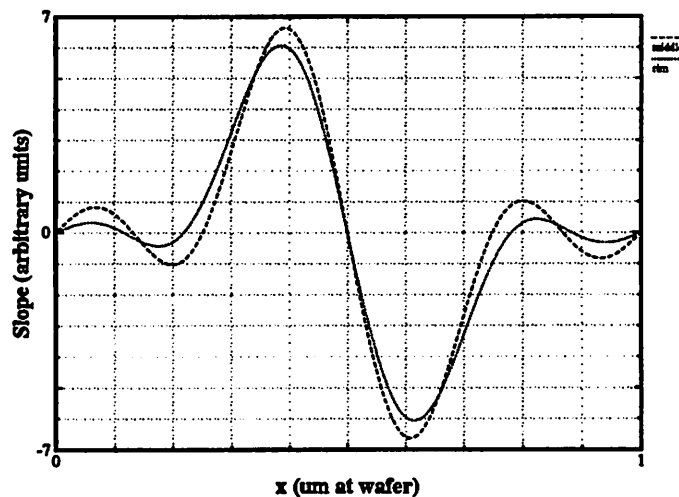


Figure 7.5 Image slope of rim-etched and middle-etched rim PSMs. The middle-etched mask shows a higher image slope and a narrower width, although it shows a lower peak intensity.

In order to determine the importance of the dimensions of the rim (d_2) and the middle (d_1) in affecting the peak intensity, image slope, etc., a set of simulations were done with different d_1 and d_2 values using an approach analogous to a two-level experimental design. Since there is no noise in simulation studies, the significance of the effects due to variations in the d_1 and d_2 dimensions is determined by comparison with the variance of the data over the noiseless cases. The observed parameters are the peak intensity, the image slope, the sidelobe amplitude, and the image width which is defined to be the distance between the steepest points in the image. The nominal

dimension for d_1 is $1.60 \mu\text{m}$ and for d_2 is $0.50 \mu\text{m}$. Variations in the d_1 and d_2 dimensions are $\pm 0.2 \mu\text{m}$.

Table 7.3 shows the dependence of peak intensity on variations of d_1 , d_2 , and the product $d_1 \cdot d_2$ for a rim-etched mask. Increasing both d_1 and d_2 was found to increase the peak intensity, but d_1 is about 2.5 times more effective than d_2 . There is virtually no curvature or the interaction effect $d_1 \cdot d_2$. Thus, the peak intensity is predominately a linear function of d_1 and d_2 .

	d_1 (μm)	d_2 (μm)	$d_1 \cdot d_2$	Peak
	1.80 (+)	0.70 (+)	+	1.426
	1.80 (+)	0.30 (-)	-	1.232
	1.40 (-)	0.70 (+)	-	1.029
	1.40 (-)	0.30 (-)	+	0.931
sum+	<u>2.658</u>	<u>2.455</u>	<u>2.357</u>	
sum -	1.960	2.163	2.261	
difference	<u>0.692</u>	<u>0.292</u>	<u>0.096</u>	
effect	0.346	0.146	0.048	
	1.812σ	0.764σ	0.251σ	$\sigma=0.191$
average				1.155
center	1.60	0.50		<u>1.162</u>
curvature				-0.007

Table 7.3 Application of an approach analogous to a two-level experimental design to study the effects on the peak intensity of the rim and middle dimensions in a rim-etched mask. The effect of middle dimension (d_1) is about 2.5 times more important than the rim dimension (d_2). σ^2 is the variance of the data.

The previous results are for the peak intensity dependence of a rim-etched mask. The same procedure when applied to a middle-etched mask showed little qualitative difference. The effect of the middle dimension is 1.90σ and that of the rim dimension is 0.611σ , where σ^2 is the variance of the data ($\sigma=0.239$). There is again virtually no curvature or second order effect dependence on the term $d_1 \cdot d_2$. In fact, curvature and second order effects were found to be insignificant in all other studies including amplitudes of the sidelobes, the maximum slope, and the width of the image. This is an indication that there is no direct electromagnetic interaction between the phase-shifter edge

and the chromium edge. In fact, interaction between the edges is significant only if they are separated by less than $0.1 \mu\text{m}^{101}$.

From a design point of view, several observations can be made from the results, and these are summarized by the data in Table 7.4. The rim dimension d_2 in a rim PSM functions to increase the image slope and to reduce the linewidth, although increasing it increases the sidelobe amplitude as well. The d_1 and d_2 dimensions should therefore be optimized in such a way that the image width and the sidelobe amplitude are minimized whereas the peak intensity is maximized to increase contrast and throughput. This optimization is not complicated by second order effects, and the response of the image characteristics are almost bilinear with respect to d_1 and d_2 . This suggests that d_2 should be as large as possible within an allowed sidelobe amplitude level. Then d_1 can be chosen based on the peak intensity requirement.

rim etched				
	peak	sidelobe	slope	width
d_1	$1.812\sigma_p$	$-0.257\sigma_s$	$-1.049\sigma_1$	$1.109\sigma_w$
d_2	$0.764\sigma_p$	$1.980\sigma_s$	$1.694\sigma_1$	$-1.664\sigma_w$
$d_1 \cdot d_2$	$0.251\sigma_p$	$-0.073\sigma_s$	$0.132\sigma_1$	$0.0\sigma_w$
σ	0.191	0.109	0.144	0.018
middle etched				
	peak	sidelobe	slope	width
d_1	$1.900\sigma_p$	$-0.181\sigma_s$	$-0.94\sigma_1$	$1.000\sigma_w$
d_2	$0.611\sigma_p$	$1.993\sigma_s$	$1.707\sigma_1$	$-1.667\sigma_w$
$d_1 \cdot d_2$	$0.176\sigma_p$	$-0.051\sigma_s$	$0.443\sigma_1$	$0.333\sigma_w$
σ	0.239	0.138	0.0902	0.015

Table 7.4 The importance of the d_1 and d_2 dimensions on four aspects of the image: peak intensity, sidelobe amplitude, maximum image slope, and image width. The effects are expressed in units of σ , which is the standard deviation of the data points. The rim-etched and middle-etched masks show similar behaviors.

7.6 Attenuated PSM

7.6.1 Transmission Level of the Partially Transmitting Layer

Attenuated PSMs have advantages over other types of PSM techniques because of the compactness of features on the masks and the absence of the phase conflict problem. However, the design of attenuated masks is complicated by the choice of an appropriate level of transmission for the partially transmitting layer. In this study, the partially transmitting layer is assumed to have a transmission of 7% and a phase of 110° when the thickness is $0.1\ \mu\text{m}$. From these data, the index of refraction of the partially transmitting layer can be determined to be $(2.115, -j0.756)$. Thus, a 4% transmitting layer would be $0.126\ \mu\text{m}$ thick and have a phase of 136° .

Figure 7.6 shows the optical image profiles generated by a 5X i-line projection printing system (called System C) with $(\lambda=0.365\ \mu\text{m}, \text{NA}=0.48, \sigma=0.38, M=5)$. These are images in the TE polarization of two attenuated masks with different degrees of intensity transmission of 7% and 4% for the partially transmitting layer. The image corresponding to the lower transmission mask shows a higher peak intensity as well as lower sidelobes. However, the 7% transmission mask shows a smaller feature size than the 4% transmission mask. Therefore, the optimal transmission of the partially transmitting layer is a balance between a tolerable sidelobe amplitude (especially when defocus is taken into consideration) and a narrow image.

To accurately predict the images generated by attenuated masks, a rigorous electromagnetic model is necessary. Figure 7.7 shows the simulated images of a $1.50\ \mu\text{m}$ opening on a 4% transmission attenuated mask using the scalar approach of SPLAT and the rigorous model in TEMPEST for the TE polarization on optical System C. The feature size is equivalent to a k_1 value of 0.4. The two images agree extremely well in the partially transmitting regions. However, the two simulators gave drastically different peak intensities. The peak intensity of the SPLAT image is about 20% higher than that of the TEMPEST image. This difference is attributed to glass edge scattering and is consistent with the data shown in Figure 7.4. Thus, a rigorous simulation model must be used to model attenuated PSMs.

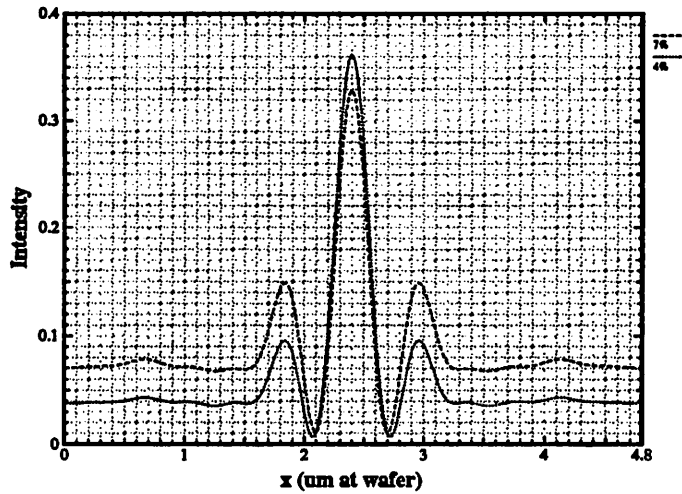


Figure 7.6 Images of two attenuated masks with different degrees of transmission of the partially transmitting layer. The mask with higher transmission gives a smaller feature whereas the mask with lower transmission gives a higher peak intensity and a lower sidelobe amplitude.

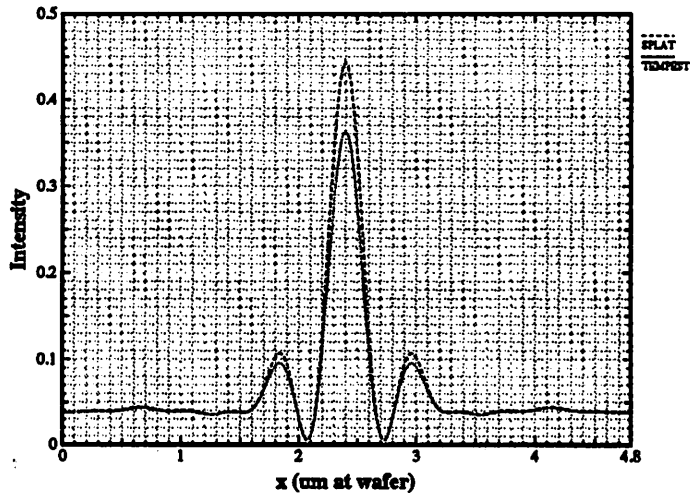


Figure 7.7 Simulated images from SPLAT and TEMPEST of a 1.50 μm opening on a 4% transmitting attenuated mask. The rigorous approach of TEMPEST predicts about a 30% lower peak intensity than the scalar approach of SPLAT.

To investigate the feasibility of printing features at $k_1=0.4$, Table 7.5 shows the image contrast at different focus levels produced by attenuated masks of transmission of 7%, 4%, and 0.5%. Contrast is defined as the ratio of the difference between the main signal intensity value and the sidelobe amplitude to their sum. A negative contrast value means that the sidelobe amplitude is

higher than the main signal. If a contrast of as low as 0.3 can be tolerated, then a 7% transmission mask can barely work with less than ± 1 RU (1 RU = 0.79 μm) of DOF. A minimum contrast of 0.5 would render a 7% transmission mask impossible whereas a 4% mask still functions with about ± 1 RU of DOF. If severe substrate reflection causes large standing waves in the photoresist, then a contrast of at least 0.8 is required. This means that only a mask with low transmission (close to a conventional mask) can be useful.

Defocus	Contrast	Contrast	Contrast
-2.0	-0.281	-0.035	N/A
-1.0	0.194	0.408	0.833
0.0	0.378	0.579	0.864
+1.0	0.324	0.531	0.702
+2.0	-0.020	0.182	N/A

Table 7.5 Image contrast for an isolated open space at $k_1=0.4$ at different focal depths for three attenuated masks with 7%, 4%, and 0.5% transmission. Although the 7% mask gives a narrower image, the image contrast in focus is only 0.38.

A k_1 value of 0.4 is a challenge to the state-of-the-art technology. In production, however, a k_1 value of 0.6 is more common. Table 7.5 shows the image contrast at different focal depths for an opening size corresponding to $k_1=0.6$ on attenuated masks with 7% and 4% transmission. A 7% transmission mask is possible with about 2 RU of DOF if a contrast of about 0.6 is acceptable. For the same contrast level, a 4% partially transmitting mask gives a larger DOF of approximately 3 RU. Thus, at a fixed contrast requirement, a less transparent partially transmitting layer is recommended for smaller features or better DOF latitude. However, less transparency also means a slightly wider image.

7.6.2 Edge Effects on Image Quality

Besides the importance of choosing a suitable transmission level of the attenuating material, two other issues associated with attenuated PSMs are phase error and phase-shifter edge effects on the image quality. In §7.4, glass edge scattering have been shown to reduce transmission

Defocus	Contrast	Contrast
-2.0	0.164	0.333
-1.0	0.558	0.660
0.0	0.681	0.778
+1.0	0.610	0.725
+2.0	0.317	0.472

Table 7.6 Image contrast for an isolated open space at $k_1=0.6$. at different focal depths for two attenuated masks with 7% and 4% transmission. The larger feature size in this case makes a 7% partially transmitting mask possible.

in alternating PSMs. The attenuated PSM technology is also likely to be subjected to edge effects. In this section, these effects are examined by comparing experimental results from the IBM Aerial Image Measurement System (AIMS)⁷ with predictions from simulations using the thin mask approximation (SPLAT) and the rigorous electromagnetic model (TEMPEST). The structures under consideration are isolated space, isolated line and linespace patterns. For all these patterns, masks with five different phases of 155°, 170°, 180°, 190°, and 205° are examined in order to study the interplay among glass edge scattering, phase error and defocus effects.

7.6.2.1 Experimental Technique

Aerial images generated by attenuated masks were measured using the IBM Aerial Image Measurement System (AIMS)⁷. The AIMS tool is constructed on a Zeiss microscope base, with a deep-UV objective used to emulate the imaging lens of a stepper. An aperture is placed within the imaging objective in order to adjust the numerical aperture (NA) of the system. Selection of this aperture depends upon the NA of the stepper under consideration as well as the magnification of the reticle being analyzed. A Mercury-arc lamp generates the exposure energy, with the appropriate wavelength selected through an optical filter. Thus far, the system has been configured to run at both i-line (0.365 μm) as well as deep-UV (0.248 μm) wavelengths. In the illumination system, an interchangeable aperture is used to choose the partial coherence (σ) or to create a modified illumination configuration. The aperture is imaged onto the entrance pupil of the imaging objective

to achieve Köhler illumination. The projected image is collected by a CCD camera with 512x512 pixels at a magnification of approximately 200X from mask to CCD array. The focus of the system is adjusted by moving the stage containing the reticle; typically, the aerial image is collected during one measurement at eleven different positions of the stage. The collected aerial image is normalized by measurements taken in a large clear area to generate a relative intensity.

7.6.2.2 Simulation Context

The context chosen to explore the edge effects is that of 4X deep-UV (248 nm) projection printing with an NA of 0.5 and a σ of 0.54 (called System D). The attenuated PSMs have a chromium layer of thickness of 293 Å and a refractive index of (1.623, -j1.627). The measured intensity transmission is 7% and the phase is 19°. The remaining phase is created by etching into the glass substrate of refractive index (1.5, -j0.0), resulting in a trench with vertical sidewalls.

SPLAT is a FORTRAN program which simulates two-dimensional projection-printing based on the Hopkins' formulation of partially coherent imaging⁵. It assumes that the lithographic mask is infinitesimally thin and thus neglects possible edge effects. Such idealization nevertheless gives good prediction for binary mask patterns. For alternating PSMs, however, effects of glass edge scattering can render the thin-mask approximation in SPLAT in error by as much as 10% of the clear field intensity⁷³. In such instances, rigorous electromagnetic simulation of transmission through masks is required. Thus, the importance of edge scattering is measured by the difference in the simulation results between SPLAT and TEMPEST. For structures in which edge scattering is insignificant, SPLAT can be used to predict mask behaviors. When edge scattering is important, however, the computation intensive model of TEMPEST must be used to obtain useful predictions.

7.6.2.3 Isolated Space

One of the concerns in the fabrication of attenuated PSMs is the exact control of the phase and transmission of the partially transmitting layer due to non-uniformities during the course of layer deposition. This results in the difficulty of maintaining a 180° phase shift between the opening regions and the leaky regions. Although the phase can be controlled to better than one degree for particular features, etch rate fluctuations may result in phase errors of $\pm 10^\circ$ for openings of different

sizes. Study of the effect of phase error on aerial images were done on five different masks with phases of 155° , 170° , 180° , 190° , and 205° , corresponding to phase errors of -25° , -10° , 0° , 10° , and 25° , respectively.

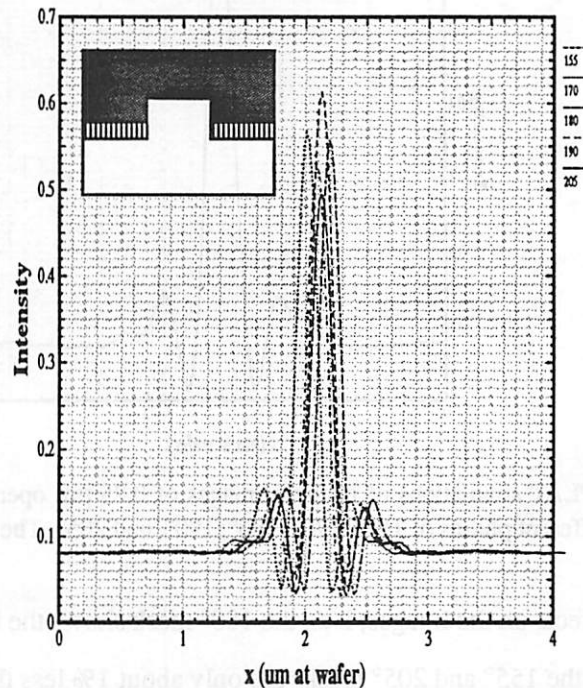


Figure 7.8 AIMS measured in-focus images of $0.25 \mu\text{m}$ openings (wafer dimension) for five different phases of 155° , 170° , 180° , 190° , and 205° . The lateral shift of the images is only a measurement artifact.

AIMS measured in-focus aerial images of $0.25 \mu\text{m}$ space patterns (wafer dimension) for the five different phases of the masks are shown in Figure 7.8. If the masks were infinitesimally thin, the change in the peak intensity with respect to phase would be very gradual and symmetric with respect to 180° . In-focus SPLAT images for the five different masks shown in Figure 7.9 indicate this behavior. However, the experimental and TEMPEST images behave differently. A very rapid and asymmetric behavior is observed in the AIMS measurements in Figure 7.8 as well as from TEMPEST simulation results as shown in Figure 7.10. From the discrepancy between the two simulators and the experimental data, one can conclude that glass edge scattering dominates over phase error in affecting in-focus images of isolated spaces in attenuated PSMs. In fact, simulation results from SPLAT shown in Figure 7.9 suggest that a pure phase error of $\pm 25^\circ$ does not

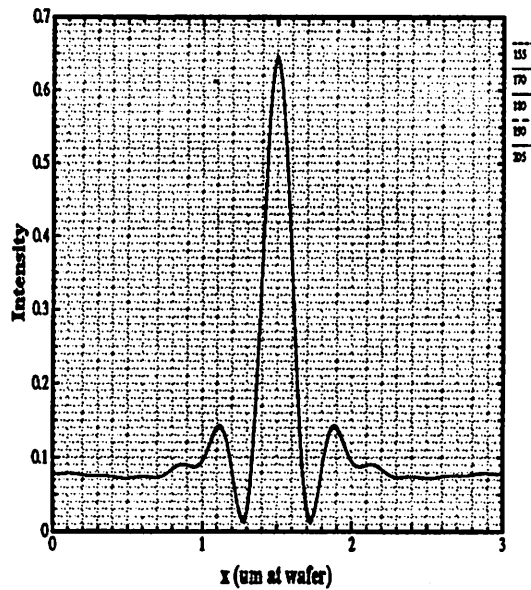


Figure 7.9 SPLAT simulations of in-focus images of $0.25\ \mu\text{m}$ openings (wafer dimension) for five different phases of 155° , 170° , 180° , 190° , and 205° . The images vary by only 1%.

have noticeable effects on the images, i. e., the 180° mask shows the highest peak intensity; but the peak intensities of the 155° and 205° masks are only about 1% less than that of the feature with no phase error. An examination of the normalized SPLAT images shows that all the aerial images are almost identical. This indicates that a pure phase error is non-critical. Scattering due to the glass edges is thus significant as the peak intensity is reduced in an asymmetrical manner about 180° . A 205° ($+25^\circ$ phase error) mask shows a lower peak intensity than a 155° (-25° phase error) mask because the 205° mask has a deeper glass trench and longer glass edges.

This increased scattering with increasing glass trench depth is shown in Figure 7.11 for a space opening on a binary mask. The total energy transmitted through the opening, however, is constant to within 0.5% for the different etched depths despite the decrease in peak intensity. This suggests that the glass edges reduce the peak intensity by diffracting light out of the collection cone of the optical system and the amount of scattering increases with the glass etched depth. The efficiency of glass edge scattering, however, may be dependent on the mask structure. For a $0.5\ \lambda$ NA space opening, the SPLAT image for a conventional binary mask shows a peak intensity which is 30% higher than that of the TEMPEST image. For an opening on an attenuated PSM of the same

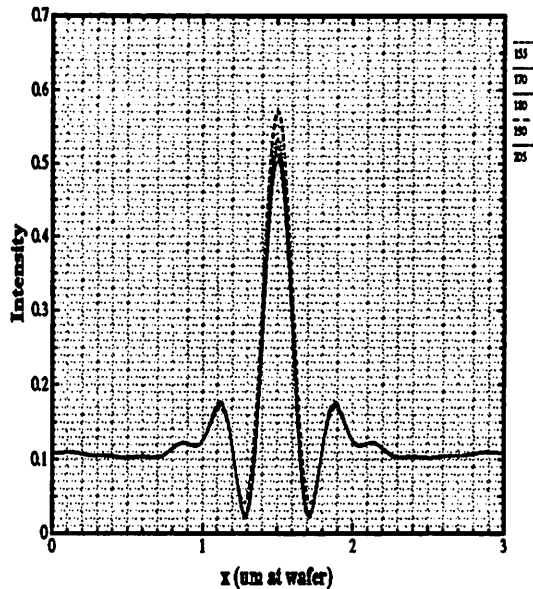


Figure 7.10 TEMPEST simulations show the same behavior as observed experimentally.

dimension, the peak intensity of the SPLAT image is only 23% higher than that of the TEMPEST image. This indicates that the phase interaction between the clear area and the leaky area in an attenuated PSM reduces the effect of glass edge scattering.

Although the peak intensities for the features with different phases vary by as much as 10% as the phase changes from 155° to 205° , the normalized images as shown in Figure 7.12 do not differ by too much except that the sidelobe and the background transmission become relatively more important as the glass etched depth increases. This increased relative importance of the sidelobe intensity is not important for in-focus printing. For out-of-focus printing, however, the slightly decreased contrast may cause the depth-of-focus (DOF) to degrade for higher phase masks.

A possible remedy to the problem of reduced peak intensity is to fabricate the attenuated PSM using the recessed leaky chrome (RLC) technique²⁰ as shown in Figure 7.13 where the structure of a normal leaky chrome (NLC) mask is also illustrated. The inverted configuration of the RLC mask was implemented in order to reduce the effect of electromagnetic scattering from the sidewalls of the etched glass openings. The efficacy of the RLC mask in reducing glass edge scattering is studied by examining the electric field in the vicinity of a glass edge for the two types of masks as shown in Figure 7.13. Incident radiation propagates from the top of the figures and

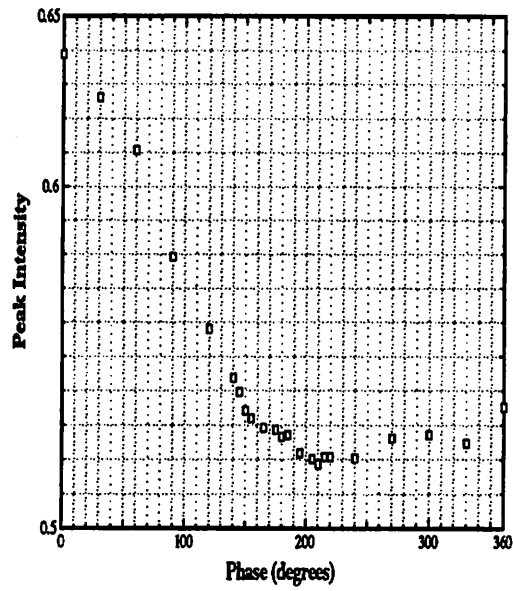


Figure 7.11 Peak intensity of a 0.25 μm opening (wafer dimension) in a binary chrome mask as a function of glass etched depth (phase) from TEMPEST. Deeper glass trenches result in lower peak intensities.

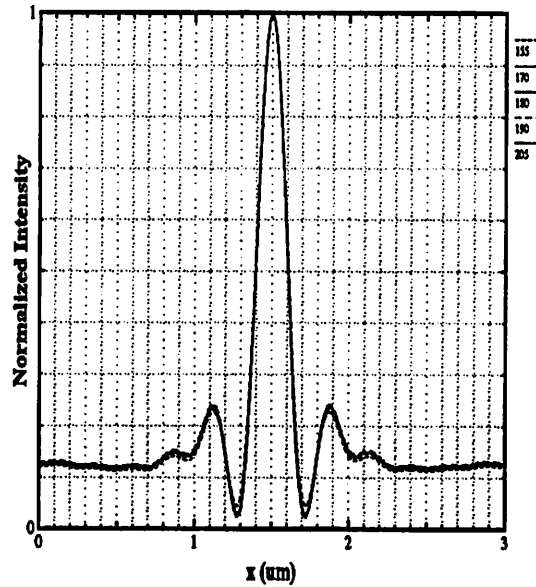


Figure 7.12 Normalized TEMPEST images of Figure 7.10 show that there is not much difference in image quality for the five different phases, other than the difference in peak intensity.

impinges upon the mask topography creating the transmitted field distribution at the lower part of the figures. For the NLC mask, Figure 7.13a shows that a region of low electric field is created in

the air adjacent to the glass edge. The reduction in peak intensity can be attributed to the formation of this shadow region. For the RLC mask, however, Figure 7.13b shows that the light tends to concentrate in the opening region and remain in the optically denser material (glass). Thus, the RLC mask is expected to alleviate the problem of transmission loss due to glass edge scattering.

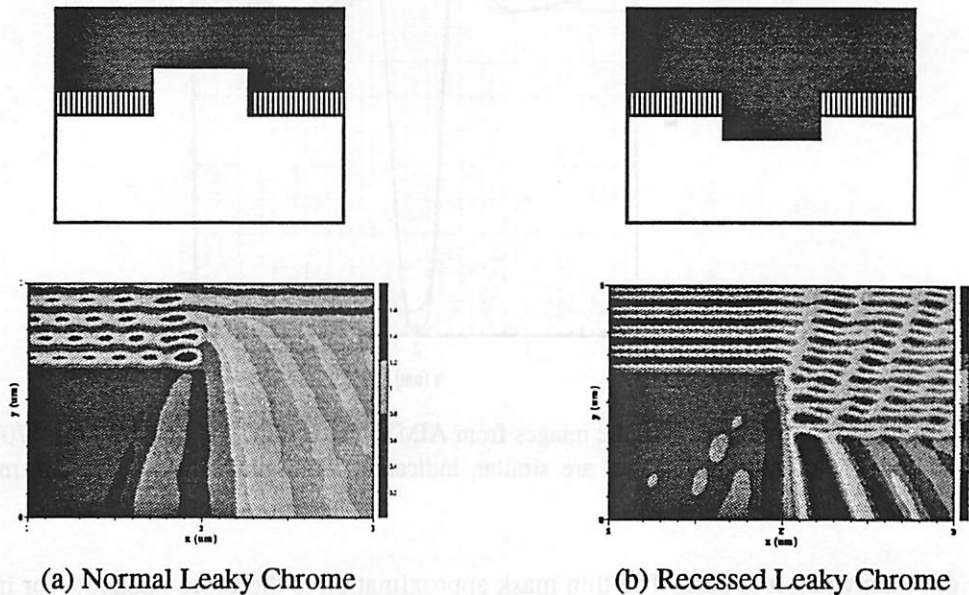


Figure 7.13 The RLC mask can be used to alleviate the problem of glass edge scattering in attenuated PSMs. (a) In the NLC mask, a region of low electric field is created by the glass edge which results in a loss in peak intensity. (b) In the RLC mask, the low electric field region does not exist because the field tends to remain in the optically denser material.

7.6.2.4 Isolated Line

For isolated line patterns, SPLAT simulation results show that a pure phase error of $\pm 25^\circ$ is again not significant in affecting the in-focus images. Contrary to the isolated space patterns, the in-focus images as measured by the AIMS tool and predicted by TEMPEST and SPLAT match closely with one another as shown in Figure 7.14. (The AIMS measured image has a higher minimum intensity which may be caused by flare in the measurement environment.) Thus, scattering from the glass edges does not play an important role in degrading the in-focus aerial images of isolated lines. This is because the relative importance of the scattered light is less when the mask background is

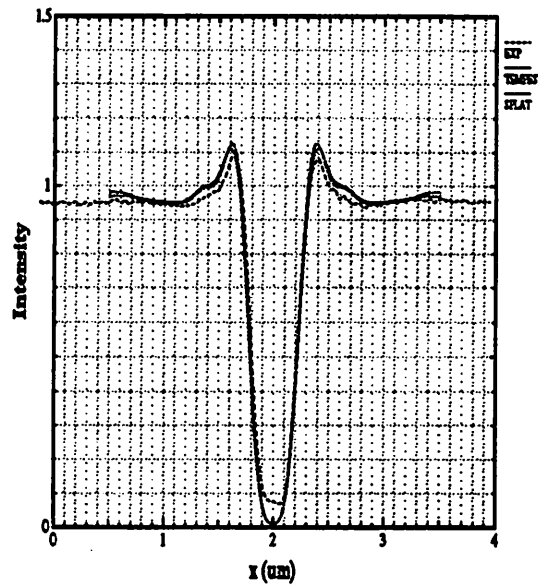


Figure 7.14 Comparison of the images from AIMS, TEMPEST, and SPLAT for a 170° $0.25 \mu\text{m}$ line. The three images are similar, indicating the applicability of the thin mask and scalar approximations.

bright than when it is dark. The thin mask approximation is therefore adequate for in-focus image prediction.

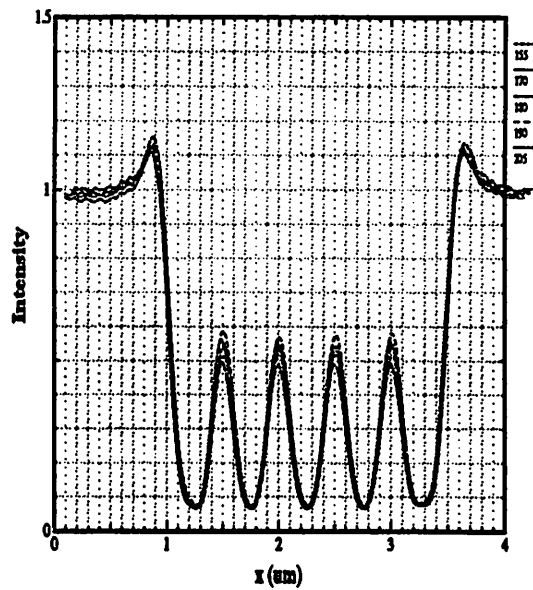


Figure 7.15 AIMS measured images of $0.25 \mu\text{m}$ linespace patterns of five different phases. Similar to the isolated space pattern, the peak intensity decreases with increasing phase.

7.6.2.5 Linespace Pattern

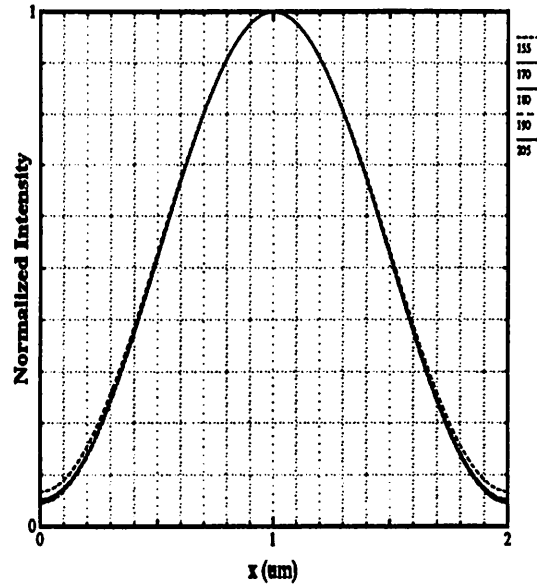


Figure 7.16 Normalized images of linespace patterns of Figure 7.15 from TEMPEST simulations show that there should not be much in-focus performance difference among the masks with different phases.

AIMS measured images for linespace patterns with the five different phases are shown in Figure 7.15. Similar to the behavior of isolated spaces, the mask with the lowest phase (155°) shows the highest peak intensity. The peak intensity decreases as the phase is increased, reaching a minimum for the 205° mask with a peak intensity which is about 15% lower than that of the 155° mask. However, this decrease in peak intensity may not be significant in adversely affecting the mask performance because the normalized images from TEMPEST simulation shown in Figure 7.16 are very similar. Furthermore, contrary to the isolated space pattern, this decrease in peak intensity with increasing phase may not cause significant degradation in the DOF because of the absence of sidelobes in the images.

7.6.2.6 Defocus Behavior

The images of a 180° space pattern from SPLAT simulations for different defocus levels are shown in Figure 7.17. The images show a behavior which is symmetric with respect to the in-

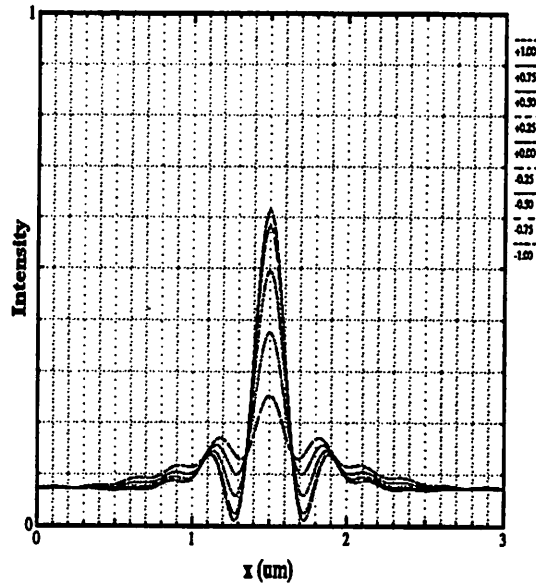


Figure 7.17 SPLAT images of a 180° space at defocus levels of 1.0, 0.75, 0.5, 0.25, 0.0, -0.25, -0.5, -0.75, and -1.00 μm . The defocus behavior is symmetric with respect to the in-focus image.

focus image, i.e., the image for $+x \mu\text{m}$ of defocus is the same as the image for $-x \mu\text{m}$ of defocus. However, such is not the case for the defocus images from TEMPEST simulations as shown in Figure 7.18. This asymmetry with respect to the zero defocus image can be attributed to glass edge scattering which causes an effective phase-shift of the opening¹⁹. In fact, a plot of the peak intensity as a function of defocus from AIMS measurements, and TEMPEST and SPLAT simulations in Figure 7.19 shows that although the SPLAT images show no focus shift, the TEMPEST images show a focus shift of about 0.1 μm . Determination of focus shift from AIMS images is difficult because of the difficulty in establishing a reference plane. Thus, the apparent focus shift of the AIMS images in Figure 7.19 cannot be interpreted as quantitatively correct. Nevertheless, AIMS measurements do indicate a focus shift which changes monotonically with the glass etched depth.

This focus shift can be explained by the path difference between light diffracted from the glass trench opening and the light leaking through the chromium layer. Since the diffracted light from the glass trench has an energy distribution which is almost uniform across the lens whereas the leaky field uses primarily the center part of the lens, the path difference or the focus shift is approximately $(d \cdot \text{NA}_m) / (2(\lambda/4))$ Rayleigh unit (RU), where d is the depth of the glass trench, NA_m

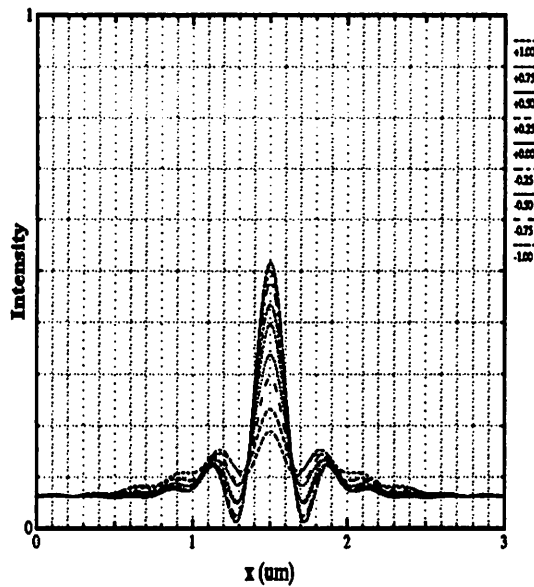


Figure 7.18 TEMPEST images of the same mask at the same defocus levels as Figure 7.17. The defocus behavior is asymmetric with respect to the in-focus image, indicating the influence of mask edge effects.

is the numerical aperture of the lens on the mask side, and $1 \text{ RU} = 0.5 \cdot (\lambda / \text{NA}^2)$. The number two is a heuristic factor which accounts for the fact that the diffracted field from the glass trench must be averaged over the entire lens. For the structure under consideration, $d = \lambda(\phi_{\text{glass}} / 360^\circ) / (n_{\text{glass}} - n_{\text{air}}) = 0.22 \mu\text{m}$, $\text{NA}_m = 0.125$, and the focus shift is calculated to be about 0.22 RU or 0.11 μm . This theoretical value agrees well with the observed focus shift from the TEMPEST curve in Figure 7.19. In practice, the value of this focus shift is different for different features across the field of exposure; and this would result in a loss of DOF. A similar phenomenon is observed for line patterns as well. Although SPLAT usually gives reasonable results near focus, it would need modifications such as a trench depth dependent phase correction factor to work well out-of-focus. The similarity between TEMPEST results and the AIMS data, together with their agreement with the above theoretical consideration, validates that TEMPEST is capable of modeling subtle effects in photolithography.

From the AIMS defocus images, the DOF of the masks with different phases are calculated via an E-D analysis with a 15% exposure latitude; and the results are shown in Figure 7.20. The DOF for both the isolated space (open squares) and the linespace patterns (shaded squares) are

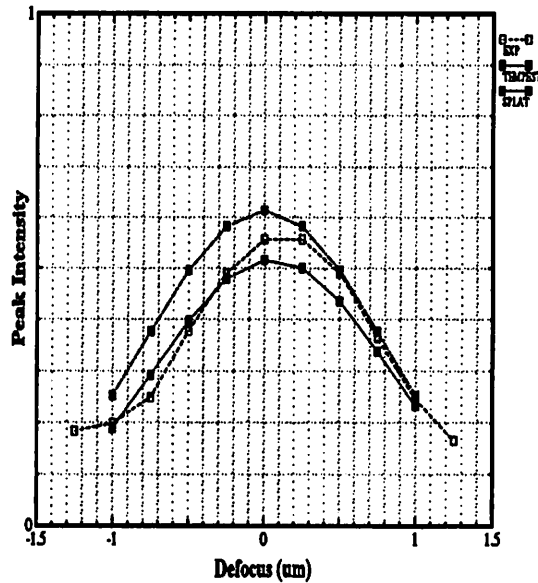


Figure 7.19 Peak intensity versus defocus for a 180° space from AIMS, TEMPEST and SPLAT. The TEMPEST data as well as AIMS measurements show a focus shift whereas the SPLAT data do not. This focus shift is related to the path difference between light diffracted from the glass trench opening and the light leaking through the chromium layer. The higher peak intensity shown by the AIMS measurements than the TEMPEST data is reasonable because of flare in the measurement environment.

larger than the line pattern (dark squares). For the 180° mask, the DOF for a 0.25 μm isolated space feature is 0.99 μm; for a 0.25/0.25 μm linespace feature it is 1.05 μm; and for a 0.25 μm isolated line it is only 0.52 μm. This poor DOF performance of isolated lines can be improved, however, by biasing. If a 1 μm line on the mask (corresponding to 0.25 μm in 4X reduction printing) is used to print 0.28 μm lines, the DOF is improved tremendously as shown by the dark diamonds in Figure 7.20. The DOF for a 180° line increases from 0.52 μm to 0.86 μm, representing a 50% increase in DOF with a 12% increase in the k_1 factor. This suggests that in the attenuated PSM technology, printing small isolated space and linespace patterns is more robust than isolated lines.

Reading the curves in Figure 7.20 individually, it is observed that for the isolated space pattern, the DOF generally decreases slowly as the phase increases. This is because the contrast of isolated space images decreases as the phase increases due to the reduction in peak intensity. As a result, the sidelobes become relatively more important when the image gets out of focus. The line pattern also shows a decrease in DOF as the glass trench becomes deeper. The linespace pattern

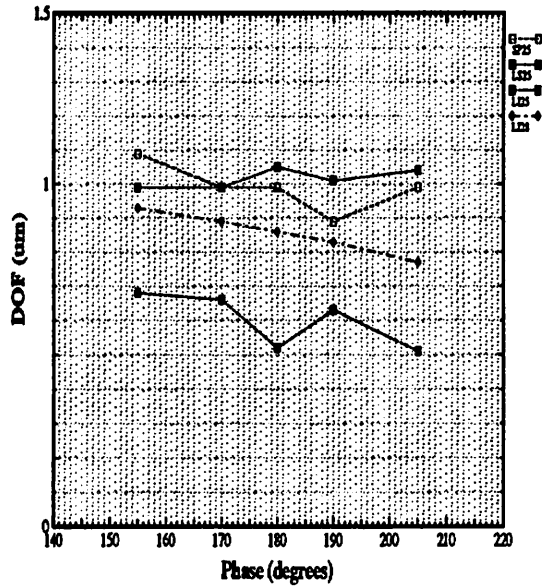


Figure 7.20 DOF as a function of phase. The DOF for space and linespace patterns are comparable; but the DOF for the line pattern is much smaller.

shows the least variation. This is due to the similarity among the normalized images in Figure 7.16 as well as the absence of sidelobes.

7.7 Chromeless PSMs

Chromeless PSMs are useful in printing dense lines and spaces. However, phase conflict and defect printability are major concerns for this technique. Methods to alleviate the phase conflict problem include introducing one 90° or two 60° phase steps between the 0° and 180° regions on the mask¹⁶. Despite these concerns, another issue of the chromeless technology is uneven linewidths for equal width patterns on the mask, similar to the situation of the alternating PSM technology discussed above. For chromeless masks, asymmetry can arise because glass sticking up from the mask substrate can attract radiation emanating from the bottom of the trench. Figure 7.21 shows the aerial images created by two masks with equal 0° and 180° widths (intended to produce a $0.5 \mu\text{m}$ pitch pattern on a wafer) on two different optical projection printing systems: System A and System B. SPLAT predicts a balanced image in both cases but this is not correct. For TEMPEST, system B gives equal peak heights at the 0° and 180° regions. However, system A does not. The peak

intensity corresponding to the 180° region (to the side in the figure) is lower than that corresponding to the 0° region (in the middle of the figure). Thus, in order to obtain equal linewidths, a system dependent bias to the mask must be applied.

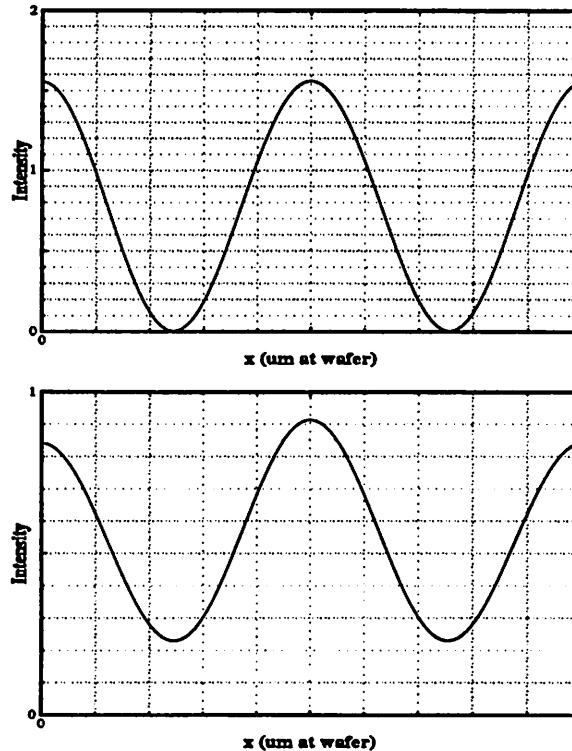


Figure 7.21 Optical image profiles created by chromeless masks for system B (above) and system A (below). System B shows symmetry between the 0° and the 180° regions; but system A does not.

The imbalance in peak intensities in system A arises because the small but non-vanishing zeroth and second diffracted orders becomes more important at small k_1 values and large σ . Since $k_1=0.35$ for system A, the collection lens captures only a fraction of the energy in the ± 1 diffraction harmonics. As a result, the energy associated with the zeroth and the second diffraction harmonics are relatively more important. In system B, however, the k_1 value of 0.5 is high enough and σ low enough so that the collection lens captures all the energy of the ± 1 harmonics, and the importance of the zeroth and second order harmonics remains negligible compared to the ± 1 beam interaction.

Another interesting phenomenon associated with chromeless mask repair is the difference between a 360° trench and a 360° protrusion. A phase defect is normally repaired by removing

glass at the defect position to attain a 360° trench. Figure 7.22 shows the images created by System B when such a methodology is employed for repairing defects of different sizes. The $2.0\ \mu\text{m}$ wide trench (a large defect) shows that a single 0° to 360° transition produces a dip to 80% of the clear field value. As the trench width decreases, the two glass edges interact to double the intensity decrease to 40%, corresponding to a dip going as low as 60% of the clear field value. This maximum dip occurs for a $0.25\ \mu\text{m}$ wide trench. As the trench size decreases from $0.25\ \mu\text{m}$, the dip becomes less severe as the trench becomes more difficult to resolve. The two curves marked by diamonds in Figure 7.23 show this simple behavior. The percentage intensity decrease is the most severe when the trench width is about one freespace wavelength. The severity of the effect decreases monotonically to both sides, reaching zero for very small defects and reaching the effect of a single edge for very large defects.

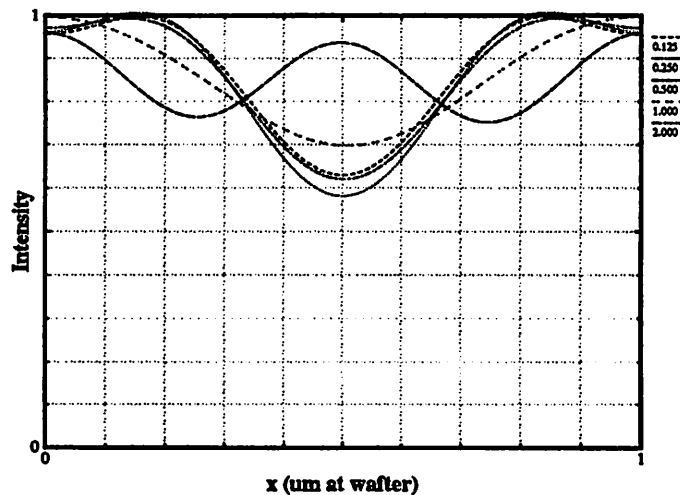


Figure 7.22 Images of 360° phase-shifter trenches of 2.00 , 1.00 , 0.50 , 0.25 and $0.125\ \mu\text{m}$ wide on chromeless phase-shift masks for the TM polarization.

During the course of phase defect repair, however, small downward pointing glass protrusions or dielectric ridges may be left behind. Assuming that the protrusions have 360° phase and vertical edges, they can produce decrease in the intensity of as much as 80% causing the image to dip to as low as 20% of the clear field value as shown in the two curves marked by squares in Figure 7.23. This region of sharp decrease occurs for both polarizations and shows an oscillatory behavior with respect to the width of the protrusion, indicating that a resonant phenomenon may be

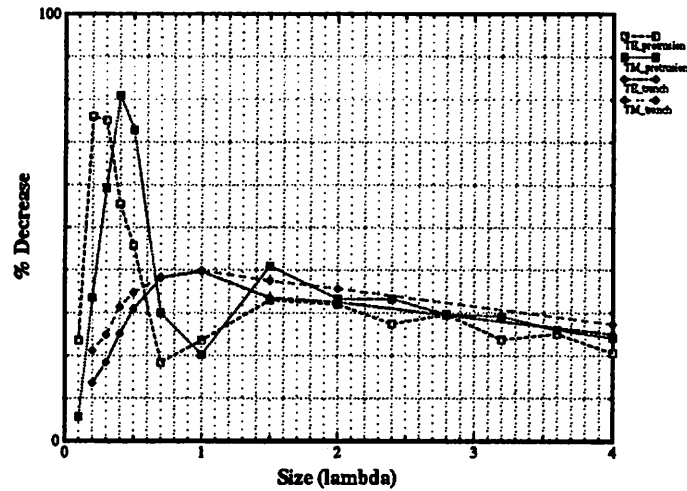


Figure 7.23 Percentage intensity decrease as a function of the width of the 360° trench (diamond marked) and protrusion (square marked) for the TE and TM polarizations. The oscillatory behavior associated with the protrusion suggests a resonance within the protrusion.

occurring within the protrusion. (Such a phenomenon does not occur if the defect is a trench etched into the glass substrate as discussed above.) If the resonance is due to reflection between the glass edges, the full width at half maximum (FWHM) of the resonance, i.e., the range of protrusion widths which produce severe drop in the intensity, should be about $0.5\lambda_{\text{material}}$. The first resonances in Figure 7.23 for both polarizations show widths of about $0.3\lambda_0$, which is about $0.5\lambda_{\text{glass}}$, agreeing with the above prediction. The difference in the resonance location (protrusion width which gives the most severe drop in intensity) between the two polarizations can be attributed to the difference in reflection coefficients for the two polarizations.

To test if the observed behavior is a function of the mask structure or the optical system parameters, the same structure was simulated with the optical System B, except that the resolution in this case is halved by reducing the numerical aperture from 0.5 to 0.25. Figure 7.24 shows that the worst intensity decrease in this system is 50%, or 30% less than the previous system owing to lower resolution. However, the width of the protrusion corresponding to the worst case is the same for both systems and does not scale with resolution, indicating that the resonance is a property of the mask structure itself. Thus, the optical system parameters such as the numerical aperture and the partial coherent factor were found to affect the degree of the intensity decrease but not the basic

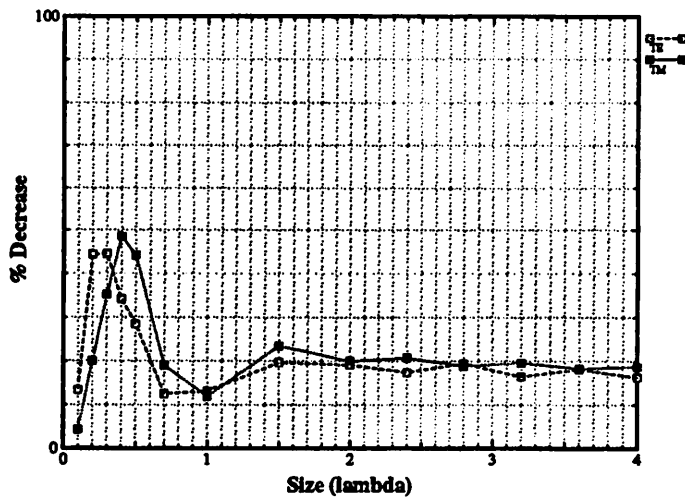


Figure 7.24 Percentage intensity decrease as a function of protrusion width for a system with an NA of 0.25. The percentage drop for this system is less than the previous system with an NA of 0.50, but the locations of the peaks and valleys are identical.

behavior itself. This structural effect can even be seen in oblique incidence. Figure 7.25 shows the instantaneous magnetic field for a 0.125 μm wide glass protrusion for an incident angle of 3.6° in the TM polarization ($\lambda=0.248 \mu\text{m}$). The high peak values in the vicinity of the dielectric protrusion again suggest a resonant phenomenon.

The difference in behavior between a dielectric ridge and a trench can also be seen experimentally as shown in Figure 7.26. The feature on the left corresponds to the printed image of a glass trench and the feature on the right corresponds that of a protrusion. The effect of a protrusion is bigger than a trench as can be seen by the darker (deeper) line in the SEM picture.

7.8 Conclusions

Effects of phase-shifting mask edge in projection printing for four types of phase-shifting masks were assessed using rigorous electromagnetic simulation on four different optical systems and validated with experimental data. Important effects of glass edge scattering of light rays through the masks were found, resulting in images which are 10 to 30 per cent different from the ideal images predicted by scalar and thin mask models in simulators such as SPLAT. The etched glass edges were found to scatter light and lead to a lowering in peak intensity. For alternating masks, edge scattering can be remedied by reducing the opening dimension by $0.021 \lambda/\text{NA}$ per

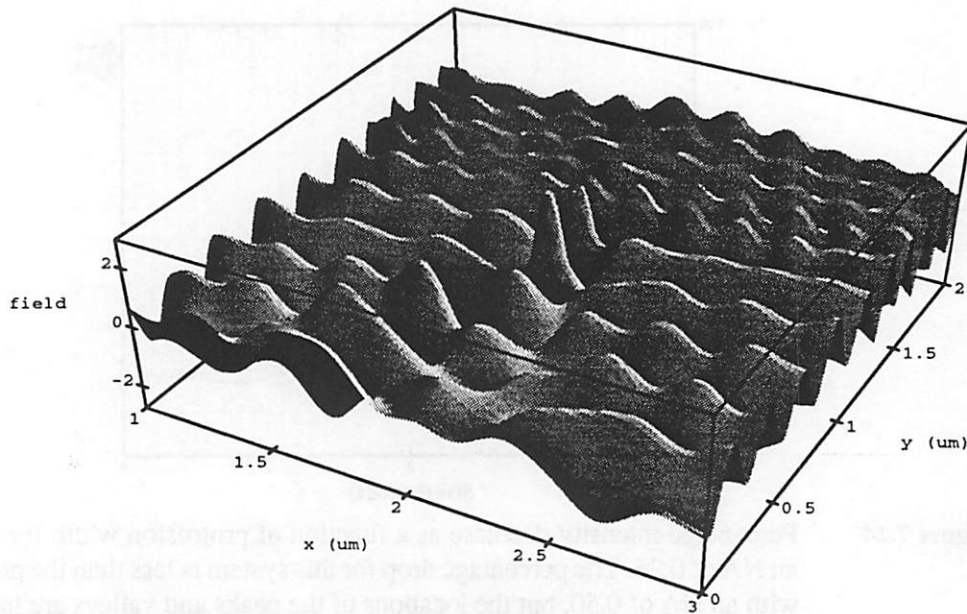


Figure 7.25 Instantaneous magnetic field for a $0.125\ \mu\text{m}$ wide glass protrusion for oblique incidence (TM). The field shows high peak within the protrusion, suggesting a resonant phenomenon.

edge for feature size ranging from 0.3 to $0.7\ \lambda/\text{NA}$. To model such an effect in SPLAT to first order, Figure 7.4 can be used as a design graph to determine the amount of bias needed.

For rim type PSMs, edge to edge interaction is shown to be insignificant based on an approach analogous to a two-level experimental design. No direct electromagnetic interaction between chromium edges and shifter edges was found. Hence, optimization of the rim size and the middle size is not complicated by the second order effect of the product of the rim and middle dimensions. The rim dimension can thus be designed solely on the basis of the sidelobe level and peak intensity. For attenuated PSMs, a lower level of transmission of the partially transmitting layer is recommended for smaller features based on consideration of image contrast through focus. Topographies on attenuated PSMs also have important effects on the image quality and defocus behavior of isolated space, isolated line, and linespace patterns. These edge effects cause a loss in peak intensity and hence a possible reduction in throughput. Remedy to this problem with the recessed leaky chrome mask is promising. The trench depth also produces a focus shift which is slightly pattern dependent. Improvements may be made if a suitable attenuating material is found

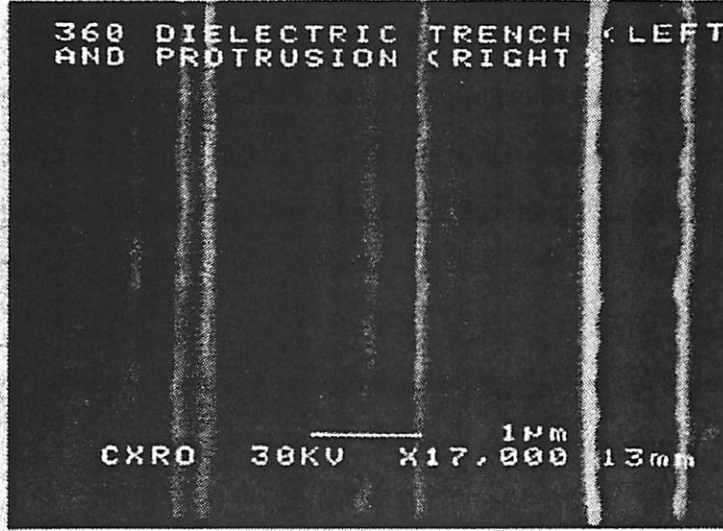


Figure 7.26 SEM picture of photoresist lines produced by a 1 μm dielectric ridge (right) and a 1 μm trench (left). The effect of a protrusion is bigger than a trench as is indicated by the darker (deeper) line in the picture. Exposure is done on a 4X deep-UV stepper with a numerical aperture of 0.6 and a partial coherence factor of 0.5. The photoresist is negative tone SNR-248. (Photoresist picture courtesy of Marco Zuniga at the University of California, Berkeley.)

such that little height difference occurs between the open and attenuated regions. For chromeless PSMs, optical system parameters can affect the peak intensity balance between the 0° and the 180° regions for small features through the increase in relative importance of the small but non-negligible even order diffracted harmonics.

In any PSM technology, small 360° glass protrusions may produce a drastic drop in the intensity. This effect was first predicted by TEMPEST and then observed experimentally. The qualitative behavior of this resonance is dependent only on the mask structure, and is independent of the optical system parameters. The effect is expected to be smaller for “real-life” protrusion defects since the rough and non-vertical edges may inhibit the resonance which exists for a vertical edge protrusion.

Through the study of these different PSM techniques, in advance predictions by TEMPEST have shown quantitative agreement with experimental data taken on different systems. TEMPEST predictions of focus shift and the effects of glass edge scattering in attenuated PSMs were

confirmed by AIMS measurements. The difference in behavior between a dielectric ridge and a glass trench in the chromeless PSM technology predicted by TEMPEST was also supported by SEM pictures of photoresist lines. For the alternating PSM technique, variations of the optical image due to subtle changes in the mask are successfully predicted by TEMPEST and validated by photoresist exposure studies. TEMPEST is thus a useful and accurate electromagnetic modeling program for understanding difficult and complicated issues in photolithography.

Chapter 8

Three-dimensional Applications: Mask Edge Effects and Reflective Notching

8.1 Introduction

The ability to analyze three-dimensional structures is very important in photolithography as it allows many complicated issues to be examined. Effects in two-dimensional features may be exaggerated or diminished in a three-dimensional structure. For example, results from two-dimensional rigorous simulation of a $0.5 \lambda/NA$ wide isolated space feature on a binary mask show polarization effects of 3% and a transmission loss of 10% as the light passes through the opening¹⁰⁰. These effects are expected to be larger in three-dimensional mask features such as contact hole patterns. Another interesting problem is that of the printability of a 360° phase quartz bump defect. For a 360° phase ridge, the previous chapter indicates the existence of resonance within the dielectric ridge which can cause a 70% drop in the intensity. The corresponding three-dimensional bump defect is not expected to show such a drastic effect because such a structure does not support a waveguide mode. Reflective notching is another important three-dimensional issue as non-planar topography on the wafer can cause undesired exposure in the photoresist and a change in the critical dimension of the feature being formed.

8.2 Simulation Context

A typical TEMPEST simulation described in this chapter uses a simulation domain of $4 \mu\text{m}$ by $4 \mu\text{m}$ by $1 \mu\text{m}$ (length by width by height). The domain is divided into a cubic grid of 256 by 256 by 64 simulation nodes. This translates to about one simulation node per 16 nm. The incident radiation is assumed to be a normally incident plane wave with the electric field polarized in the x-direction (the length direction). Steady-state is reached after about 30-50 wave cycles, which takes about 10 minutes on a 32-node partition on the CM-5. (Each node on the CM-5 consists of 32 megabytes of memory, and there are a total of 512 nodes on the CM-5 at the National Center for Supercomputing Applications (NCSA) in Illinois. A larger problem can be solved by using more processor nodes.) The calculated diffraction harmonics are then transferred to SPLAT for image

synthesis. Two-dimensional image calculation using SPLAT generally takes less than one minute on a workstation, although longer computation time may be needed for larger problems.

8.3 Polarization Effects and Transmission loss in 1X Contact Holes

Evidence of the importance of polarization effects and transmission loss was shown to be important for 1X deep-UV projection printing¹⁰⁰. These effects are expected to be more severe for mask patterns such as contact holes and elbows because of increased interactions between the electromagnetic fields and the chromium absorption layer. In this study, square openings of sizes ranging from 0.1 μm to 1.0 μm in length on each side are examined for transmission loss and polarization effects. The context chosen to explore these effects is that of 1X deep-UV (248 nm) projection printing with a numerical aperture (NA) of 0.5 and a partial coherence factor (σ) of 0.4. Thus $1 \lambda/NA$ is approximately equal to 0.5 μm . The absorption layer of the mask is chromium with a refractive index of (2.5, -j2.0) and a thickness of 80 nm. The glass substrate has a refractive index of (1.5, j0.0).

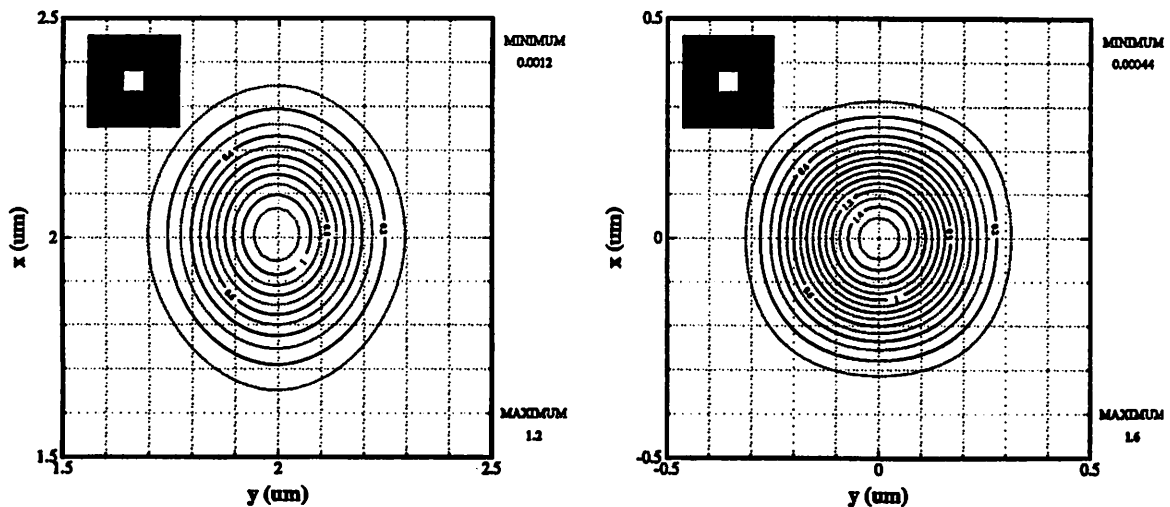


Figure 8.1 Images of a 0.5 μm by 0.5 μm ($1 \lambda/NA$ by $1 \lambda/NA$) opening predicted by TEMPEST (left) and SPLAT (right) simulations. The SPLAT image shows a four-fold symmetry whereas the TEMPEST image shows only a two-fold symmetry, indicating polarization effects.

The images of a 0.5 μm by 0.5 μm ($1 \lambda/NA$ by $1 \lambda/NA$) opening predicted by TEMPEST and SPLAT (thin mask and scalar approximations) simulations are shown in Figure 8.1. Notice in

the figure that the SPLAT image shows a peak intensity which is 25% higher than that of the TEMPEST image. This loss in peak intensity is also observed for space patterns¹⁰⁰, and is apparently due to a combination of propagation through a small aperture and energy dissipation in the chrome due to its finite thickness. In fact, a plot of the peak intensity as a function of opening size for TEMPEST and SPLAT simulations shown in Figure 8.2 indicates that the SPLAT image shows higher peak intensity for opening sizes of less than $1 \lambda/NA$. The SPLAT image can give a peak intensity which is almost 2X higher than that predicted by TEMPEST for the case of a $0.4 \mu\text{m}$ by $0.4 \mu\text{m}$ ($0.8 \lambda/NA \times 0.8 \lambda/NA$) opening. The difference in the peak intensities between SPLAT and TEMPEST is greater for contact hole structures than for a space pattern. An exact relationship of transmission loss between an open space and a square contact hole is complicated. However, for feature sizes smaller than $1 \lambda/NA$, transmission loss for a square contact hole is about three times that of an isolated space. This increase is due to the simultaneous presence of the north/south and east/west edge effects in a contact hole structure.

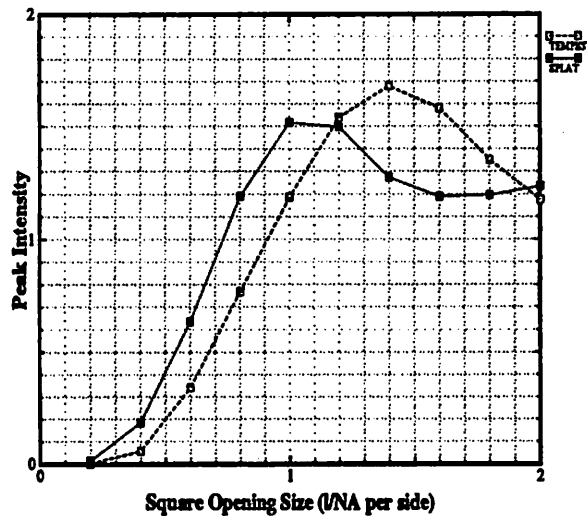


Figure 8.2 Peak intensity of square openings as a function of size. For openings smaller than $1 \lambda/NA$, SPLAT images show higher peak intensity than the TEMPEST images.

Since the transmission loss of a square contact hole is about three times that of an isolated space, the effects in a contact hole cannot be approximated by summing the effects of two perpendicular space openings. Non-linear effects are present. These effects can also be ascertained from Figure 8.2 as the transmission loss is not constant over any range of the feature size, implying

that a different bias must be used for features of different sizes. This is not a serious restriction in IC fabrication, however, because all the contact holes usually have the same dimensions.

Another interesting feature in Figure 8.1 is that the image predicted by SPLAT shows a four-fold symmetry (with respect to the x-axis, the y-axis, the $x = y$ line and the $x = -y$ line) whereas the TEMPEST image exhibits only a two-fold symmetry (with respect to the x-axis and the y-axis). Since the four-fold symmetry shown by the SPLAT image is also present in the square mask pattern, lack of symmetry with respect to the $x = y$ line and the $x = -y$ line in the TEMPEST image indicates that the electromagnetic fields interact with the metal chromium differently depending on the relative orientation between the incident polarization and the metal surface. In fact, the TEMPEST image in Figure 8.1 shows an elliptical shape which is elongated in the x-direction when the incident electric field is polarized in the x-direction. The eccentricity (defined as the ratio of the image width in the y-direction to the width in the x-direction) as a function of the opening size is shown as the open squares in Figure 8.3. In the absence of polarization effects, a square contact with $k_1=0.8$ prints slightly eccentric by 6% as shown by the SPLAT image in Figure 8.1. The polarization effect is about 3 times larger as the eccentricity reaches a maximum of 1.17 when the opening size is $1 \lambda/NA$. This suggests that there is a critical size at which polarization effects are the most important. For sizes smaller than this critical size, polarization effects are relatively less important because of the difficulty in transmission through a small opening, and the contact hole becomes more difficult to resolve. For contact holes larger than this critical size, the relative importance of the metal edges decreases as the clear area increases.

To test if this critical size is a function of the mask structure or of the optical system parameters, the same contact holes were simulated with another optical system with an NA of 0.35. This system produces features which are 1.5 times larger than the former system. The results are shown as the open diamonds in Figure 8.3. Comparing the two curves in Figure 8.3, the critical size is the same for both systems at about $1 \lambda/NA$, although the $NA=0.5$ system shows a higher degree of eccentricity. Thus, the critical size is dependent on the optical system parameters. For the $NA=0.5$ system, the critical size is $0.5 \mu\text{m} \times 0.5 \mu\text{m}$ whereas for the $NA=0.35$ system, the critical size is $0.7 \mu\text{m} \times 0.7 \mu\text{m}$.

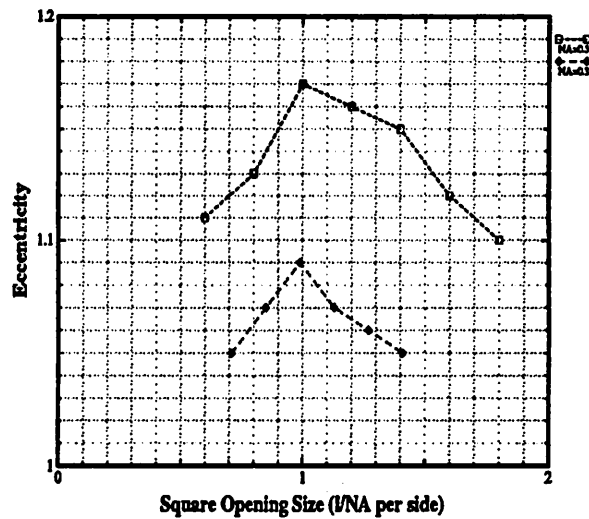


Figure 8.3 Eccentricity as a measure of lack of symmetry. The value should be one in the absence of any polarization effects. Eccentricity is system dependent as it peaks at $1 \lambda/NA$ for two optical systems.

The elliptical shape of the TEMPEST images can be partly explained by the electromagnetic boundary conditions on a metal surface imposed by Maxwell's equations. On the surface of a good conductor, the parallel electric field is almost zero whereas the perpendicular electric field is nonzero. Thus, when the incident electric field is polarized in the x-direction, the electric field is almost zero at the metal surfaces parallel to the x-axis. The effective length of the mask in the y-dimension is therefore smaller than the effective length in the x-dimension, leading to the elliptical shape of the images.

The dependence of the critical size on the optical system parameters suggests that besides purely electromagnetic considerations, there is an interplay between electromagnetic scattering on the mask and the optical system which creates the mask image. Since the image eccentricity arises because of the metallic layer on the mask, the most important optical system parameter should be the cone angle on the mask side. The larger the cone angle, the more eccentric the image is as suggested by Figure 8.3. Thus, there should be little eccentricity in square contact hole images for reduction masks as the cone angle on the mask side is small.

This polarization effect is expected to be more pronounced for rectangular patterns because a narrow slit may transmit different amounts of energy depending on the incident polarization.

Figure 8.4 shows the TEMPEST images of a $0.4\ \mu\text{m}$ by $0.5\ \mu\text{m}$ mask and a $0.5\ \mu\text{m}$ by $0.4\ \mu\text{m}$ mask.

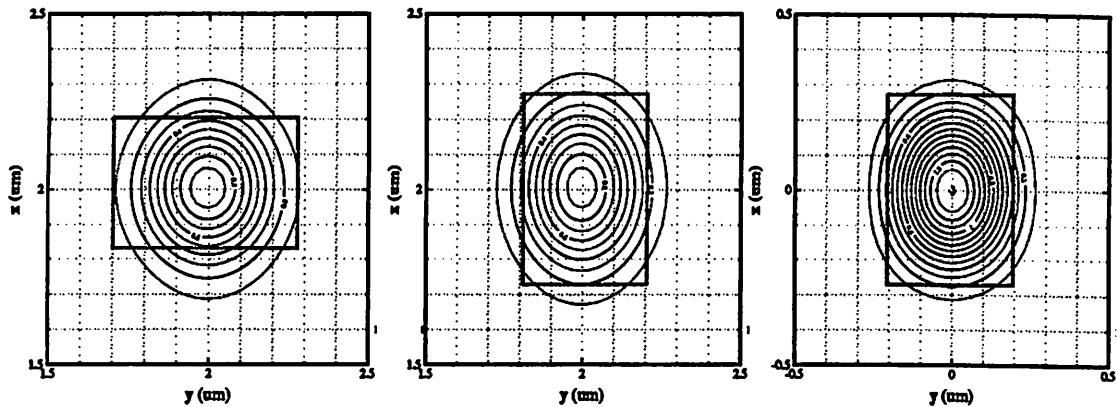


Figure 8.4 Images of a $0.4\ \mu\text{m}$ by $0.5\ \mu\text{m}$ opening by TEMPEST (left), a $0.5\ \mu\text{m}$ by $0.4\ \mu\text{m}$ opening by TEMPEST (middle), and a $0.5\ \mu\text{m}$ by $0.4\ \mu\text{m}$ opening by SPLAT (right). Polarization effects make the effective y dimension of the opening smaller in TEMPEST simulations.

It can be seen from the figure that for the 0.4 by 0.5 mask, the image is longer in the x -direction than in the y -direction although the mask opening is longer in the y -direction. This indicates that polarization effects are even stronger than the orientation of the rectangular mask feature. For the 0.5 by 0.4 mask, polarization shortening of the y dimension causes the structure to appear more elliptical as indicated by the oval shape of the image. The image predicted by SPLAT shown in the same figure displays a less elliptical image, indicating the effects of polarization in the TEMPEST images.

Since the effective length of the opening in the y -direction is smaller when polarization effects are considered, the eccentricity of the images predicted by TEMPEST is smaller than the eccentricity of the images predicted by SPLAT. Table 8.1 shows the eccentricity of the images predicted by TEMPEST and SPLAT for different sized rectangular openings. The eccentricity is determined by the x and y extent of the image at the 30% intensity level (with respect to clear field). The difference between the eccentricities can be as much as 31% for an opening of $0.5\ \mu\text{m}$ by $0.6\ \mu\text{m}$. Notice also that for certain structures, the eccentricity of the TEMPEST images may be less than 1 while the mask aspect ratio is greater than 1. This effect may complicate the design of masks as different bias values are needed for the two different directions if polarized illumination is used.

From Table 8.1, a bias of about 0.05 μm in the y-direction is needed to correct for polarization effects assuming that no bias is applied to the x-direction. In most projection systems, however, the use of unpolarized light sources would reduce almost all asymmetries due to polarization effects, but it would still be important to bias the contact hole according to Figure 8.2 to increase the peak intensity of the image.

Mask Size (μm by μm)	Mask Aspect Ratio	Eccentricity (TEMPEST)	Eccentricity (SPLAT)	Percentage Difference
0.2 x 0.5	2.50	N/A	1.66	N/A
0.4 x 0.5	1.25	0.97	1.15	-18.6%
0.6 x 0.5	0.83	0.75	0.84	-12.0%
0.8 x 0.5	0.63	0.57	0.58	-1.8%
1.0 x 0.5	0.50	0.45	0.45	0.0%
0.5 x 0.2	0.40	N/A	0.60	N/A
0.5 x 0.4	0.80	0.85	0.87	-2.4%
0.5 x 0.6	1.25	0.91	1.19	-30.8%
0.5 x 0.8	1.60	1.32	1.72	-30.3%
0.5 x 1.0	2.00	1.88	2.24	-19.1%

Table 8.1 Eccentricity of the TEMPEST and SPLAT images for mask openings of different dimensions. For any contact hole, the eccentricity of the TEMPEST image is less than the SPLAT image. The difference can be as large as 31% for a 0.5 μm by 0.6 μm opening.

All the contact holes considered so far are ideal. Contact holes on masks which are used in photolithography have non-idealities such as rounded corners and defects. These non-idealities can also be examined with TEMPEST. For example, the image of a 0.5 μm by 0.5 μm contact hole with its corners obscured is shown in Figure 8.5 together with the image of an ideal contact hole. The obscurities at the corners are chromium with the same thickness as the opaque region. The cross-sections of each obscurity is a square of size 50 nm in length on each side. There is little qualitatively difference between the two images, although the ideal contact hole gives a slightly higher peak intensity and a slightly larger image.

8.4 Defect Printability in Chromeless Phase-Shifting Masks

It was shown that a 360° glass ridge in a chromeless PSM produces resonances that may cause an intensity drop of 70% to 30% of the clear field value¹⁰¹. Such a drastic drop in the intensity

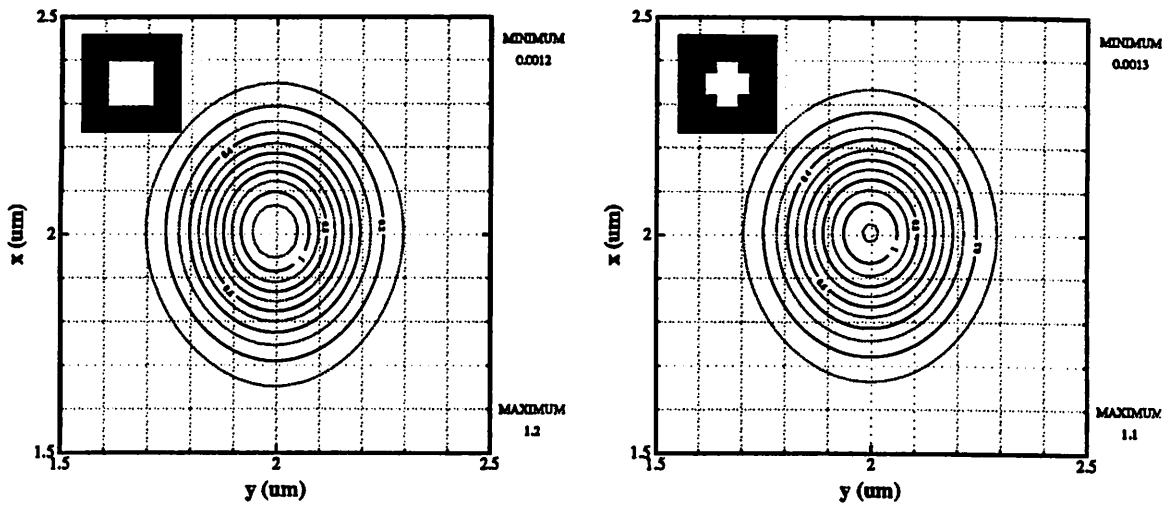


Figure 8.5 The images of an ideal contact hole (left) and a contact hole with obscurities at the corners (right) show little qualitative difference in the aerial images. The ideal contact hole shows a slightly higher peak intensity.

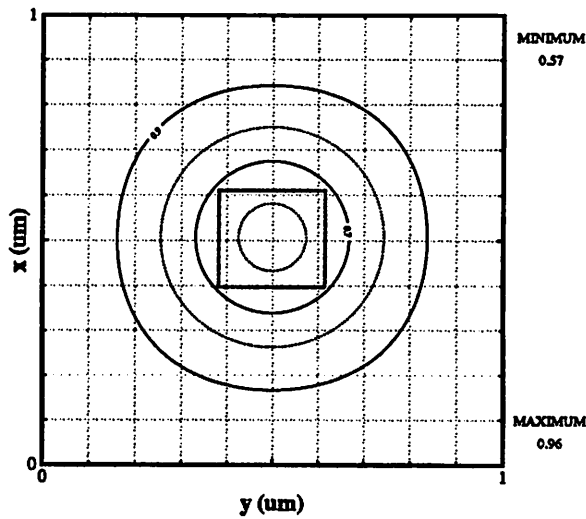


Figure 8.6 Image of a $0.9\ \mu\text{m}$ by $0.9\ \mu\text{m}$ 360° phase bump defect. The image attains a minimum in the middle of the defect. This is typical of the behavior of such defects.

level was attributed to wave-guiding effects of the dielectric protrusion. It is thus interesting to investigate the printability of 360° phase quartz bump defects. The context chosen to explore this phenomenon is that of 4X deep-UV projection printing with an NA of 0.5 and a σ of 0.4. The point defects all have vertical glass edges which are 2λ ($0.496\ \mu\text{m}$) long in the vertical dimension in order

to create a phase of 360° with the refractive index of glass assumed to be $(1.5, j0.0)$. In the horizontal dimensions, the protrusion has a square surface which varies in size from $0.1 \mu\text{m}$ to $1.0 \mu\text{m}$ in length on each side on the mask.

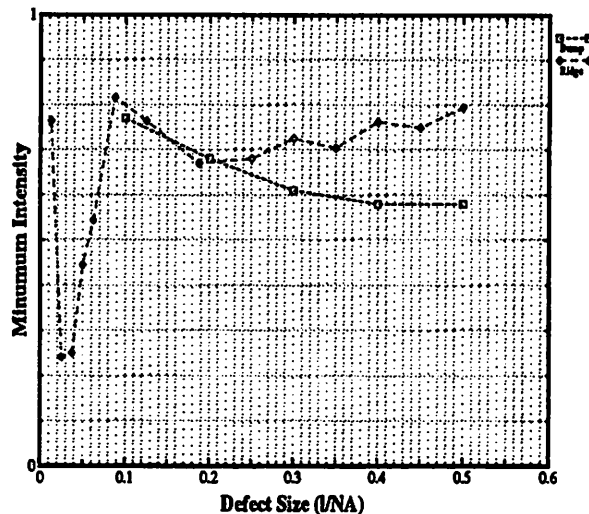


Figure 8.7 Minimum intensity as a function of defect size. The bump defect shows a smooth behavior whereas the ridge defect shows an oscillatory behavior.

A typical optical image profile of such a defect is shown in Figure 8.6 for a defect size of $0.9 \mu\text{m}$ by $0.9 \mu\text{m}$. Notice that the image shows a four-fold symmetry, indicating that polarization effects are not important. This is also the case for a 360° phase glass ridge or glass trench¹⁰¹. The 0° - 360° transition causes an intensity drop which is the most severe in the middle of the defect; and this point of lowest intensity can be used to characterize the impact of the defect. Figure 8.7 plots this minimum intensity as a function of defect size. The impact of the defect reaches a maximum for a defect of size $1 \mu\text{m}$ by $1 \mu\text{m}$ ($0.5 \lambda/NA$ by $0.5 \lambda/NA$), where the intensity is reduced by 40%. The effect of the defect decreases monotonically for larger and smaller sizes. This behavior is in contrast to a glass ridge which shows the oscillating behavior (discussed in the previous chapter) as shown by the open diamonds in Figure 8.7. This result indicates that a waveguide mode is not set up within the glass protrusion. Quartz bump defects of 360° phase are thus not problematic when the dose to clear is below 55% of the clear field exposure value.

8.5 Reflective Notching

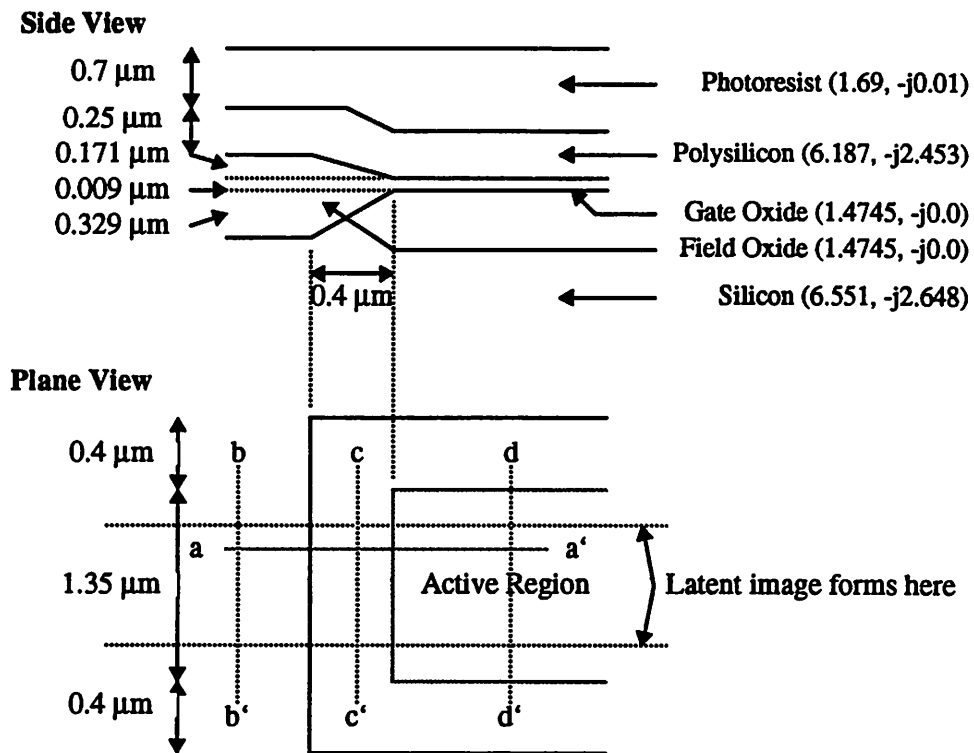


Figure 8.8 Printing of a polysilicon gate. The 0.25 μm thick conformal polysilicon is coated on the oxide; it passes from the field oxide through the bird's beak onto the active region.

Besides its applications in the study of mask problems, three-dimensional TEMPEST is also useful in the study of formation of latent images in photoresist over non-planar topography. This is especially important in the patterning of the polysilicon gate. Topography on the wafer may cause uneven exposure and hence non-uniform critical dimension of the polysilicon gate as it transverses over the active region and field oxide. As an example, consider the printing of a polysilicon line as shown in Figure 8.8. A conformal layer of polysilicon with a thickness of 0.25 μm is coated on the oxide. The polysilicon runs from the field oxide ($\sim 0.5 \mu\text{m}$ thick) through the bird's beak (lateral dimension of 0.4 μm) onto the active region with a gate oxide thickness of 90 \AA . A latent image is formed on the planar photoresist layer with Dill's ABC parameters¹⁵ given as (0.95, 0.083, 0.016). The image is formed by SPLAT simulation of a 1.75 μm wide opening on a

5X reduction mask at a wavelength of $0.365 \mu\text{m}$. A total dose of 100 mJ is delivered. Dynamic bleaching of the photoresist is modeled by dividing the total dose into five steps.

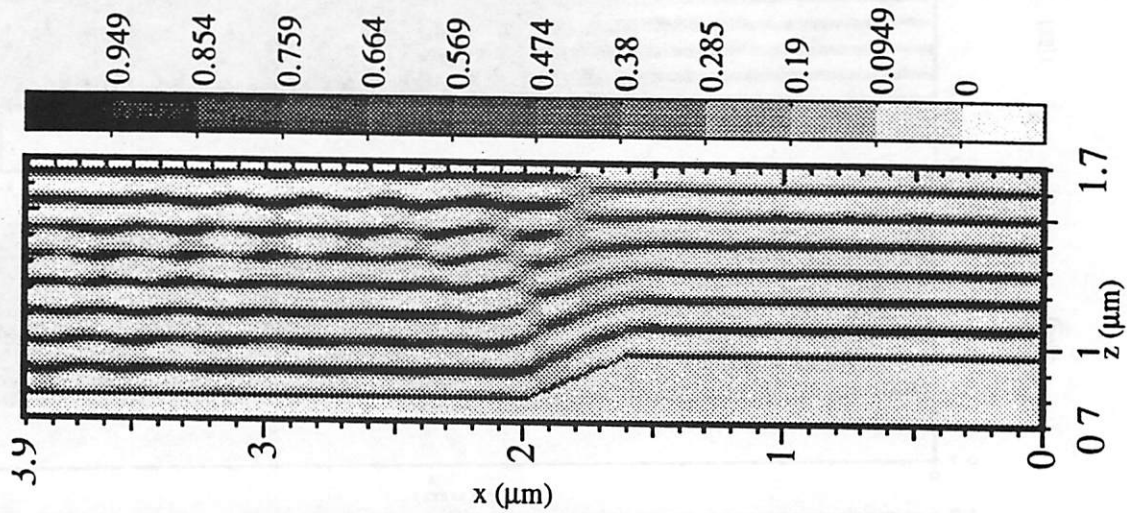


Figure 8.9 PAC concentration of a vertical plane along the line aa' in Figure 8.8. Far away from the bird's beak, the latent image shows the effects of standing waves. At the polysilicon step, the exposure energy is re-directed by the topography, resulting in a region of low exposure.

Figure 8.9 shows the latent image within the photoresist (PAC concentration) of a vertical plane along the line aa' in Figure 8.8. Far away from the step, the latent image shows the effects of standing waves caused by the high reflectance of the polysilicon layer. At the bird's beak, the exposure energy is re-directed by the polysilicon topography, resulting in a region of low exposure. The effect of the step can also be seen in Figure 8.10, in which the PAC concentration of vertical planes along bb', cc', and dd' are shown. The picture on the top (bb') shows the standing wave within the photoresist in the field oxide region. The picture on the bottom (dd') shows the PAC concentration in the photoresist in the active region. These latent images show wider critical dimensions than the one in the middle picture (cc') in which the PAC concentration of a vertical plane at the location of the bird's beak is plotted. This reduction of polysilicon critical dimension due to the slope of the bird's beak has also been observed experimentally³⁸.

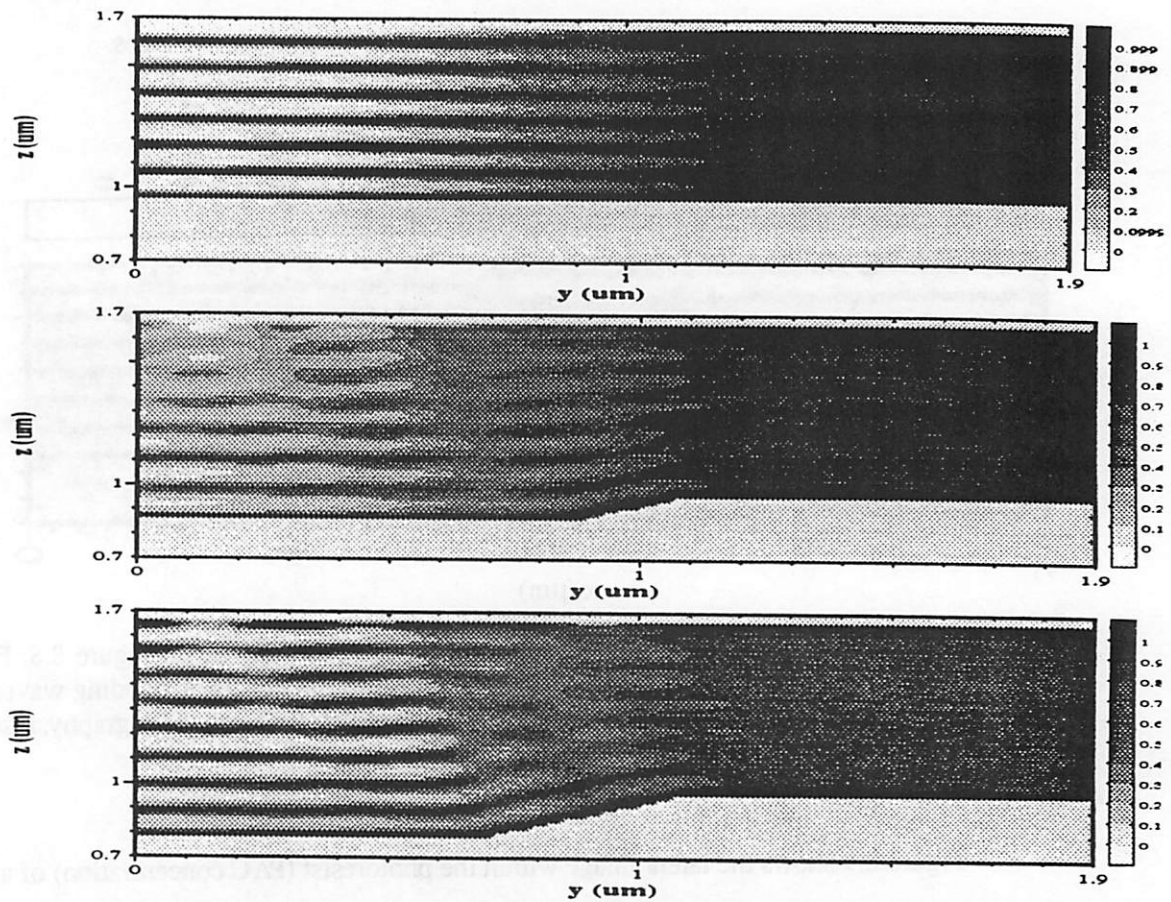


Figure 8.10 PAC concentration of vertical planes along bb' (top), cc' (middle) and dd' (bottom). The critical dimension at the bird's beak (middle picture) is different from the other two.

8.6 Conclusions

The three-dimensional version of TEMPEST has been shown to be very useful in characterizing potential mask and reflective notching problems in photolithography. Studies of quartz bump defects of 360° phase do not show significant eccentricity or severe intensity reduction and will not print if the dose to clear is below 55% of the clear field exposure value. They also do not appear to have a resonance as is the case for a glass ridge. Examination of 1X projection printing of contact holes at 248 nm shows that transmission loss is typically three times more than the loss in isolated opening spaces. Polarization effects in binary mask transmission produce eccentricities in the images of square contact holes. The effect can be as large as 17% which is three

times that of a square contact hole at 5X projection printing. These eccentricities can be more important than the slight imbalance in the lengths of the sides of a normally square opening. It is hoped that these predictions will be confirmed by studies on 1X projection printing systems and/or aerial image monitoring systems. For example, transmission loss in small contact holes can be tested by using a series of contact holes of different sizes and monitoring the time of exposure required to clear the photoresist as a function of opening size.

TEMPEST has also been applied in an initial study of reflective notching in the printing of the polysilicon gate. The slope of the bird's beak re-directs the exposure energy and cause variations in the critical dimension. This effect has also been observed experimentally.

Chapter 9

Conclusions

Rigorous electromagnetic simulation in photolithography is expected to play a major role in the IC fabrication industry because of its ability to predict subtle effects of electromagnetic interaction with matter. For example, with the phase-shifting mask technique, rigorous electromagnetic simulations can predict the changes in aerial images due to subtle changes in the glass edge shape. Moreover, the ability in simulation studies to isolate certain effects also makes simulation attractive in the examination of complex ideas and novel methods. Furthermore, with the increasing cost of performing experiments and the decreasing cost of computer memory and time, simulation is expected to be an indispensable tool in developing new fabrication techniques.

The contributions of this thesis can be viewed as pushing the frontier of rigorous electromagnetic simulation in three areas: numerical methods, integration of scattering and imaging simulation software, and applications of simulation in the studies of state-of-the-art IC fabrication technologies. With regard to numerical methods, a three-dimensional formulation of rigorous electromagnetic modeling using the time-domain finite-difference approach on the connection machine CM-5 is presented. The use of a cubic grid in which the six electromagnetic field components are staggered in space makes the problem maps well onto parallel computer architectures. Stability of the conventional TDFD numerical scheme requires that the time step be smaller than a fraction of the spatial step multiplied by the speed of light as well as the real part of the refractive index be greater than the imaginary part. The latter requirement can be relaxed with the use of the frequency-dependent finite-difference time-domain method in which the convolution relation between the electric displacement and the electric field is modeled via a recursive relation. The Debye model (which models ionic-like materials) or the Lorentz model (which models metallic-like materials) are used with this (FD)²TD scheme. Termination of the simulation domain is achieved by the application of a novel second order absorbing boundary condition which is derived based on the harmonic nature of electromagnetic waves. This boundary condition is shown to be as accurate and more efficient than other existing boundary conditions.

Several extensions can be made to the current algorithm. More efficient boundary conditions can be formulated so that the simulation domain can be terminated as close to the scatterer as possible. This would reduce the memory requirement, allowing larger problems to be solved. These boundary conditions must be derived based on a different concept (such as the MEI method⁵⁷) than the conventional radiation boundary condition because close to the scatterer surfaces, the electromagnetic fields cannot be decomposed into propagating plane waves alone. Savings in memory is also possible with the use of a variable grid instead of the cubic grid implemented currently. This would maintain a constant node density throughout the simulation domain. Other possible extensions include the capability to analyze anisotropic materials and even non-linear effects. These would enable the modeling of quantum electronics such as laser cavities.

With regard to software integration, the software package TEMPEST contains supporting routines and a link to the aerial image simulation program SPLAT in addition to the electromagnetic solver. The linkage to SPLAT for image synthesis allows the results of rigorous electromagnetic simulation from TEMPEST to be interpreted in the context of optical system effects such as arbitrary lens aberrations. The execution time of each TEMPEST simulation is about 10 minutes on the connection machine CM-5. The number of CM-5 nodes required depends on the problem size. For a typical simulation domain of 4 μm by 4 μm by 1 μm , 64 nodes (out of a total of 512 nodes at the National Center for Supercomputing Applications) are needed. Convergence of the program is dominated by physical scattering phenomena.

Some improvements in the software package can be made. First, the program can be implemented a multiple-instruction multiple-data computer architecture such that the boundary condition can be calculated more efficiently. Second, TEMPEST can be rewritten for execution on more accessible computer architectures such as the Cray. In terms of simulation tool integration, TEMPEST can be integrated under the technology CAD framework of SIMPL²⁴. This would allow the simultaneous study of deposition and etching effects, optical system characteristics, and electromagnetic scattering, enlarging the scope of applicability of these simulation tools.

With regard to applications, TEMPEST is shown to be useful in two-dimensional and three-dimensional studies. Predictions of TEMPEST in different phase-shifting mask techniques had been validated by experimental data taken on different systems. Predictions from the program

can also be used to provide physical insight and design data for different fabrication technologies. Other two-dimensional applications such as metrology, alignment mark signal integrity and mask transmission have also been examined in other publications^{82,99,100}. Initial three-dimensional studies are also undertaken in this thesis in the areas of mask effects in projection printing of 1X contact holes and reflective notching. Through these different studies, TEMPEST has proven itself to be a valuable prediction tool in photolithography.

With regard to future work in the area of TEMPEST applications, experimental verifications of 1X contact hole predictions and 360° phase bump defect printability are important in order to validate the program. An integrated SIMPL-SPLAT-TEMPEST software package would allow more realistic structures to be simulated such as the actual alignment mark and trench memory structures. Other interesting applications include the effects of reflection from underlying topography during photoresist exposure which can cause variations in the polysilicon gate critical dimension, and characterization of projection printing of contact holes on attenuated phase-shifting masks. Alignment mark detection is another challenging issue as the planarization process makes the marks almost invisible.

With the current capabilities, TEMPEST is effective in modeling two-dimensional and three-dimensional electromagnetic scattering problems in photolithography. It is hoped that TEMPEST would continue to be useful in developing future integrated circuit processes.

References

- 1 E. Barouch, B. Bradie, G. Karniadakis, and S. Orszag, "Comprehensive 3D simulator with non-planar substrates," *Proc. SPIE, Optical/Laser Microlithography III*, vol. 1264, pp. 334-342, 1990.
- 2 Jörg Bischoff, Ulrich Glaubitz, and Norbert Haase, "New method of topography simulation in photolithography," *Proc. SPIE, Optical/Laser Microlithography*, vol. 1674, pp. 423-434, 1992.
- 3 Jeffrey G. Blaschak, and Gregory A. Kriegsmann, "A Comparative Study of Absorbing Boundary Conditions," *J. Comp. Phys.*, vol. 77, pp. 109-139, 1988.
- 4 Norman Bobroff, and Alan Rosenbluth, "Alignment errors from resist coating topography," *J. Vac. Sci. Technol., B*, vol. 6, no. 1, pp. 403-408, Jan./Feb. 1988.
- 5 Max Born, and Emil Wolf, *Principles of Optics*, pp. 526-532, Pergamon Press, 1989.
- 6 L. C. Botten, "A new formalism for transmission gratings," *Optica Acta*, vol. 25, no. 6, pp. 481-499, 1978.
- 7 R. Budd, J. Staples, and D. Dove, "A New Tool for Phase-Shift Mask Evaluation, the Stepper Equivalent Aerial Image Measurement System -- AIMS," *Proc. SPIE*, vol. 2087, pp. 162-171, 1993.
- 8 C. B. Burckhardt, "Diffraction of a Plane Wave at a Sinusoidally Stratified Dielectric Grating," *J. Opt. Soc. Am.*, vol. 56, no. 11, pp. 1502-1509, Nov. 1966.
- 9 José M. Carcione, Dan Kosloff, Alfred Behle, and Geza Seriani, "A spectral scheme for wave propagation simulation in 3-D elastic-anisotropic media," *Geophysics*, vol. 57, no. 12, pp. 1593-1607, Dec. 1992.
- 10 I. Chang, "Plane Electromagnetic Wave Scattering from Coated Cylinders," *M. S. Thesis*, MIT, 1989.
- 11 S. Chu, and S. Wong, "Linear Pulse Propagation in an absorbing medium," *Physical Review Letters*, vol. 48, no. 11, pp. 738-1293, 1982.
- 12 K. S. Cole, and R. H. Cole, "Dispersion and Absorption in Dielectrics," *J. Chem. Phys.*, vol. 9, p. 341, Apr. 1941.
- 13 L. N. Deriugin, "Equations for Coefficients of Wave Reflections from a Periodically Uneven Surface," *Dokl. Akad. Nauk., SSSR*, vol. 87, no. 6, pp. 913-916, 1952.
- 14 T. Doi, K. Tadros, B. Kuyel, and A. R. Neureuther, "Edge-profile, Materials and Protective Coating Effects on Image Quality," *Proc. SPIE, Integrated Circuit Metrology, Inspection and Process Control V*, vol. 1464, pp. 336-345, 1991.
- 15 Frederick H. Dill, Andrew R. Neureuther, James A. Tuttle, and Edward J. Walker, "Modeling Projection Printing of Positive Photoresist," *IEEE Trans. Electron Devices*, vol. ED-22, no. 7, pp. 456-464, Jul. 1975.

- 16 S. Dunbrack, A. Muray, C. Sauer, and R. Lozes, "Phase-shift mask technology: requirements for e-beam mask lithography," *Proc. SPIE, Integrated Circuit Metrology, Inspection, and Process Control V*, vol. 1464, pp. 314-326, 1991.
- 17 Bjorn Engquist, and Andrew Majda, "Absorbing Boundary Conditions for the Numerical Simulation of Waves," *Math. of Comp.*, vol. 31, no. 139, pp. 629-651, Jul. 1977.
- 18 Bjorn Engquist, and Andrew Majda, "Radiation Boundary Conditions for Acoustic and Elastic Wave Calculations," *Comm. on Pure and Applied Math.*, vol. 32, pp. 313-357, 1979.
- 19 R. Ferguson, R. Martino, R. Budd, G. Hughes, J. Skinner, J. Staples, C. Ausschnitt, and J. Weed, "Etched-Quartz Fabrication Issues for a 0.25 μm Phase-Shifted DRAM Application," *International Symposium on Electron, Ion, and Photon Beams*, Jun. 1993.
- 20 Richard Ferguson, William Adair, David O'Grady, Ronald Martino, Antoinette Molless, Brian Grenon, Alfred Wong, Lars Liebmann, Alessandro Callegari, Douglas Tulipe, Donna Sprout, Christopher Seguin, "Impact of Attenuated Mask Topography on Lithographic Performance," *Proc. SPIE, Optical/Laser Microlithography VII*, vol. 2197, pp. 130-139, 1994.
- 21 Bengt Fornberg, "High-Order Finite Differences and the Pseudospectral Method on Staggered Grids," *SIAM J. Numer. Anal.*, vol. 27, no. 4, pp. 904-918, Aug. 1990.
- 22 G. M. Gallatin, J. C. Wedster, E.C. Kintner, and F. Wu, "Modeling the images of alignment marks under photoresist," *Proc. SPIE, Optical Microlithography VI*, vol. 772, pp. 193-201, 1987.
- 23 John Gamelin, "Simulation of Topography Scattering for Optical Lithography with the Connection Machine," *M. S. Thesis*, Memorandum No. UCB/ERL M89/71, University of California, Berkeley, May 1989.
- 24 M. A. Grimm, K. Lee, and A. R. Neureuther, "SIMPL-1 (SIMulated Profiles from the Layout - Version 1)," *IEDM Technical Digest*, pp. 255-258, 1983.
- 25 Roberto Guerrieri, Karim H. Tadros, John Gamelin, and Andrew Neureuther, "Massively Parallel Algorithms for Scattering in Optical Lithography," *IEEE Trans. CAD*, vol. 10, no. 9, pp. 1091-1100, Sep. 1991.
- 26 R. Harrington, *Time-harmonic Electromagnetic Fields*, p. 19, McGraw-Hill, 1961.
- 27 W. Henke, D. Mewes, M. Weiss, G. Czech, and R. Schiessl-Hoyler, "Simulation of Defects in 3-Dimensional Resist Profiles in Optical Lithography," *Microelectronic Engineering*, vol. 13, pp. 497-501, 1991.
- 28 Robert L. Higdon, "Numerical Absorbing Boundary Conditions for the Wave Equation," *Mathematics of Computation*, vol. 49, no. 179, pp. 65-90, Jul. 1987.
- 29 W. Daniel Hillis, *The Connection Machine*, ACM Distinguished Dissertation, MIT Press, 1985.
- 30 Intel Corporation, *Paragon Supercomputers*, Intel Corporation, 1992.
- 31 J. D. Jackson, *Classical Electrodynamics*, pp. 281-282, John Wiley & Sons, 1975.

- 32 J. D. Jackson, *Classical Electrodynamics*, p. 288, John Wiley & Sons, 1975.
- 33 F. G. Kasper, "Diffraction by thick, periodically stratified gratings with complex dielectric constant," *J. Opt. Soc. Am.*, vol. 63, no. 1, pp. 37-45, Jan. 1973.
- 34 William Kaufmann, and Larry Smart, *Supercomputing and the Transformation of Science*, Scientific American Library, 1993.
- 35 Kendall Square Research, *KSRI Technical Summary*, Kendall Square Research, 1992.
- 36 David Kershaw, "The Incomplete Cholesky - Conjugate Gradient Method for the Iterative Solution of Systems of Linear Equations," *J. Comp. Phys.*, vol. 26, pp. 43-65, 1978.
- 37 C. P. Kirk, "Theoretical Models for the Optical Alignment of Wafer Steppers," *Proc. SPIE, Optical Microlithography VI*, vol. 772, pp. 134-141, 1987.
- 38 Zoran Krivokapic, *Advanced Micro Devices, personal discussions*, Feb. 1994.
- 39 K. S. Kunz and K. M. Lee, "A Three-Dimensional Finite-Difference Solution of the External Response of an Aircraft to a Complex Transient Electromagnetic Environment: Part I - The Method and its Implementation," *IEEE Trans. Electromagnetic Comp.*, vol. EMC-20, pp. 328-333, May 1978.
- 40 M. E. Law, and R. W. Dutton, "Verification of Analytic Point Defect models Using SUPREM-IV," *IEEE Trans. CAD*, vol. 7, pp. 181-190, Feb. 1988.
- 41 C. F. Lee, R. T. Shin, and J. A. Kong, "Finite Difference Method for Electromagnetic Scattering Problems," *PIER 4: Progress in Electromagnetics Research*, pp. 415-435, Elsevier Science Publishing Co., Inc., 1991.
- 42 M. D. Levenson, N. S. Viswanathan, and R. A. Simpson, "Improving Resolution in Photolithography with a Phase-Shifting Mask," *IEEE Trans. Electron Devices*, vol. ED-29, no. 12, pp. 1812-1846, Dec. 1982.
- 43 B. Lin, "The Attenuated Phase-Shifting Mask," *Solid State Tech.*, vol. 35, no. 1, pp. 43-47, Jan. 1992.
- 44 Lo & Lee, *Antenna Handbook*, pp. 5-14, Van Nostrand Reinhold Company, 1988.
- 45 B. A. Lippmann, "Note on the Theory of Gratings," *J. Opt. Soc. Am.*, vol. 43, no. 5 pp. 408, 1953.
- 46 Kevin Lucas, Chi-Min Yuan, and Andrzej Strojwas, "A Rigorous and Practical Vector Model for Phase Shifting Masks in Optical Lithography," *Proc. SPIE, Optical/Laser Microlithography V*, vol. 1674, pp. 252-263, 1992.
- 47 K. Lucas, A. Strojwas, K. K. Low, and C. Yuan, "Intensity Optimization for Phase Shifting Masks," *Proc. SPIE Optical/Laser Microlithography VI*, vol. 1927, pp. 438-449, 1993.
- 48 R. Luebbers, F. Hunsberger, K. S. Kunz, R. B. Standler, and M. Schneider, "A Frequency-Dependent Finite-Difference Time-Domain Formulation for Dispersive Materials," *IEEE Trans. Electromagnetic Comp.*, vol. 32, no. 3, pp. 222-227, Aug. 1990.

- 49 R. J. Luebbers, F. Hunsberger, and K. S. Kunz, "A Frequency-Dependent Finite-Difference Time-Domain Formulation for Transient Propagation in Plasma," *IEEE Trans. Antennas Propagation*, vol. 39, no. 1, pp. 29-34, Jan. 1991.
- 50 Toshiharu Matsuzawa, Akemi Moniwa, Norio Hasegawa, and Hideo Sunami, "Two-Dimensional Simulation of Photolithography on Reflective Stepped Substrate," *IEEE Trans. CAD*, vol. CAD-6, no. 3, pp. 446-451, May 1987.
- 51 D. Maystre, "A new general integral theory for dielectric coated gratings," *J. Opt. Soc. Am.*, vol. 68, no. 4, pp. 490-495, Apr. 1978.
- 52 W. C. Meecham, "Variational Method for the Calculation of the Distribution of Energy Reflected from a Periodic Surface I," *J. Appl. Phys.*, vol. 27, no. 4, pp. 361-367, Apr. 1956.
- 53 Kenneth K. Mei, "Unimoment Method of Solving Antenna and Scattering Problems," *IEEE Trans. Antennas Propagation*, vol. AP-22, no. 6, pp. 760-766, Nov. 1974.
- 54 Kenneth K. Mei, Andreas Cangellaris, and Diogenes J. Angelakos, "Conformal time domain finite difference method," *Radio Science*, vol. 19, no. 5, pp. 1145-1147, Sep./Oct. 1984.
- 55 Kenneth Mei, *personal discussions*, Oct. 1991.
- 56 Kenneth K. Mei, and Jiajuan Fang, "Superabsorption - A Method to improve Absorbing Boundary Conditions," *IEEE Trans. Antennas Propagation*, vol. 40, no. 9, pp. 1001-1010, Sep. 1992.
- 57 Kenneth K. Mei, Rafael Pous, Zhaoqing Chen, Yao-Wu Liu, and Mark D. Prouty, "Measured Equation of Invariance: A New Concept in Field Computations," *IEEE Trans. Antennas Propagation*, vol. 42, no. 3, pp. 320-328, Mar. 1994.
- 58 D. E. Merewether, "Transient Currents Induced on a Metallic Body of Revolution by an Electromagnetic Pulse," *IEEE Trans. Electromagnetic Comp.*, vol. EMC-13, pp. 41-44, May 1971.
- 59 Mahmood K. Moaveni, Azhar A. Rizvi, and Bahman A. Kamran, "Plane-wave scattering by gratings of conducting cylinders embedded in an inhomogeneous and lossy dielectric," *J. Opt. Soc. Am., A*, vol. 5, no. 6, pp. 834-842, Jun. 1988.
- 60 M. A. Morgan, C. H. Chen, and S. C. Hill, "Finite Element-Boundary Integral Formulation for Electromagnetic Scattering," *Wave Motion*, vol. 6, pp. 91-103, 1984.
- 61 Gerrit Mur, "Absorbing Boundary Conditions for the Finite-Difference Approximation of the Time-Domain Electromagnetic-Field Equations," *IEEE Trans. on Electromagnetic Comp.*, vol. EMC-23, no. 4, pp. 377-382, Nov., 1981.
- 62 L. W. Nagel, "SPICE2 - A computer Program to Simulate Semiconductor Circuits," *M. S. Thesis*, Memorandum No. ERL-M520, University of California, Berkeley, May 1975.
- 63 A. R. Neureuther, K. Zaki, "Numerical Methods for the Analysis of Scattering from Non-planar Periodic Structures," *Intn'l URSI Symposium on Electromagnetic Waves*, Stresa, Italy, pp. 282-285, 1969.

- 64 A. R. Neureuther, "Modeling Phase Shifting Masks," *Proc. SPIE, BACUS Symposium*, vol. 1496, pp. 80-88, 1990.
- 65 M. Nevriere, P. Vincent, R. Petit, and M. Cadilhac, "Systematic Study of Resonances of Holographic Thin Film Couplers," *Optics Communications*, vol. 9, no. 1, pp. 48-53, Sep. 1973.
- 66 Khanh Nguyen, Tai Nguyen, Alfred Wong, Andrew Neureuther, and David Attwood, "Areal Images of EUV Projection Lithography Masks with Defects in Reflective Coatings: Electromagnetic Simulation," *OSA Proc. on Soft X-Ray Projection Lithography*, vol. 18, pp. 47-53, 1993.
- 67 A. Nitayama, T. Sato, and K. Hashimoto, "New Phase Shifting Mask with Self-aligned Phase Shifters for a Quarter Micron Photolithography," *IEDM Tech. Digest*, pp. 3.3.1-3.3.4, 1989.
- 68 D. Nyyssonen, "Theory of optical edge detection and imaging of thick layers," *J. Opt. Soc. Am.*, vol. 72, no. 10, pp. 1425-1436, Oct. 1982.
- 69 D. Nyyssonen, and C. P. Kirk, "Optical microscope imaging of lines patterned in thick layers with variable edge geometry: theory," *J. Opt. Soc. Am., A*, vol. 5, no. 8, pp. 1270-1280, Aug. 1988.
- 70 W. G. Oldham, S. N. Nandgaonkar, A. R. Neureuther, and M. M. O'Toole, "A General Simulator for VLSI Lithography and Etching Processes: Part I - Application to Projection Lithography," *IEEE Trans. Electron Devices*, vol. ED-26, no. 4, pp. 717-722, Apr. 1979.
- 71 Edward D. Palik (Editor), *Handbook of Optical Constants of Solids II*, pp. 374-385, Academic Press, 1991.
- 72 R. Petit, and M. Cadilhac "Sur la diffraction d'une onde plane par un réseau infiniment conducteur," *C. R. Acad. Sci., B*, vol. 262, no. 7, pp. 468-471, 1966.
- 73 C. Pierrat, A. Wong, and S. Vaidya, "Phase-Shifting Mask Topography Effects on Lithographic Image Quality," *IEDM Tech. Digest*, pp. 53-56, 1992.
- 74 Mark R. Pinto, Conor S. Rafferty, and Robert W. Dutton, "PISCES-II - Poisson and Continuity Equation Solver," *Stanford Electronics Laboratory Technical Report*, Stanford University, Sep. 1984.
- 75 Lord Rayleigh, "On the Dynamical Theory of Gratings," *Proc. R. Soc. London, A*, vol. 79, pp. 399-416, 1907.
- 76 Lord Rayleigh, *The Theory of Sound*, vol. 2, pp. 86-96, Dover, 1945.
- 77 R. A. Renaut, "Absorbing Boundary Conditions, Difference Operators, and Stability," *J. Comp. Phy.*, vol. 102, pp. 236-251, 1992.
- 78 Youcef Saad, and Martin Schultz, "GMRES: A Generalized Minimal Residual Algorithm for Solving Nonsymmetric Linear Systems," *SIAM J. Sci. Stat. Comput.*, vol. 7, no. 3, pp. 856-869, Jul. 1986.
- 79 S. Selberherr, A. Schütz, and H. W. Pötzl, "MINIMOS - a Two-Dimensional MOS Transistor Analyzer," *IEEE Trans. Electron Devices*, vol. ED-27, pp. 1540-1550, 1980.

- 80 John A. Stratton, *Electromagnetic Theory*, pp. 486-488, McGraw-Hill, 1941.
- 81 K. Tadros, A. R. Neureuther, J. Gamelin, and R. Guerrieri, "Investigation of Reflective Notching with Massively Parallel Simulation," *Proc. SPIE, Optical/Laser Microlithography III*, vol. 1264, pp. 322-332, Mar. 1990.
- 82 K. Tadros, A. R. Neureuther, and R. Guerrieri, "Understanding Metrology of Polysilicon Gates through Reflectance Measurements and Simulation," *Proc. SPIE, Integrated Circuit Metrology, Inspection and Process Control V*, vol. 1464, pp. 177-186, 1991.
- 83 A. Taflove and M. E. Brodwin, "Numerical Solution of Steady-state Electromagnetic Scattering Problems Using the Time Dependent Maxwell's Equations," *IEEE Trans. Microwave Theory Tech.*, vol. MTT-23, pp. 623-630, Aug. 1975.
- 84 Allen Taflove, and Korada Umashankar, "A Hybrid Moment Method/Finite-Difference Time-Domain Approach to Electromagnetic Coupling and Aperture Penetration into Complex Geometries," *IEEE Trans. Antennas Propagation*, vol. AP-30, no. 4, pp. 617-627, Jul. 1982.
- 85 C. D. Taylor, D. H. Lam, and T. H. Shumpert, "Electromagnetic Pulse Scattering in Time-varying Inhomogeneous Media," *IEEE Trans. Antennas Propagation*, vol. AP-17, pp. 585-589, Sep. 1969.
- 86 Technology Modeling Associates, *DEPICT-2*, Technology Modeling Associates, 1990.
- 87 T. Terasawa, N. Hasegawa, T. Kurosaki, and T. Tanaka, "0.3-micron optical lithography using a phase-shifting mask," *Proc. SPIE, Optical/Laser Microlithography II*, vol. 1088, pp. 25-33, 1989.
- 88 Thinking Machines Corporation, *CM5 Technical Summary*, Thinking Machines Corporation, Nov. 1992.
- 89 Kenny Toh, "Two-Dimensional Images with Effects of Lens Aberrations in Optical Lithography," *M. S. Thesis*, Memorandum No. UCB/ERL M88/30, University of California, Berkeley, May 1988.
- 90 K. Toh, G. Dao, R. Singh, and H. Gaw, "Chromeless Phase-Shifted Masks: A New Approach to Phase-Shifting Masks," *Proc. SPIE, BACUS Symposium*, vol. 1496, pp. 27-53, 1990.
- 91 Lloyd N. Trefethen, "Instability of Difference Models for Hyperbolic Initial Boundary Value Problems," *Comm. Pure and Appl. Math.*, vol. 37, pp. 329-367, 1984.
- 92 Lloyd N. Trefethen, and Laurence Halpern, "Well-Posedness of One-Way Wave Equations and Absorbing Boundary Conditions," *Math. of Comp.*, vol. 47, no. 176, pp. 421-435, Oct. 1986.
- 93 H. Paul Urbach, and Douglas A. Bernard, "Modelling Latent Image Formation in Photolithography using the Helmholtz Equation," *Proc. SPIE, Optical/Laser Microlithography III*, vol. 1264, pp. 278-293, 1990.
- 94 A. J. Warnecke, P. J. Lopresti, "Refractive Index Dispersion in Semiconductor-related Thin Films," *IBM J. Res. Develop.*, pp. 256-262, May 1973.

- 95 G. Wojcik, D. Vaughn, and L. Galbriath, "Calculation of Light Scatter from Structures on Silicon Surfaces," *Proc. SPIE, Optical/Laser Microlithography*, vol. 772, pp. 21-31, 1987.
- 96 Gregory L. Wojcik, David K. Vaughan, John Mould, Francisco Leon, Qi-De Qian, and Michael A. Lutz, "Laser Alignment Modeling Using Rigorous Numerical Simulations," *Proc. SPIE, Optical/Laser Microlithography IV*, vol. 1463, pp. 292-303, 1991.
- 97 Gregory L. Wojcik, John Mould, Robert J. Monteverde, Jaroslav J. Prochazka, and John R. Frank, "Numerical Simulation of Thick Line Width Measurements by Reflected Light," *Proc. SPIE, Integrated Circuit Metrology, Inspection, and Process Control V*, vol. 1464, pp. 187-203, 1991.
- 98 G. Wojcik, J. Mould, R. Ferguson, R. Martino, and K. K. Low, "Some image modeling issues for I-line, 5x phase shifting masks," *Proc. SPIE, Optical/Laser Microlithography VII*, vol. 2197, pp. 455-465, 1994.
- 99 A. Wong, T. Doi, D. Dunn, and A. R. Neureuther, "Experimental and Simulation Studies of Alignment Marks," *Proc. SPIE, Optical/Laser Microlithography IV*, vol. 1463, pp. 315-323, Mar. 1991.
- 100 Alfred Wong, and Andrew Neureuther, "Polarization Effects in Mask Transmission," *Proc. SPIE, Optical/Laser Microlithography V*, vol. 1674, pp. 315-323, 1992.
- 101 Alfred K. Wong, and Andrew R. Neureuther, "Edge Effects in Phase-shifting Masks for 0.25 μm Lithography," *Proc. SPIE*, vol. 1809, pp. 222-228, 1992.
- 102 Alfred K. Wong, "Two-dimensional Electromagnetic Simulation of Topography Scattering and Diffraction for Optical Lithography," *M. S. Thesis, Memorandum No. UCB/ERL M92/115*, University of California, Berkeley, Oct. 1992.
- 103 Alfred Wong, *TEMPEST Users' Guide*, Electronics Research Laboratory, University of California, Berkeley, Aug. 1994.
- 104 K. S. Yee, "Numerical Solution of Initial Boundary Value Problems Involving Maxwell's Equations in Isotropic Media," *IEEE Trans. Antennas Propagation*, vol. 14, pp. 302-307, May 1966.
- 105 Michael Yeung, *personal discussions*, University of California, Berkeley, Feb. 1992.
- 106 Michael Yeung, and Andrew Neureuther, "Improvement of the physical-optics approximation for topography simulation in optical lithography," *Proc. SPIE, Optical/Laser Microlithography VI*, vol. 1927, pp. 833-846, 1993.
- 107 Michael Yeung, *SCOE Review Presentation*, University of California, Berkeley, May 1994.
- 108 Chi-Min Yuan, and Andrzej J. Strojwas, "Modeling optical microscope images of integrated-circuit structures," *J. Opt. Soc. Am., A*, vol. 8, no. 5, pp. 778-790, May 1991.
- 109 Chi-Min Yuan, and Andrzej J. Strojwas, "Modeling Optical Equipment for Wafer Alignment and Line-Width Measurement," *IEEE Trans. Semiconductor Manufacturing*, vol. 4, no. 2, pp. 99-110, May 1991.
- 110 Chi-Min Yuan, "Calculation of One-Dimensional Lithographic Aerial Images Using the Vector Theory," *IEEE Trans. Electron Devices*, vol. 40, no. 9, pp. 1604-1613, Sep. 1993.

- 111 Kawthar Abd El Hamid Zaki, "Numerical Methods for the Analysis of Scattering from Non-planar Periodic Structures," *Dissertation*, University of California, Berkeley, pp. 47-56, Jul. 1969.
- 112 Svetlana S. Zivanovic, Kane S. Yee, and Kenneth K. Mei, "A Subgridding Method for the Time-Domain Finite-Difference Method to Solve Maxwell's Equations," *IEEE Trans. Microwave Theory Tech*, vol. 39, no. 3, pp. 471-479, Mar. 1991.